Analysis of Fluid-Dynamical and Multiphase Flow Aspects of Capillary Membrane Backwashing

Von der Fakultät für Ingenieurwissenschaften, Abteilung Maschinenbau und Verfahrenstechnik

der

Universität Duisburg-Essen

zur Erlangung des akademischen Grades

eines

Doktors der Ingenieurwissenschaften

Dr.-Ing.

genehmigte Dissertation

von

Hussam Mansour

aus

Syrien

Referent: Uni.-Prof. Dr.-Ing. Wojciech Kowalczyk
Korreferent: Uni.-Prof. Dr.-Ing. Stefan Panglisch
Tag der mündlichen Prüfung: 21.12.2017

Acknowledgements

First and foremost I would like to thank my supervisor, Prof. Dr.-Ing. Wojciech Kowalczyk, for his patient guidance and support throughout my thesis. He gave me the freedom to pursue my own ideas. I appreciate all the time, ideas and constructive feedback he contributed to make my Ph.D. experience productive and stimulating.

I am also indebted to Prof. Dr.-Ing. Stefan Panglisch for his critical suggestions and for sharing his experience to develop this work.

I would like to thank the chair of Mechanics and Robotics at the University of Duisburg-Essen for allowing me to use the chair equipment and providing the necessary software and hardware, and especially, working atmosphere. I would also like to express my thanks to the academic staff for their supportive discussions.

Financial support from the Deutsche Forschungsgemeinschaft (DFG) is gratefully acknowledged. Additionally, I would like to thank the IT Center at RWTH Aachen University for granting me access to their High Performance Computing (HPC) systems to perform simulations, and for providing technical support.

I would like to express my deep gratitude to my large family for their strong, consistent encouragement and unconditional support.

Finally, special thanks to you Wejdan for being by my side during this time, for your quiet patience and your love.

Abstract

The number of industrial applications has increased exponentially in the last decades and the need for effective water treatment methods has become more essential as demand for pure water has increased. It is no longer possible to fulfil the rapidly growing demand worldwide using natural water resources. Low pressure membrane filtration with inside-out dead-end driven UF-/ MF- capillary membranes has been widely inserted in water and wastewater treatment plants to remove colloids and suspended particulate matter. However, the implementation of this technology has been limited by several factors. These include concentration polarisation, membrane fouling and particles which remain inside the capillary after backwashing.

An efficient backwash process is a determining factor in ensuring effective membrane filtration and enhance the separation of the particles in the capillary membrane. By optimising the backwash process, hydraulical irreversible membrane fouling can be minimised and membrane permeability recovered, and the operating costs of the filtration process can consequently be controlled.

In the context of this thesis, a numerical approach to the detailed description of the fluid dynamics process in capillary membrane during backwashing is developed and partially validated by experiments. Moreover, the study contributes to a better understanding of the conditions for potential formation of agglomerates inside the capillary, which lead to increased operating pressure during the process and may clog the capillary.

The presented model investigates a variety of parameters associated with the backwash process in dead-end capillary membrane, such as operation parameters, in particular the operating pressure as a function of time, particle properties (size and density) and initial particle distribution in addition to capillary arrangement (vertical/horizontal). The evaluation of these data concentrates on observation and analysis of particle behaviour and distribution in a cross-sectional plane and along the capillary length. Based on the fluid flow and particle distribution, the eventual formation of particle plugs inside the capillary membrane is predicted.

For this purpose, a multiphase flow model was developed to describe the fluid flow and particle motion inside the capillary membrane. The numerical model considers the interaction between the involved phases in terms of lift, virtual mass and drag forces. The simulations are carried out using different configurations of the initial particle distribution, homogeneous distribution, evenly and unevenly deposited particles. The model is coupled with a population balance equation to account for particle agglomeration and breakage.

Furthermore, the pressure drop as well as the shear stress on the membrane surface inside the capillary during the backwash process are estimated. Based on the fact that during the backwash there are tightly adhered layers which can not be removed, the influence of these layers on the process is taken into account.

The simulation results show a good agreement with the experimental data in terms of the flow rate during the backwash process and particle removal at certain operating pressures.

Contents

List of Figures

List of Tables

Nomenclature

α	subscript refers to the phase	
β	inertial resistance	$1/m$
$\boldsymbol{\gamma}$	strain rate tensor	$1/s$
$\boldsymbol{\tau^{eff}}$	effective Reynolds stress tensor	m^2/s^2
$\boldsymbol{\tau}$	viscous stress tensor	Pa
$\boldsymbol{F}^D$	drag force	N
$\boldsymbol{F}^L$	lift force	N
$\boldsymbol{F}^V$	virtual mass force	N
$\boldsymbol{g}$	gravitational acceleration	m/s^2
$\boldsymbol{I}$	identity tensor	
$\boldsymbol{M}^D$	drag momentum rate	$kg/(m^2s^2)$
$\boldsymbol{M}^L$	lift momentum rate	$kg/(m^2s^2)$
$\boldsymbol{M}^V$	virtual mass momentum rate	$kg/(m^2s^2)$
$\boldsymbol{M}_\alpha$	interfacial momentum exchange rate acting on phase α	$kg/(m^2s^2)$
$\boldsymbol{S}$	source term	m/s^2
$\boldsymbol{u}$	velocity	m/s

$\boldsymbol{u}_\alpha$	velocity of the phase α	m/s
$\boldsymbol{u}_c$	velocity of the continuous phase	m/s
$\boldsymbol{u}_r$	relative velocity	m/s
$\boldsymbol{x}$	external, spatial coordinates	m
ΔP	transmembrane pressure	Pa
Δt	time step	s
Δx	distance between two neighboring cell centers	m
$\frac{D}{Dt}$	substantive derivative	
κ_α	source term of the weighted abscissa equation	
λ_m	thickness of the membrane	m
μ	dynamic viscosity	$Pa.s$
ν	kinematic viscosity	m^2/s
ν^{eff}	effective kinematic viscosity	m^2/s
ν^t	turbulent kinematic viscosity	m^2/s
ν_α	molecular kinematic viscosity	m^2/s
Φ_c	flow response time	s
Φ_d	particle response time	s
ψ	permeability	$L/(m^2\,h\,bar)$
ρ	density	kg/m^3
θ_α	source term of the weighted equation	
υ	internal coordinate, particle volume	m^3
ς_α	weighted abscissa	$-$

$\vartheta(v)$	mean number of particles formed by breakage	–
ξ	quadrature abscissas	m^3
$b(v)$	breakage frequency	$1/s$
B_b	particles birth rate due to the breakage	$1/(m^6 s)$
B_a	particles birth rate due to the aggregation	$1/(m^6 s)$
c	subscript refers to the continuous phase	
C_D	coefficient of interphase drag force	–
C_v	coefficient of interphase virtual mass force	–
$C_{L,\alpha}$	coefficient of interphase lift force	–
C_t	dimensionless coefficient	–
Co	Courant number	–
D	viscous resistance	$1/m^2$
D_a	particles death rate due to the aggregation	$1/(m^6 s)$
D_b	particles death rate due to the breakage	$1/(m^6 s)$
d_c	diameter of the capillary	m
d_α	particle diameter of phase α	m
$e(v, v')$	aggregation frequency	$1/(m^3 s)$
$f(\boldsymbol{x}, v, t)$	particle distribution function	$1/(m^6)$
J	permeate flux	m/s
k	turbulent kinetic energy	J/kg
L	characteristic length	m
L^*	normalised length of the capillary	–

n_m	number of pores	$-$
p	pressure	Pa
$P(v\|v')$	conditional probability of particle v' to generate a daughter particle v	$1/m^3$
Q	volumetric flow rate	m^3/s
r	radius of the capillary	m
r^*	normalised radius of the capillary	$-$
r_α	volume fraction of phase α	
R_c	cake layer resistance	$1/m$
R_m	resistance of clean membrane	$1/m$
r_m	radius of pores	m
R_p	pore blocking resistance	$1/m$
R_{total}	total filtration resistance	$1/m$
Re_α	particle Reynolds number	$-$
S_v	specific surface of the cake layer	$1/m^2$
S_k	source term in population balance equation	$1/(m^6 s)$
$S_k^{(n)}$	k moment of the source term given by population balance equation approximated by the n-point quadrature	$1/(m^6 s)$
St	Stokes number	$-$
t	time	s
V	volume	m^3
w	weight	$1/m^3$

Chapter 1

Introduction

1.1 Membrane technology in water treatment

Water is the most important resource for human life and activities. The demand for freshwater is rising worldwide due to increasing industrialisation and urbanisation as well as the decreasing quality and quantity of environmental water resources. Membrane processes have been widely used for water treatment due to their reliability, low energy consumption and efficient separation capabilities Fig. 1.1. In contrast to conventional plants, membrane-based plants work without the addition of chemicals and are cost-competitive as well as being relatively easy to install and operate. Membrane forms a physical barrier with selective permeability. It stops the target particles according to shape, size or properties and permits other compounds to pass through. The range of retained particles depends strongly on the pore structure which varies in size from macro to extremely small size on the micro and even nano scale.

1.2 Characterisation of the membrane processes

The membrane pore is one of the most important membrane characteristics. It denes the permeability and selectivity of a membrane according to its size, shape and distribution. Based on the membrane pore size, a membrane process can be classified into four main divisions, Microfiltration (MF), Ultrafiltration

Figure 1.1: Membrane filtration [1].

(UF), Nanofiltration (NF), and Reverse Osmosis (RO). Fig. 1.2 distinguishes the different types of membrane processes. MF and UF are porous membranes which can be operated at low pressure, whereas the RO is considered non-porous membrane. Both RO and NF require relatively high operating pressure and are therefore they are referred to as high pressure membranes. The target particles for MF and UF are much larger than for NF and RO due to the larger pore size. Table 1.1 summarises the main features of the four membrane processes according to their pore size and target substances [6].

MF has the largest pore size between $50 - 10000\ nm$ and can prevent bacteria and turbidity from passing through. NF has relatively very small pore (less

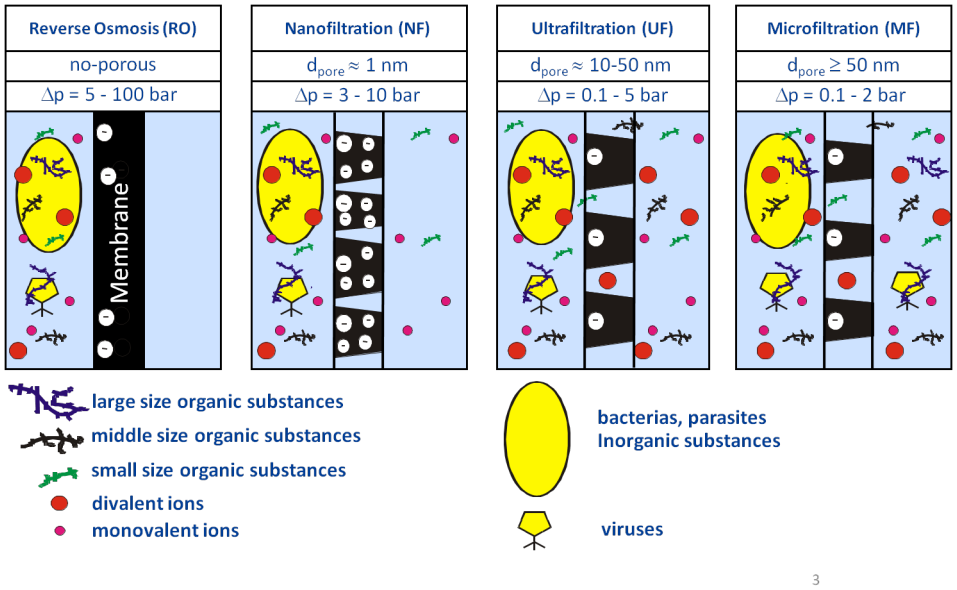

Figure 1.2: Membrane processes: Reverse Osmosis (RO), Nanofiltration (NF), Ultrafiltration (UF), Microfiltration (MF) [2].

than 2 nm) and stops dissolved ions in addition to organic molecules. UF membrane is intermediate between MF and NF. It has a pore size of $1 - 100$ nm. This range is able to remove smaller substances such as viruses, colloids and macromolecules. RO is very dense so there are no detectable pores and it becomes an efficient filtration method if the raw feed water is saline [6]. All these processes rely on the pressure difference between the fed water and the outer pressure to generate driving force for the particles [7]. The fed water is

Table 1.1: The main features of the four membrane processes.

Membrane process	**Pore size in nm**	**Target substances**
Microfiltration (MF)	50-10000	Bacteria, turbidity
Ultrafiltration (UF)	1-100	Virus, colloids, macrosolutes
Nanofiltration (NF)	2	Di-and multivalent ions, natural organic matter, small organic molecules
Reverse Osmosis (RO)	> 2	Dissolved ions, small molecules

exposed to a transmembrane pressure and due to the pressure gradient, the water passes through the membrane pore where the particles will be trapped on the membrane surface.

The Ultrafiltraion process has the greatest interest. It has been inserted in a wide variety of water treatment applications. Its advantages are a high removal rate of particles with relatively low operating costs and high flux rates at low operating pressure.

1.3 Modes of operation

Ultrafiltration membrane can be operated in two standard modes, cross flow and dead-end. In cross-flow mode, the feed water flows tangentially to the membrane surface. A portion of the feed water penetrates the membrane as permeate due to a pressure difference while the remaining feed water turns into retentate and can be recirculated again as feed stream. The shear rate developed on the membrane surface encourages the transport of the retained particles with the flow direction and thus may prevent the particles accumulating and maintains a low transmembrane pressure. This mode aids self-cleaning and allows longer operational time and longer intervals between backwash or membrane replacement. The efficiency of cross flow is determined by the flow velocity which is proportional to the energy needed.

In dead-end mode, all the feed water is forced to pass through the membrane due to driving pressure. The carried particles which are larger than the pore size accumulate on the membrane surface building up a cake layer. The formation of cake layers negatively effects the efficiency of the filtration process, declines the permeate flux and increases the operating pressure Fig. 1.3. In other words, dead-end mode is susceptible to high fouling. However, in terms of filtration dead-end can reduce energy costs since it works without continuous surface shear. By means of periodic backwash, the membrane can recover its permeability and eliminate the deposited particles [8, 9].

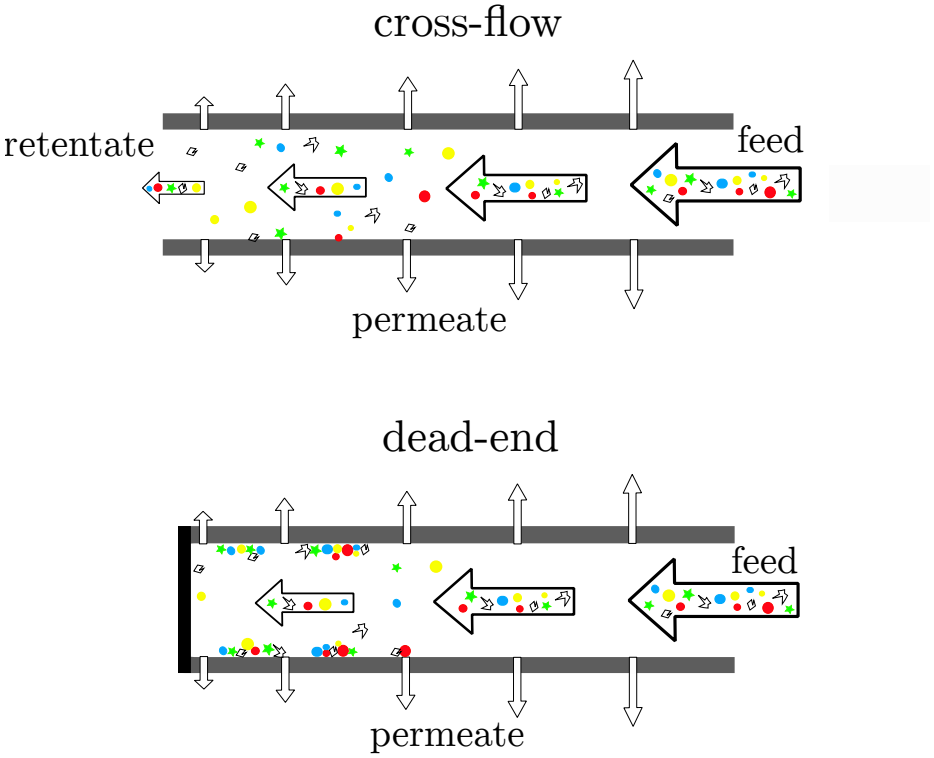

Figure 1.3: Schematic two different configurations of membranes in capillary module.

1.4 Module types of membrane filtration

In order to perform effective and economic filtration, a large area of membrane is required. Therefore, membrane is manufactured in different modules e.g. flat sheet, tubular, capillary and hollow fibre. Flat sheet module is one of the earliest configurations used for large scale processes. Due to the limitations related to the operation costs and packing density, flat sheet is not used in this form and is replaced by Spiral Wound module. Spiral Wound module is constructed for the Reverse Osmosis (RO) and Nanofiltration (NF) in addition to Microfiltration (MF) and Ultrafiltration (UF) systems and consists of layers of flat sheet membranes separated by porous spacers and wrapped around a collection tube, as shown in Fig. 1.4. The spacers prevent the compression of the membrane and define the height between the sheets. In addition, they create channels through the sheets and reduce the effect of concentration

polarization. This construction of the spiral wound module has a high membrane packing area and intermediate energy consumption. However, it is sensible to fouling and may require pretreatment.

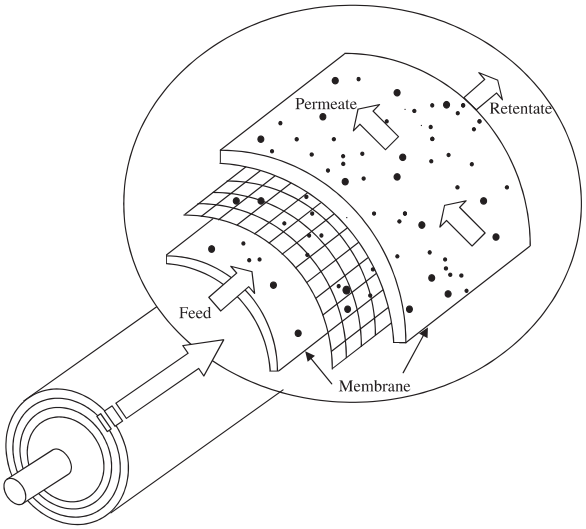

Figure 1.4: Spiral wound membrane module [3].

Tubular membrane module has the membrane area cast inside the support tube made of breglass, ceramic, plastic or stainless steel. Then, the single tubes are placed together in a plastic cylindrical form like a bundle. This module is suitable for cross flow mode and ensures a stable filtration rate, as shown in Fig. 1.5. The tubular membrane has a diameter in the range of 5 - 25 mm [10]. It has a high resistance to membrane fouling and enables easier chemical and mechanical cleaning. However, the low packing density of this module causes high operating costs.

The capillary module is equipped with large number of long, narrow capillaries. These capillaries are provided with a porous wall and are arranged in parallel next to each other in very close proximity. The capillary has a diameter between 0.5 - 5 mm [10]. It can be operated either in dead-end or cross flow mode under low pressure. The bundle contains between 50 and 10000 capillaries which are potted at each end to epoxy to form a cylindrical sheet. In Fig. 1.6,

Figure 1.5: Tubular ultrafiltration membrane module [4].

the housing and configuration of capillary membrane module operated in dead-end mode is explained. Capillary module has a very high packing density which allow large volumes of water to be filtered with a minimum effective surface area and low energy costs. One of the major disadvantages of this kind of membrane module is that it is highly susceptible to fouling, and consequently capillary plugging is likely to occur.

According to the direction of the flow in the porous capillary, the applications of this module can be divided into outside-in and inside-out. In the first configuration, the active surface is the outer shell side of the capillary. The feed water flows through the outer shell side of the capillary and the permeate is collected in the lumen side. Its advantage is that it handles large suspended solid particles. In contrast, in inside-out configuration, the active surface is the lumen surface of the capillary. Feed water with a low suspended solid particles is pumped through the capillary and the permeate is collected outside the capillary, Fig. 1.7 represents the arrangement inside-out in capillary bundle.

The hollow fibres module is very similar in design to the capillary module, but it uses a diameter in the range of 80 - 500 μm [10] and thus it has a larger packing density and higher likelihood of plugging.

Figure 1.6: Ultrafiltration capillary membrane module [1].

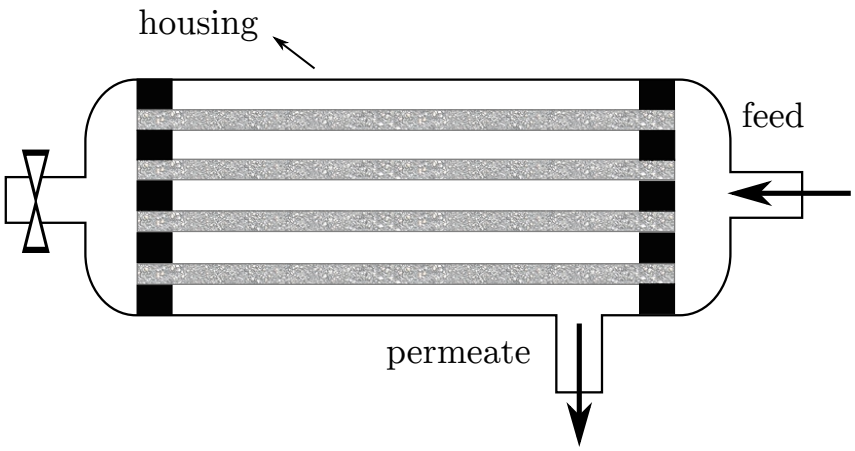

Figure 1.7: Schematic drawing of capillary membrane module.

The selection of the suitable membrane module for a certain membrane application is based on many factors, among others the costs, formation of

concentration polarisation, the tendency to fouling and the material used for the fabrication of the module [11, 4, 3].

1.5 Problem description and objectives

Although in the last decades membrane technology has undergone continuous development, the ultrafiltration process in capillary membrane is still of great interest since it has been inserted in a wide variety of water treatment applications. Over a long operating period, the dead-end fitration in capillary membrane module is prone to membrane fouling. This results in a loss of membrane permeability and an increase in membrane resistance due to the accumulation of particles on the membrane surface. The additional resistance manifests as flux decline and an increase in required operating costs. A periodic backwash of the capillary membrane removes the reversible fouling and recovers the membrane permeability and thus, the performance of the filtration process and productivity increase.

If the backwash is not efficient, the remaining particles in the capillary become harder and more difficult to remove due to the time effect. Consequently, the capillary will be clogged and the efficiency of the filtration process decreases. In other words, it is assumed that optimising the backwash process will aim at enhancing the removal of the cake layers, minimising fouling and regaining the initial membrane permeability. Furthermore, optimisation of the operating conditions is crucial for maintaining adequate long-term operation and effective and low operational costs for capillary membrane filtration. According to the research published in [12, 2, 13], the formation of capillary blockage caused by detached fouling layers may depend on the operating condition of the backwash. The particles are transported inside the capillary at different velocities, depending on their position and size. This behaviour might cause the formation of agglomerates or even the growth of existing agglomerates and can result in capillary plugging. This is why it is important to understand the mechanisms taking place inside the capillary during the backwash process.

The aim of the thesis is the development of a numerical model for the backwash process that describes the flow inside the capillary membrane, predicts the particle behaviour and observes the potential formation of agglomerates under different parameters set. Furthermore, the effect of operating conditions and particle properties on the efficiency of the backwash process and the particle behaviour are to be investigated with special consideration given to multiphase flow.

The thesis has been completed within the scope of a DFG-project. This project combines experimental work on the backwash process with modelling and numerical simulation of multiphase flow. Close cooperation between these two parts of the project was required in order to obtain fundamental understanding of the relevant backwash mechanisms. In relation to the simulation, the experimental part had the major specific objectives of providing the initial and boundary conditions needed for CFD simulation and verifying whether particles remain in the capillary after the backwash process is performed. Thus, the results obtained in the experimental part of the project were used in the theoretical study as process parameters; i.e. operating pressure, membrane permeability and the form of the deposited layer which is created on the surface membrane after the filtration process. The experiments were performed on a single capillary operated in dead-end mode [14]. In order to be able to compare the results of the experiment and the simulation, a similar capillary and particle properties (latex and quartz) in terms of size and density were used for the numerical simulations. In addition, the simulation time was compared with that of the experiment and accordingly defined, as extending the simulation time was much more expensive than is beneficial for the assumptions considered in the numerical study.

1.6 Description of the simulation procedure

Computational fluid dynamics (CFD) has been widely used in water treatment to evaluate and improve UF process. It has been proven to be a reliable tool for studying complex mechanisms taking place inside capillary membrane. Arising

from the need to better understand backwash in capillary membrane, CFD simulations are carried out to provide information about the particle behaviour inside a single capillary membrane. In order to achieve that, the following steps are covered in the thesis:

- For single phase flow
  - Build an adequate 3D CFD model for a single inside-out dead-end driven capillary membrane during backwash with consideration of the capillary's porous wall.
  - Define the initial and boundary conditions and discretize the computational domain in a finite number of control volumes.
  - Investigate the model under different operating conditions and with different membrane properties in a single phase flow.
  - Predict the pressure drop inside the capillary and the flow regime.
  - Define the boundary condition for further simulations.
  - Validate the obtained results in terms of flow rate.
- For two-phase flow
  - Build an adequate 3D CFD model for a single capillary membrane during backwash without consideration of porous walls.
  - Model the forces acting on the particles.
  - Discretize the computational domain in a finite number of control volumes.
  - Simulate the backwash process under different boundary conditions (operating pressure), different initial particle distribution (e.g. homogeneous, evenly deposited and unevenly deposited particles) and different particle properties (e.g. particle size, density).
  - Observe particle behaviour during the backwash in addition to the velocity profile and shear stress on the membrane surface.
  - Predict the pressure drop inside the capillary during the process.

  - Investigate various pressure functions and thereby the particle distribution and the particles remaining inside the capillary.
  - Predict the flow regimes in the presence of particles tightly adhered to the membrane surface.

- For Multi-phase flow
  - Build an adequate 3D CFD model for a capillary membrane during backwash without consideration of porous walls.
  - Analyse the behaviour of the polydisperse particles without consideration of agglomeration and breakup models.
  - Analyse the behaviour of the polydisperse particles with consideration of agglomeration and breakup models.
  - Observe potential formation of plugs inside the capillary.

The obtained results will be partly validated with the experiments. The performance of the backwash process will be discussed on the basis of the simulation results.

1.7 Global assumptions

In this chapter, the assumptions and approaches which are considered in this thesis are introduced. Due to the complexity of the backwash process and the complicated mechanisms taking place inside the capillary, simplifying assumptions for the mathematical modelling process are made. The assumptions include:

1. For single phase flow:
   - The thickness of the membrane as well as its permeability is constant along the capillary.
   - A steady state simulation is carried out.
   - The Reynolds number for the axial flow velocity inside the capillary indicates laminar working conditions.

- The modification of the membrane permeability takes into account the formation of the fouling layer as it has a porous structure.
- The bulges considered in the thesis are artificial configuration and may appear in segments of the capillary. They represent the non-backwashable and tightly adhered particles on the membrane surface. It is assumed that these bulges are impermeable and do not change their thickness during the backwash process. This assumption is not completely in agreement with reality, however it simplifies the model and reduces the computational effort. For these simulations the porous wall is not taken into account.

2. For multiphase flow:

   - The porous wall of the capillary is not included in the calculation, rather, the computational domain is limited to the inner diameter of the capillary. Furthermore, the definition of the boundary conditions for these simulations is derived by analysing the single phase flow in the capillary with a porous wall. It can be noticed that the variation of the radial component of the inward velocity is very small along the capillary length and can be neglected. That means the operating pressure is replaced by a constant flow rate at the inlet. These assumptions are essential in reducing the computational efforts and achieving the defined convergence more quickly.
   - For the purpose of simplifying the simulation model, the following forces are not considered in the theoretical study: inter-particles electrostatic force and adhesive forces on the wall.
   - The deposited particles detach from the membrane surface once the backwash process begins, i.e. the particles are not adhered to the membrane surface since this force is not considered.
   - The backwash process is simulated for the duration of 5 s due to the expensive computation time. This time is determined by some preliminary simulations and by the results provided by the primary experimental measurements of the project.

Chapter 2

State of the art

2.1 Fouling mechanism

UF by capillary membrane modules is increasingly used in the water treatment industry for the purpose of removing particulate matter from treated water. Its low energy demand, low operation pressure and high selectivity make UF particularly suitable technology for water filtration. However, one of the critical problems in the membrane process is membrane fouling. This problem has been under investigation for a long time since it is a challenging issue which restricts the development of membrane technology. By definition, fouling is the deposition of particles or solutes within or on the membrane so that the membrane's performance is degraded. The direct effect of fouling is the loss of the membrane throughput. It forms an additional layer which prevents water from entering through the membrane, as illustrated in Fig. 2.1. As this layer is created, either the flux rate declines when constant transmembrane pressure is maintained, or an increase of transmembrane pressure is necessary in order to compensate for the reduction in flux. In both cases, the energy consumption needed to treat the same volume of water rises significantly. Furthermore, fouling results in more frequent hydraulic and chemical cleaning of the membranes, in addition to high maintenance costs and a shortening of membrane lifetime due to chemical cleaning agents [15]. Fouling can take three forms in MF/UF in water treatment [16, 11], as shown in Fig. 2.1.

a) Pore restriction: Due to adsorption, the membrane pores are partially plugged by particles smaller than the pore size. This has a very significant influence on the membrane's permeability.

b) Pore blockage: Pore closure occurs during filtration when the particle diameter is larger than the pore size. As a consequence, the flux declines and high hydraulic resistance occurs.

c) Cake formation: The continuous deposition of individual particles on the membrane surface leads to the formation of a cake layer. This cake layer constitutes important additional hydraulic resistance. In dead-end mode, a cake layer grows without a limit and has a considerable effects on operating costs.

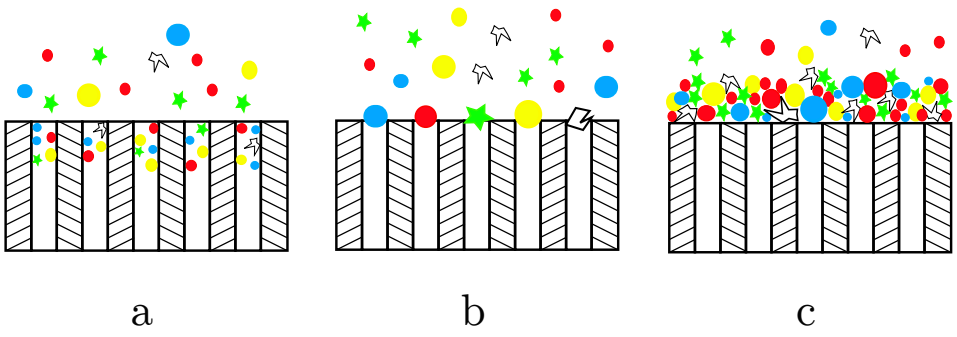

Figure 2.1: Schematic drawing of different fouling mechanisms: a) pore restriction b) pore blockage c) cake formation.

Fouling has been described and addressed in many studies which identify the main foulants and fouling mechanisms and introduce methods to control membrane fouling [17, 18]. Further information about the deposition of particles during UF in dead-end [19] and MF in cross flow [20], including deposit thickness measurements and its properties over the filtration time was obtained using an in-situ optical method. This enables observation of the growth of the cake layer and its effects on filtration performance. In review, the effect of feed properties, membrane properties and operating conditions on protein fouling in UF and MF were discussed [21]. The impact of several

operating parameters on the fouling process of UF membrane, including the transmembrane pressure and corresponding flux, was examined [22, 23, 24, 25].

Fouling in capillaries operated in dead-end mode in UF was also investigated by Heijman et al. [12]. Experiments under constant flux conditions with a lab-scale test installation on a UF capillary module in dead-end mode showed that fouling plugs blocked some capillaries during filtration. These blockages occur in both sides of the capillaries in the potting of the membrane module, as shown in Fig. 2.2. By measuring the transmembrane pressure, the blockages, especially in the potting zone at the rear side of the capillaries, could not be detected. The indicator for such blockages was an increase in forward flush pressure drop. The inefficient cleaning of the capillaries at potting zones by hydraulic cleaning (backwash) as well as chemical cleaning is a non-negligible factor which is responsible for these blockages. Moreover, Heijman et al. [5] found that heterogeneous particle distribution over the membrane surface appears if backwashing the capillaries is not able to remove all the fouling in the membrane. As a consequence, the flux in the clean area increases, but the formation of the cake layer is faster.

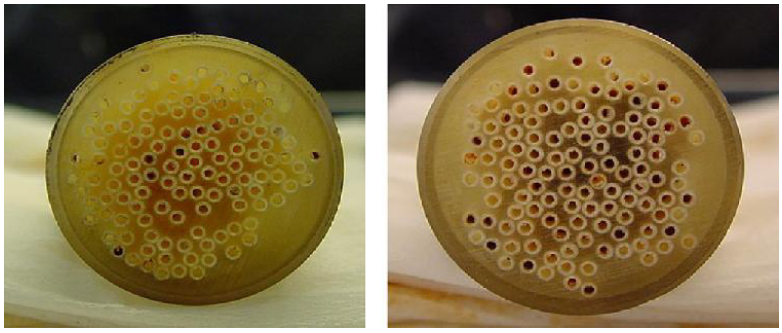

a b

Figure 2.2: Images show the blocking of the capillaries on the feed side a) and on the rear side b) after 18 h of operation [5].

2.2 Modelling of membrane processes

Many studies describe the decline in flux caused by fouling using mathematical models. These models consider the typical fouling mechanisms mentioned previously: pore restriction, pore blockage and cake formation. A simple model based on Darcy's law is widely used for cake layer formation. In this model, the permeate flux is given by the following expression as defined in [26, 27]:

$$J = \frac{\Delta P}{\mu(R_{total})} \tag{2.1}$$

J in this model is permeate flux m/s. It is proportional to the transmembrane pressure ΔP Pa and driving force and inversely proportional to the resistance in series model. The dynamic viscosity of the permeate flux is μ $kg/(s.m)$. The hydraulic resistance R_{total} $1/m$ is mainly composed of the hydraulic resistance of clean membrane R_m, the cake layer R_c and pore blocking resistance R_p. The total filtration resistance is calculated as:

$$R_{total} = R_m + R_c + R_p \tag{2.2}$$

For the membrane resistance, Hagen-Poiseuille equation can be used.

$$R_m = \frac{8\lambda_m \tau}{n_m (r_m)^2} \tag{2.3}$$

where λ_m is the thickness of the membrane, n_m is the number of pores per unit membrane area, r_m is the radius of membrane pores and τ is the tortuosity factor. From Eq. 2.3, it is clear that membrane resistance increases when pore size or pore density decreases.

Cake layer resistance is a function of filtration time. At the beginning of the filtration process, membrane resistance is dominant as the membrane pores are clean. Over time, the resistance of the cake layer increases when the thickness or denseness of the layer grows due to the accumulation of particles retained on the membrane surface. In this phase, the membrane resistance becomes a small portion of the total filtration resistance and may be negligible.

Cake layer resistance R_c is assumed to be proportional to the cake thickness and can be calculated as [28]:

$$R_c = R_c(t).\lambda_c \tag{2.4}$$

where $R_c(t)$ $1/m^2$ is specific cake resistance per unit cake thickness, and λ_c m is the thickness of cake layer. Then, the classic Carman-Kozeny equation defines the value of $R_c(t)$ as:

$$R_c(t) = \frac{K(1-\epsilon)^2}{\epsilon^3} S_v^2 \tag{2.5}$$

K is Carman-Kozeny constant, ϵ is the porosity and S_v is the specific surface of the cake layer. Eq. 2.5 indicates that the cake resistance increases when the porosity or the particle size decreases. In other words, the cake resistance increases when the cake structure becomes more compact. Pore blocking resistance R_p is caused by the complete or partial blocking of membrane pores. The degree of pore blockage depends on the ratio between particles and pore size. For particles smaller than the pore size the filtered particles fill the pores and then form the cake layer on the membrane surface. Whereas, for particles larger than the pore size the filtered particles accumulate on the surface without filling the pores and the cake layer grows across the entire filtration [29].

The particle transport mechanisms are a function of particle size, among other factors. By calculating the particle trajectories based on force balance, the formation of hardly removable particle layers in inside-out driven capillary membranes operated in dead-end mode and the particles deposition are theoretically predictable. According to their size, incoming particles are not deposited directly, rather they are transported into the capillary membrane, i.e. the larger the size, the longer the distance carried. If particles are larger than a so-called plug-forming diameter they are transported to the capillary dead-end which may cause a plugging of the capillary. Such plugs may contribute to irreversible fouling, as they may not be removed by backwashing and flushing

[13, 30]. Analysing the forces acting on the particles during the filtration process enables the calculation of particle displacement and velocity near the membrane surface [31] and highlights the effects of particle size, particle distribution and electrical surface potential on the structure of the cake layer [32, 33]. The formation and growth of the cake layer can be determined by the balance between drag force and lift force [34, 35]. Through their mathematical model Chang et al. [33] provide considerable insight into the predicted behaviour of filtration in fibre membrane experiencing particle deposition on its surface.

Developing a suitable process model of flux decline during filtration provides a better understanding of membrane fouling and enhances the design of effective operating strategies. First, mathematical models were evolved which focus on a simplified fouling mechanism [36]. Later, a combined fouling model which accounts for initial fouling due to pore blocking followed by growth of the cake layer was developed [37]. This model eliminates an intermediate mathematical formulation for the description of the transition regimes between pore blockage to cake layer, but without consideration of the internal fouling caused by protein adsorption. Next, the new fouling model was developed which accounts for the internal and external fouling caused by all three mechanisms [38]. A modified form of the combined pore blockage and cake filtration model developed by Ho and Zydney [37] can successfully describe humic acid fouling [39]. Additional work has been done to model organic fouling, taking into account the simultaneous action of all fouling mechanisms [40]. In another model, two coefficients were introduced to predict the flux decline in UF/MF cross flow [41]. These coefficients incorporate the influence of cake formation and shear cleaning and may characterise the performance of the membrane.

With the rapid development of super computers, CFD has become a powerful tool for increasing understanding of the complex fouling mechanisms, characterising the related physical phenomena governing performance and identifying the suitable operating conditions. Many models make use of computational fluid dynamics to predict flow profiles and the accumulation of particles on the membrane surface which lead to fouling layer formation in

pressure driven membrane [42, 43]. For instance, Bessiere et al. [44] developed a model applicable to dead-end filtration. This model describes the transport behaviour of concentrated colloidal dispersion and is implemented in commercial CFD code. It provides information about mass transport properties, both in dispersed (concentration polarisation) and condensed (deposit) forms of accumulation. Additionally, simulations were carried out to shed light on the influence of operating conditions and membrane characteristics on particle deposition. In other studies, CFD simulation is developed for three-dimensional cross flow models for different suspended particles, in order to predict their separation and accumulation as well as the exerted forces on these particles and provide information about the overall resistance of filtration and hydrodynamic shear forces on the membrane [45, 46, 47].

Moreover, a computational fluid dynamics model was developed for the description of the flow field in inside-out driven ultrafiltration capillaries [48]. This model is valid for both cross flow as well as dead-end modes and considers different physical properties of the flocs and membrane materials under a variety of operating conditions. It accounts for the growth of the fouling layer by numerically calculating the velocities and trajectories of the particles and by determining the possible positions of the deposit. These positions vary according to the particle size. Flocs of small size deposit homogeneously over the capillary length whereas larger flocs are carried a certain distance in the capillary and are then deposited inhomogeneously. This distance is proportional to the flocs' size. This transport mechanism contributes to the high potential for capillary clogging.

Computational fluid dynamics (CFD) has played a decisive role in the design of the module and development of membrane filtration technology. With significant improvements in computational resources, CFD has been attracting considerable interest for its ability to evaluate filtration and other related processes in water treatment [49, 50].

2.3 Membrane cleaning

The permanent operation of the filtration process leads to a significant increase in resistance and flux decline due to membrane fouling. In order to reestablish an effective filtration process and restore membrane performance, the particles must be removed from the membrane. This can be achieved by appropriate cleaning procedures. The cleaning treatment must efficiently contribute to extending the membrane's lifetime, reducing the energy demand and cutting down the cost of replacement without exceeding the chemical and mechanical limits of the membrane. Cleaning methods can be divided into two categories: the physical removal of particles and chemical cleaning by applying chemical agent [51]. Each of these categories deals with a different kind of fouling, either reversible or irreversible fouling, according to particle boundedness to each other and to the membrane surface. As mentioned above, reversible and irreversible fouling are the results of deposition and intrusion of macromolecules, particles and colloids on the membrane surface and into the membrane pore structure, respectively. Irreversible fouling can be removed by chemical cleaning, whereas reversible fouling can be completely removed by means of physical cleaning.

2.3.1 Physical cleaning

Physical cleaning uses mechanical forces to flush out the particles deposited on the membrane surface or into the membrane pores. This can be achieved by reversing the transmembrane pressure (e.g. backwashing) or enhancing the shear rates and turbulence by increasing the flow velocity (e.g. forward flush) or generating two phase flow (e.g. air flushing). For inside-out dead-end pressure driven capillaries, physical cleaning limits the effects of deposited particles and eliminates fouling resistance. The choice of cleaning method depends on both the type of fouling to be treated and the type of membrane module. There are several methods for membrane cleaning used in capillary membrane modules, some of which are listed below.

2.3.1.1 Backwash

The backwash process is categorised as hydraulic cleaning. It is operated by reversing the direction of the permeate flow in the capillary. In Fig. 2.3, the process is shown in a single capillary and Fig. 2.4c illustrates the process in a capillary membrane module. It is very effective at removing cake layer from the membrane surface. The back flow water lifts off the fouling layer and dislodges it out of the capillary. Thus, it helps avoid capillary clogging during the filtration as well as recovering the initial permeability. Ineffective backwash can also negatively influence the filtration process because flushing out the accumulated particles becomes much harder if a backwash process was not efficient enough to completely remove all potentially reversible fouling from the capillary. Thus, the remaining particles will contribute to irreversible fouling [52]. Furthermore, due to the heterogeneous fouling in dead-end capillaries and after an ineffective backwash, the remaining fouling is not evenly distributed on the membrane surface. As a consequence, different flux over the capillary length occurs and thus, different mechanisms for the formation of cake layer in the next filtration cycle can be observed [5]. The quantity of particles which remain on the membrane surface and may cause total permeability recovery is influenced by backwash parameters and procedure [53]. However, van de Ven et al. [54] proved that filtration processes can be operated in a stable manner when the backwash is applied to the last part of dead-end inside-out capillary in UF. The observation that fouling occurs primarily in the end part of the capillary led to the concept known as the partial backwashing concept.

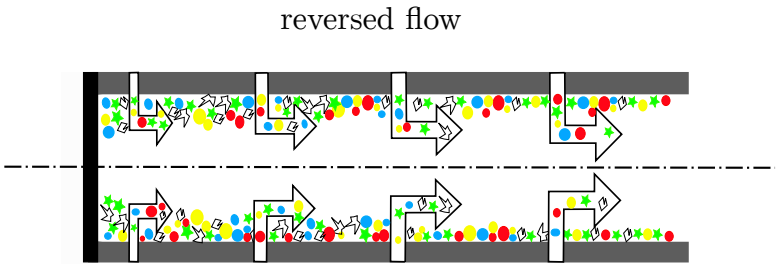

Figure 2.3: Backwash process illustrated in single capillary.

The backwash process and its impact on the reversible fouling [55, 40] and irreversible fouling mechanisms have been a main topic for researchers [22]. As mentioned above, backwashing with less than 100 % efficiency does not remove all reversible fouling, which then contributes to irreversible fouling. The backwashing performance was observed under different conditions in Out-to-In microfiltration, such as backwash pressure, interval, duration, volume and use of chemicals [56]. It was shown that the most significant results, in term of removal of the deposited particles, are obtained when the backwash water is delivered in a series of discrete pulses [56].

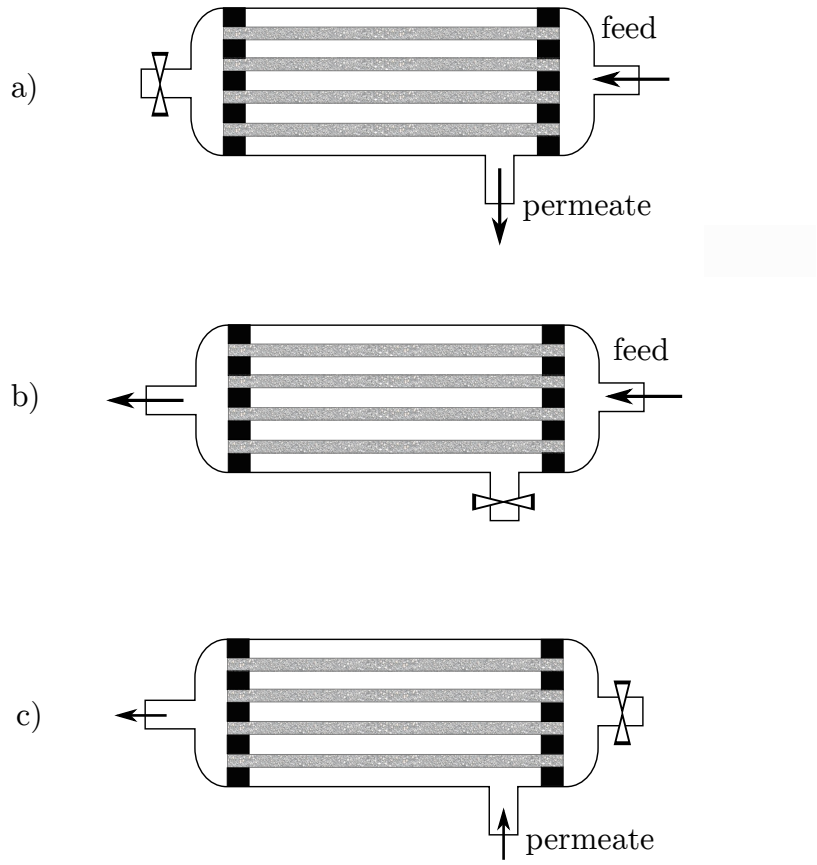

Figure 2.4: Schematic representation of the dead-end capillary membrane module a) filtration; b) forward flush; c) backwash in capillary membrane.

Optimisation of backwash frequency and duration are also reported in the literature [57]. For dead-end MF, the timing and duration of backwashing was

predicted by using an optimal control theory [58].

Backwashing usually uses UF permeate as cleaning water. However, backwash performance varies signicantly according to the composition of the backwashing solution. The addition of other components to the backwash water influences the membrane fouling considerably. Various types of backwash water in UF membrane were compared in order to achieve effective membrane cleaning [59, 60]. Furthermore, a comparison between demineralised water and UF permeate indicates that backwashing with demineralised water is much more efficient in terms of irreversible fouling removal [61]. However, the strong bindings between carboxylic functional groups of organic substances and membranes with bridging assistance from calcium ions does not enable backwashing with demineralised water to remove all biopolymers and humic substances [62]. Besides demineralised water, the investigation of solutions with different calcium or sodium concentrations for backwashing show that these components have a negative inuence on backwash performance [63].

2.3.1.2 Forward flush

In this method, the closed end of the membrane, which is responsible for the dead-end arrangement, is opened. The dead-end mode is temporary turned to cross flow and the permeate is closed. This method aims at removing the cake layer formed on the membrane surface during filtration. High shear rates in the vicinity of the membrane surface resulting from high flow velocity will enhance the removal of particles and restore the permeability. However, this method has a limited effect on the particles absorbed in or near membrane pores. The process is illustrated in Fig. 2.4b. This process is less effective than backwashing, however it demands relatively lower energy.

2.3.1.3 Air flushing

The removal of the deposited particles can be further improved by increasing the shear stress and producing a two phase flow in the vicinity of the membrane surface. Injecting air bubbles into the feed side of the capillary during

backwashing enhances the backwash process and reduces the backwash time. This method generates a considerable shear force which reduces the deposition of particles and transports them out of the module [53, 64, 65]. Comparing the performance of the cleaning methods in terms of fouling control and cleaning time, the combination of air bubbles and back-flushing was found to be much more effective than the process without air bubbles [66]. Even at low air velocity, a high backwash performance was obtained [67]. However, the drawback of this method is the inhomogeneity of the air-water distribution inside the module which may result in uneven removal of deposited particles.

2.3.2 Chemical cleaning

When the backwash process cannot restore membrane permeability, the use of chemical cleaning becomes important. Chemical cleaning applies chemical agents to influence the hydraulically irreversible foulants. This can be achieved either by adding chemicals to the backwash water and adjusting the cleaning time, or shutting down the filtration process and using special chemical agents at elevated temperatures. However, chemical cleaning leads to chemical costs and waste water discharge, as well as using energy, and it reduces membrane lifetime. Nevertheless, this technique has been subject to optimisation with the use of dynamic models to minimise operating costs for this part of the UF process [68, 69, 70].

Chapter 3

Theoretical consideration and modelling

3.1 Open-source CFD framework OpenFOAM

OpenFOAM (Field Operation And Manipulation) is a free framework for dealing with scalarial, vectorial and tensorial fields written in C++. It offers a wide range of numerical methods and discretisation schemes of time and space for the partial differential equations and the resulting linear algebraic equations. It contains libraries of pre-compiled solvers and classes for CFD problems. Furthermore, it includes a pre-processing tool for meshing the geometry and applying the boundary condition. The post-processing tool also supports the software for visualization of the results. The structure is explained in Fig. 3.1. OpenFOAM implements the finite volume method in each structured and unstructured control volume for the solution of governing equations for the fluid flow and then transforms the volume integral to surface integral according to the Gauss theorem. Different interpolation methods are available for the calculation of values at cell surface. OpenFOAM can be parallelised without license costs and offers access to its code to program new applications or adapt existing ones for the relevant problem. Moreover, it uses the object-oriented language C++ which enables users to modify or even compile their own solver or model independently of the basic codes. This flexibility makes it suitable for

complicated CFD problems and a significant subject for further development. Therefore, OpenFOAM was used for the cases considered in the current thesis to adjust the boundary conditions, solve the PDEs and visualise the results [71, 72].

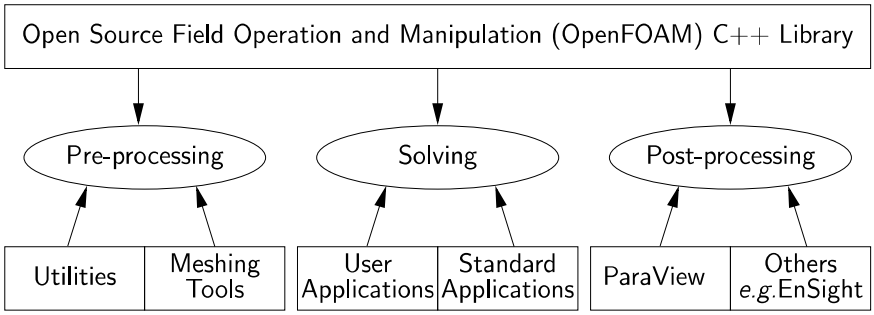

Figure 3.1: Overview of OpenFOAM structure.

3.2 Flow characterisation for single phase flow

3.2.1 Governing equations for single phase flow

The motion of a fluid can be described using continuity and momentum equations. These equations are derived from the conservation principles of mass and momentum. For Newtonian and incompressible fluid, viscosity and density are considered constant. Mass conservation Eq. 3.1: states that, the rate of mass increase in a control volume is equal to the net rate of flow of mass into the control volume.

$$\nabla \cdot \mathbf{u} = 0 \tag{3.1}$$

Momentum conservation Eq. 3.2: states that the rate of change of momentum is equal to the sum of considered forces.

$$\rho(\frac{\partial \mathbf{u}}{\partial t} + (\mathbf{u} \cdot \nabla)\mathbf{u}) = -\nabla p + \nabla \boldsymbol{\tau} \tag{3.2}$$

where u denotes the fluid velocity, ρ denotes the fluid density, t denotes time. The terms on the left side of the equation represents the substantial derivative

which consists of local derivative $\frac{\partial u}{\partial t}$ and convective derivative $(\mathbf{u} \cdot \nabla)\mathbf{u}$.
On the right side of Eq. 3.2 are the viscous force $\nabla\boldsymbol{\tau}$ and the pressure force ∇p. In single phase flow, there are no external forces and they are therefore set to zero. The shear stress tensor in Eq. 3.3 can be divided into symmetric and antisymmetric tensors which represent the rate of deformation of a fluid element and the velocity tensor, respectively.

$$\boldsymbol{\tau} = -\mu \left(\nabla\mathbf{u} + (\nabla\mathbf{u})^T - \frac{2}{3}(\nabla \cdot \mathbf{u})\mathbf{I} \right) \tag{3.3}$$

The second term of the equation is zero for incompressible flow. $\mathbf{I}$ denotes the Identity tensor, $(\nabla\mathbf{u})^T$ denotes the transpose of velocity gradient and μ denotes the dynamic viscosity. The strain rate tensor is given by Eq. 3.4

$$\boldsymbol{\gamma} = \frac{1}{2}\left(\nabla\mathbf{u} + (\nabla\mathbf{u})^T\right) \tag{3.4}$$

the components of the strain rate tensor are given in Eq. 3.5

$$\boldsymbol{\gamma} = \begin{bmatrix} \gamma_{xx} & \gamma_{xy} & \gamma_{xz} \\ \gamma_{yx} & \gamma_{yy} & \gamma_{yz} \\ \gamma_{zx} & \gamma_{zy} & \gamma_{zz} \end{bmatrix} = \begin{bmatrix} \frac{\partial u}{\partial x} & \frac{1}{2}\left(\frac{\partial u}{\partial y} + \frac{\partial v}{\partial x}\right) & \frac{1}{2}\left(\frac{\partial u}{\partial z} + \frac{\partial w}{\partial x}\right) \\ \frac{1}{2}\left(\frac{\partial v}{\partial x} + \frac{\partial u}{\partial y}\right) & \frac{\partial v}{\partial y} & \frac{1}{2}\left(\frac{\partial v}{\partial z} + \frac{\partial w}{\partial y}\right) \\ \frac{1}{2}\left(\frac{\partial w}{\partial x} + \frac{\partial u}{\partial z}\right) & \frac{1}{2}\left(\frac{\partial w}{\partial y} + \frac{\partial v}{\partial z}\right) & \frac{\partial w}{\partial z} \end{bmatrix} \tag{3.5}$$

The Reynolds number calculated inside the capillary for single phase flow is given as follows:

$$Re = \frac{\bar{u} d_c}{\nu} \tag{3.6}$$

where d_c denote the capillary diameter and $\bar{u}_x$ denotes the average axial velocity. For the considered capillary and based on the averaged axial velocity, the calculation of the Reynolds number shows $Re \leq 2300$ for various operating pressure, and thus refers to laminar flow inside the capillary. The calculations of the Reynolds number for different operating parameters will be explained later.
The viscous term in Navier-Stokes equation (Eq. 3.2) is dominated when the flow is in laminar conditions. The inertia term in dead-end configuration is

included in the calculation, as the derivative of the velocity in the flow direction is not negligible. That makes a direct solution of the governing equations very expensive, hence they are iteratively solved in the computational domain.

3.2.2 Flow in capillary with porous wall

The capillary membrane filtration process applied in water treatment makes use of the porous structure of the wall. For the backwash process operated in dead-end mode, the driving force is generated by exposing the capillary to high outer pressure that forces the water to flow through the porous wall in an inside-out direction. The magnitude of the driving force depends on many factors, including the pressure drop in the capillary. Predicting the behaviour of the flow inside the capillary adjacent to the porous wall is essential to calculate the pressure drop and loss both in the capillary and the porous wall. Consequently, the permeate flux can be estimated, and the performance of the backwash process can be improved and thus energy consumption can be reduced. The complexity of the interaction between the free and porous flow regimes highlights the need for the development of a CFD model which can optimise the backwash operating parameters. Thus, the CFD model provides a library of boundary conditions that predicts the corresponding pressure drop in the capillary and the axial and radial velocity profile with consideration of membrane fouling. Furthermore, the model investigates the influence of the membrane's characteristics and the operating parameters on the performance of the backwash process.

The flow inside a tube with a porous wall has been under investigation for long time. Early models to solve the Navier-Stokes equation for laminar flow in a porous tube were proposed by Berman [73] and Yuan [74] and extended by Bernales [75]. Berman [73] presented a solution to the two-dimensional model for laminar flow in channels with uniform wall suction. This study was extended to cylindrical coordinates to investigate suction as well as injection in flow along a porous channel [74]. There is also a description of the flow in the porous wall for a circular tube with uniform suction [76, 77, 78] and for different

permeability [79]. Further investigation was carried out for a tube with variable wall suction [80]. Karode [81] derived an analytical solution to the pressure drop in a rectangular slit and cylindrical tube with porous walls for constant permeability. This expression was in agreement with the solution proposed by Berman [73]. Another expression for the pressure drop and velocity was derived by Kim [82]. It is obtained by applying the perturbation theory to a dead-end cylindrical porous tube. More recently [83], a one-dimensional model was introduced to determine the fluid in a porous channel with wall suction or injection, based on the analytical solution proposed by Berman and Yuan [73, 74].

Linking Darcy's and Stokes' equations [84] contributes to understanding of interfacial phenomena in coupled free and porous flow regimes applicable to cross flow filtration. Various methods for coupling the free flow and the flow in permeable wall models were introduced and the strengths and weaknesses of each method were discussed [85]. An analytical solution to the coupling between the transmembrane pressure and velocity in tubular membrane is proposed and validated with direct numerical simulation [86]. Stokes' equation models free flow dynamics, while Darcy's equation models non-isothermal, non-inertial and incompressible flow in a porous medium. Darcy's law was extended to non-Stokes flow and the resulting relation between pressure gradient and mass flux in porous media is presented [87].

In order to provide better insight into the flow and pressure drop in a membrane channel with a porous wall, CFD models were developed which provides more detailed information about the physical phenomena accompanying the filtration process [88]. Another work predicts the pressure drop and permeate flux in hollow fibre using a simplified model equation [89].
The optimisation of the backwash process is linked to developing a numerical model which accurately describes the pressure drop under various boundary conditions and the flow through the porous wall of a capillary membrane in ultrafiltration module. Furthermore, adjusting the correct boundary conditions for further simulations of the backwash process requires the knowledge of the

velocity distribution in the vicinity of the membrane surface. In order to incorporate the flow in the porous wall of the capillary, a source term (S) is added to the momentum equation [90]. The porous wall is simplified as a homogeneous and isotropic medium. A steady state flow is taken into account. Thus, for incompressible flow and after some rearrangements, Eq. 3.2 can be written in the following form:

$$(\boldsymbol{u} \cdot \nabla)\boldsymbol{u} = -\frac{1}{\rho}\nabla p + \nu\nabla^2\boldsymbol{u} + \boldsymbol{S} \tag{3.7}$$

ν denotes the fluid kinematic viscosity $\nu = \frac{\mu}{\rho}$. Term S in Eq. 3.7 is divided into two parts, a viscous loss term D and an inertial loss term β as in Eq 3.8. These two terms represent the properties of the fluid and the porous wall.

$$\boldsymbol{S} = -(\nu D + \frac{1}{2}\left|\boldsymbol{u}\right|\beta)\boldsymbol{u} \tag{3.8}$$

The pressure drop has a proportional relationship to velocity in the viscous term and squared velocity in the inertial term, whose effects become dominant as the velocity increases. The viscous parameter is calculated as the inverse of permeability whereas the contribution of the non-linear Forchheimer term is quite small and not considered ($\beta = 0$) for the studied cases since the Reynolds number is smaller than 1, ($Re < 1$) in the porous wall, [91].

3.2.3 Pressure-velocity coupling

Solving the pressure-velocity coupling which appears in the momentum equation requires a suitable algorithm to calculate the flow variables. For the steady state problem and incompressible flow, a commonly used algorithm called SIMPLE (Semi-Implicit Method for Pressure-Linked Equations) [92] is implemented. This procedure is based on solving the momentum equation using a pressure gradient estimated according to the previous or initial value to obtain the velocity field. Then, the pressure equation is formulated and the pressure value is calculated. Regarding the new pressure, the velocity field is corrected. This process is iteratively repeated to lead the equations towards convergence. In other words, the change in the variables from one iteration to the next is

reduced to a value below given tolerance. Fig. 3.2 shows the solution procedure of a SIMPLE algorithm used for single phase flow in the current thesis.

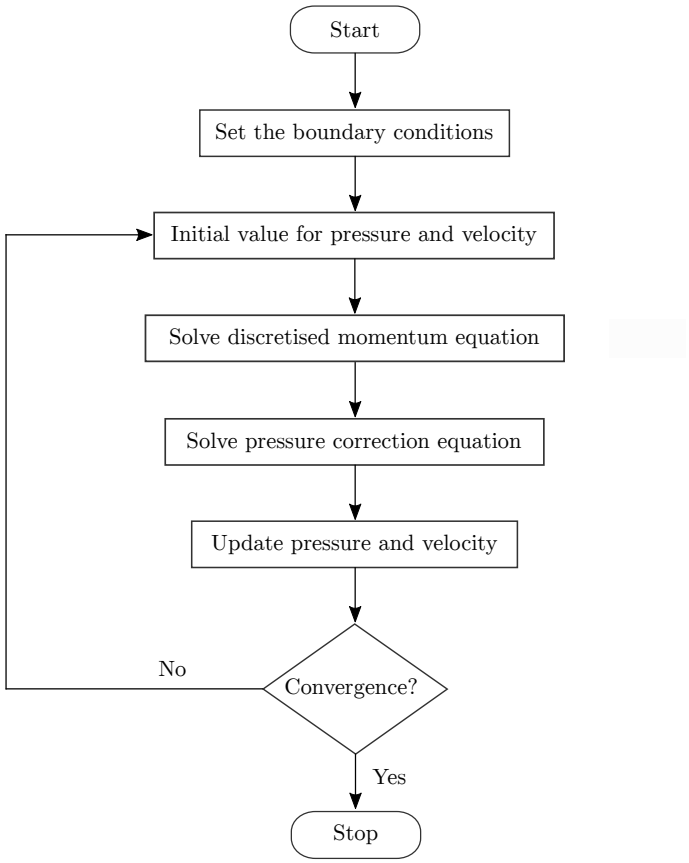

Figure 3.2: Flow chart for SIMPLE algorithm.

3.2.4 Modelling and boundary conditions

A single phase, steady-state, laminar and incompressible flow in a capillary membrane with a porous wall was carried out. The geometry is illustrated in Fig. 3.3. The capillary length is 980 mm and it has an inner and outer diameter of 1.4 mm and 2.3 mm, respectively. The equations above will be solved in a computational domain, discretised in 11 Mio structured control volume. This high mesh resolution covers the whole computational domain and ensures a mesh independent solution. Further mesh refinement has no influence on the solution and only increases computational efforts and time. The element size is

uniformly distributed in the capillary inside the capillary membrane and can be seen in Fig. 3.4. The meshing is generated in ANSYS-ICEM with *mesh extension and read in OpenFOAM using the command fluentMeshToFoam. The RenumberMesh command is used to rearrange the numbering of the cells in all time directories which reduces the computational efforts. Once the mesh is

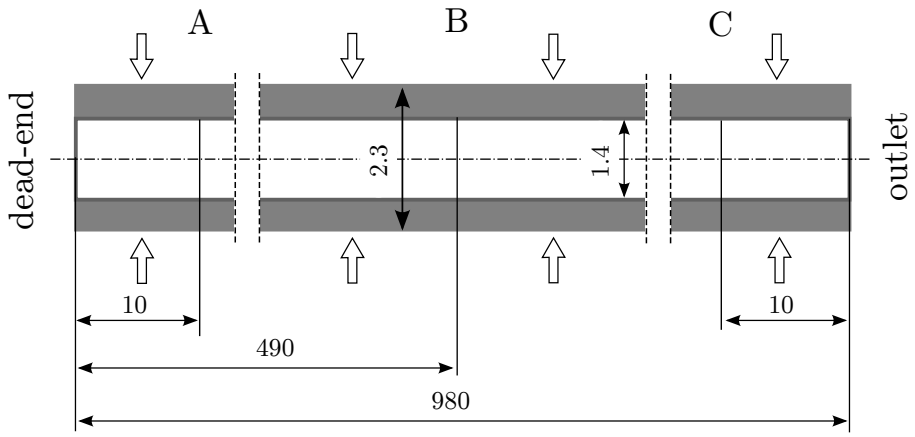

Figure 3.3: Computational domain of the capillary membrane with porous wall.

generated, the governing equation in the previous section is discretised by the Gauss theorem to convert the volume integral to surface integral. Discretisation of the convection term of the yielding governing equations is done via the upwind scheme which ensures the boundedness and stability of the solution with acceptable accuracy. The Gauss linear scheme is used for the discretisation of the diffusion term. The source term which is considered for the flow in a porous wall is treated explicitly in terms of the temporal discretisation. The resulting algebraic equations are solved based on the Semi-Implicit Method for Pressure Linked Equations, known as the SIMPLE algorithm [92], to find a converged solution. The required under-relaxation factors for velocity and pressure are chosen as 0.3 and 0.7, respectively. These small under-relaxation factors slow down the convergence speed; however, they also ensure the solution's stability and dampen the solution process. The overall iteration is assumed to be converged when the residual for each equation is below 10^{-5}.

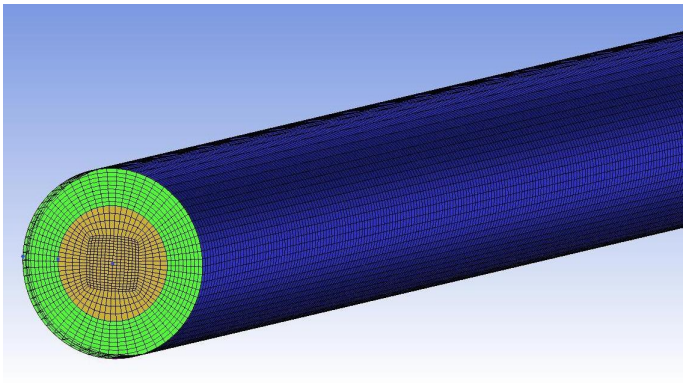

Figure 3.4: Discretisation of the computational domain.

The porous wall is homogeneous, isotropic and characterised by its viscous resistance D in Eq. 3.8, or permeability ψ. Moreover, the used fluid water is assumed to be incompressible, isothermal and with a constant density and viscosity of 1000 kg/m^3 and 10^{-6} m^2/s, respectively. The flow is laminar for all the simulated conditions. For each parameter, such as pressure or permeability, a steady state simulation is carried out resulting in the steady state flux, pressure drop and axial as well as radial velocity distribution. The boundary conditions are adjusted to match the operating conditions of the experiment. For all the simulations, the driving force for the water is pressure gradient. Therefore, the pressure has a constant value at the inlet, namely operating pressure, and an atmospheric pressure at the outlet. No-slip velocity is set at the dead-end, which is treated as a wall. The components of the velocity gradient are considered to be zero. Different permeability values for the porous wall are taken into account. This variation of the capillary permeability takes the formation of the fouling layer into consideration since this layer has a porous structure. The range of the simulated permeability is detailed in Table 3.1.

Table 3.1: Range of the studied operating parameter.

Parameter	Simulated range
Permeability $L/(m^2\ h\ bar)$	80-400
Pressure bar	1-4

The investigation of shear stress inside the capillary membrane has a significant influence on understanding the detachment mechanism of the adhered particles. Removing particles deposited firmly on the membrane surface requires high shear stress. This shear stress is induced from the change in the hydrodynamic conditions near the capillary wall. The magnitude of the needed shear stress depends strongly on the degree of stickiness of the deposited layer and is determined by the velocity gradient inside the capillary. Moreover, prediction of the shear stress in the capillary during backwashing may improve removal of the cake layer and prevent membrane fouling in addition to enhancing the flux. The shear stress near the membrane surface reflects the efficiency of deposited layer removal and the mechanical force required. Therefore, the shear stress on the adhered particles is characterised for various operating pressures. For this reason, the thickness of the deposited layer and its position are taken into account by different bulge arrangements. These bulges are impermeable patches with a curved form which are not penetrated by backwash water, as illustrated in Fig. 3.5.

Section I shows three bulges at different distances from the dead-end and on the upper as well as the lower part of the capillary. Section II shows the same bulges as in section I, but with different lengths. Section III has two bulges in close succession on the lower part of the capillary. Section IV has two bugles opposite each other. These configurations appear as result of cake layer formation during filtration.

The shear stress is calculated using the velocity gradient at the desired position and the viscosity of water: Eq. 3.3. It is investigated in a steady state condition under two operating pressures, 2 and 3 bar in the capillary membrane, disregarding the flow in the porous walls. The main assumption regarding the bulges is that they neither change their thickness nor detach from the membrane surface in the course of the backwash process. They are treated here as fixed cake layer with a constant thickness of about 30 % of the capillary radius. Moreover, they are randomly distributed along the capillary length where different water velocities are expected, as seen in Fig. 3.5.

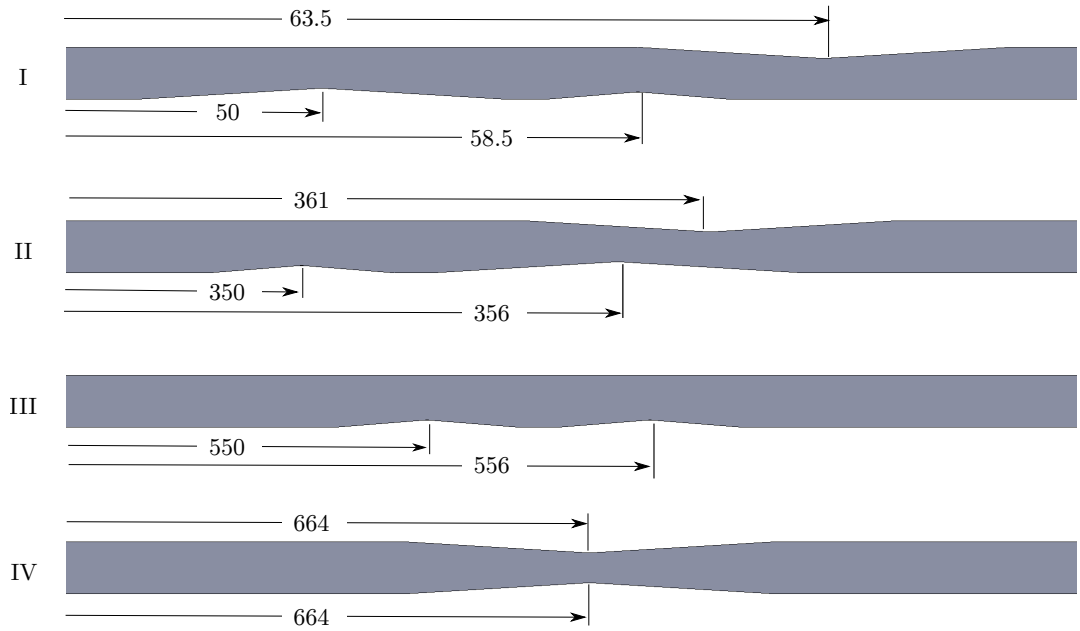

Figure 3.5: The capillary membrane with tightly adhered particles (bulges) in different positions and arrangements. The distance from the dead-end to each bulge is shown in the corresponding section whereas the hidden part of the capillary has straight, clean walls.

3.3 Flow characterisation for multiphase flow

Multiphase flow can be seen in many industrial applications, including chemical, food and water purification. A wide range of flows and patterns are expressed by the definition of multiphase flow, for example gas-solid, gas-liquid and liquid-solid. The need for a numerical solution to multiphase flow problems has become more urgent, especially with the increasing usage of matched flows. Analysis and fundamental understanding of these flows a essential for the optimisation and development of the related processes. Detailed information about particle behaviour and the influence of the flow on particle distribution is also obtained numerically by deriving the basic equations of the multiphase flow.

Multiphase flow is divided into two approaches according to the treatment of the dispersed phase. In both approaches the flow field is computed as a

single-phase flow using Navier-Stokes equations. Thus, it can be split into:

- Eulerian-Lagrangian approach: the dispersed phase is treated as solid particles with a constant shape and size. Each particle is individually tracked by calculating its trajectory through the computational domain using the particle equation of motion. The carrier phase is treated as continuous fluid and described by Navier-Stokes equations. Thus, the solution of the coupled equations gives detailed information about each particle, such as its position at a certain time, velocity, acceleration and local volume fraction. This approach demands significant computational effort and becomes unsuitable and expensive when the system contains a large number of particles.

- Eulerian-Eulerian approach: each phase is treated as a continuous fluid and described by a set of Navier-Stokes equations. However, the interaction among the considered phases appears in the modelling through an additional term which accounts for the momentum exchange of the phases. Then, the resulting equations can be solved by a suitable averaging procedure such as time, volume or ensemble averaging [93, 94]. This procedure deals with the volume fraction occupied by each phase in every control volume in the computational domain and thus the sum of the volume fractions of the involved phases in a control volume is equal to one. The limitation of this approach is the accurate modelling of the involved forces in the calculation, which may add some complexities to the model.

The Eulerian approach is applicable to a wide range of multiphase flows and is more efficient than the Lagrangian approach in terms of costs and restriction to certain flow patterns. Thus, the Eulerian approach allows the modelling of a higher number of dispersed phases with acceptable computational effort and reliable results, as the number of equations depends on the number of phases and not on the number of particles. This approach is chosen for the numerical simulations carried out in this thesis.

3.3.1 Continuity and momentum conservation

Description of the particle motion in the capillary membrane during the backwash process is based on the modelling of the multiphase flow using the Eulerian-Eulerian approach. Several authors [95, 96] worked on the modelling of the multiphase flow. Ishii [97] divided the two-phase flow into three categories according to the flow regime, namely separated flows, mixed or transitional flows, and dispersed flows, and derived the corresponding governing equations. Issa [98] developed the solution algorithm for the two-phase flow prepared by Ishii [97] to improve its performance at regions where the volume fraction is zero.

To derive the mathematical model, it is assumed that the involved phases consist of one continuous phase and number of dispersed phases. All phases are treated as an interpenetrating continuum. In addition, the implemented approach assumes that all phases share the same pressure field but that each phase has its own velocity field. The dynamic behaviour of each phase in the considered domain is obtained by solving the average mass and momentum conservation equations for each phase. These conservation equations are valid within each phase up to the interaction between the phases. The dispersed phase is characterised by applying the average process for each phase over the control volume. The averaging approach introduces the phase fraction r_α into the mathematical model, which is the probability that phase α is present at a certain point at a given time and space. The volume fraction of phase α is defined as the volume occupied by the particles classified as phase α in a unit volume.

$$r_\alpha = \frac{V_\alpha}{V} \tag{3.9}$$

V_α is the volume of phase α. Thus, the volume fraction of the continuous phase is calculated as:

$$r_c = (1 - \sum r_\alpha) \tag{3.10}$$

When all the phases share the same pressure field, the mixture velocity is defined as follows:

$$\boldsymbol{u} = (r_c \boldsymbol{u}_c + \sum \boldsymbol{u}_\alpha r_\alpha) \tag{3.11}$$

the term $\sum \boldsymbol{u}_\alpha r_\alpha$ represents the sum of velocities of the involved phases multiplied by the corresponding volume fraction.

Mass conservation

The continuity equation for each phase α in multiphase flow for transient conditions and incompressible flow is given by:

$$\frac{\partial(r_\alpha)}{\partial t} + \nabla \cdot (r_\alpha \boldsymbol{u}_\alpha) = 0 \tag{3.12}$$

Momentum conservation

The conservation of the momentum of each phase in the system is given by

$$\frac{\partial(r_\alpha \boldsymbol{u}_\alpha)}{\partial t} + \nabla \cdot (r_\alpha \boldsymbol{u}_\alpha \boldsymbol{u}_\alpha) = -\nabla \cdot (r_\alpha \boldsymbol{\tau}_\alpha^{eff}) - \frac{r_\alpha}{\rho_\alpha} \nabla p + r_\alpha \boldsymbol{g} + \frac{\boldsymbol{M}_\alpha}{\rho_\alpha} \tag{3.13}$$

The r.h.s. terms in Eq. 3.13 represent, respectively, the effective Reynolds stress tensor τ_α^{eff} which is decomposed as

$$\boldsymbol{\tau}_\alpha^{eff} = -\nu_\alpha^{eff} (\nabla \boldsymbol{u}_\alpha + \nabla \boldsymbol{u}_\alpha^T - \frac{2}{3} \boldsymbol{I} \nabla \cdot \boldsymbol{u}_\alpha) + \frac{2}{3} \boldsymbol{I} k_\alpha \tag{3.14}$$

here k_α is the turbulent kinetic energy of phase α and the effective viscosity ν_α^{eff} of phase α is calculated by Boussinesq hypothesis [99] and models the strain rate. It is decomposed into turbulent and molecular viscosity

$$\nu_\alpha^{eff} = \nu_\alpha + C_t^2 \nu^t \tag{3.15}$$

The pressure gradient and gravity in addition to the interfacial momentum exchange term $\frac{M_\alpha}{\rho_\alpha}$, which represents the momentum exchange between the phases, are terms of the r.h.s. in Eq. 3.13 as well.

3.3.2 Interaction forces

The motion of the particles is captured by modelling the interfacial momentum exchange between the fluid and the particles. This interaction is expressed by assembling the acting forces at the interface between the continuous and dispersed phases. These forces are responsible for drag, lift and virtual mass. Interfacial momentum is also known as the closure term in the momentum equation. It can be decomposed into:

$$\boldsymbol{M}_\alpha = \boldsymbol{M}^D + \boldsymbol{M}^L + \boldsymbol{M}^V \tag{3.16}$$

where $\boldsymbol{M}^D$ denotes drag momentum rate, $\boldsymbol{M}^L$ denotes lift momentum rate and $\boldsymbol{M}^V$ denotes the virtual mass momentum rate. The corresponding forces

$$\frac{\boldsymbol{M}_\alpha.V}{r_\alpha} = \boldsymbol{F}^D + \boldsymbol{F}^L + \boldsymbol{F}^V \tag{3.17}$$

here is V the volume of dispersed phase, $\boldsymbol{F}^D$, $\boldsymbol{F}^L$ and $\boldsymbol{F}^V$ are the drag, lift and virtual mass forces, respectively.

- Drag force
  The Drag force is the most important and dominating force in the particle-fluid interaction system. It arises due to the relative motion between the particle and the fluid around it. It depends on particle size d_p and the relative velocity between the dispersed and the continuous phases u_r. The drag force for a spherical, non-deformable and constant particle diameter reads:

  $$\boldsymbol{M}^D = \frac{3}{4}\frac{\rho_c}{d_\alpha} r_\alpha C_D \left|\boldsymbol{u}_{r,\alpha}\right| \boldsymbol{u}_{r,\alpha} \tag{3.18}$$

  where d_α is the particle diameter, C_D is drag coefficient as calculated as a function of the particle's Reynolds number which depends on the relative

velocity and particle diameter and is computed as follows:

$$Re_\alpha = \frac{|\boldsymbol{u}_{r,\alpha}| d_\alpha}{\nu_\alpha} \tag{3.19}$$

For small Reynolds numbers ($Re_\alpha < 1000$) the particles fall in a viscous dominant flow regime and the drag coefficient C_D is calculated according to Schiller and Naumann [100]. Otherwise, the particles fall in the Newton regime where friction is dominating and independent of the Reynolds number. Therefore, it is considered approximately constant.

$$C_D = \begin{cases} \frac{24}{Re_\alpha}(1 + 0.15 Re_\alpha^{0.687}) & Re_\alpha \leq 1000 \\ 0.44 & Re_\alpha > 1000 \end{cases} \tag{3.20}$$

The relative velocity is defined as the difference between the dispersed phase and the continuous phase and given as:

$$\boldsymbol{u}_{r,\alpha} = \boldsymbol{u}_\alpha - \boldsymbol{u}_c \tag{3.21}$$

- Lift force

  A particle moving in a shear flow experiences lateral force [101]. This force has a considerable impact on the particle in a high shear flow and influences significantly the radial distribution of the particles. It appears due to the non-uniform velocity and pressure distribution around the particle and acts in a perpendicular direction to the flow. It is expressed as follows:

$$\boldsymbol{M}^L = -C_{L,\alpha} \rho_c r_\alpha \boldsymbol{u}_{r,\alpha} \times (\nabla \times \boldsymbol{u}_c) \tag{3.22}$$

  where $C_{L,\alpha}$ is the lift coefficient which is obtained analytically from simplified cases or through empirical correlation. In this study, it is estimated using a constant value of $C_{L,\alpha} = 0.5$ according to Silva [102]. Lift force drives to an equilibrium position either towards the axis if the fluid lags the flow or towards the wall if the particles lead the flow . This particle motion causes what is called the tubular pinch effect.

- Virtual mass
  Due to the mass of fluid in the particle's vicinity, when the particle accelerates, the fluid in its vicinity accelerates as well since the particle displaces the fluid around it, causing virtual mass force. Thus, virtual mass force depends on the relative acceleration between the particle and the fluid. Ignoring virtual mass force in the modelling leads to rapid acceleration of the particle. However, virtual force becomes unimportant when the particle has a small diameter and similar inertia to the carrier fluid. The force is stated as:

$$\boldsymbol{M}^V = C_v \rho_c r_\alpha (\frac{D\boldsymbol{u}_c}{Dt} - \frac{D\boldsymbol{u}_{r,\alpha}}{Dt}) \tag{3.23}$$

  C_v is the virtual mass coefficient which is adjusted to 0.5 [102].

  For simplification purposes and as first step towards analysing the particle behaviour during the backwash process, some other forces like Van der Waals and inter-particle electrostatic forces arise but their effects on the particles behaviour and distribution are not considered in this approach. Since it is assumed that the particles are detached from the wall at the beginning of the simulation, adhesive and friction force are also not taken into account.

Stokes number

The Stokes number is defined as the ratio between the particle response time Φ_d and the flow response time Φ_c and is formulated as

$$St = \frac{\Phi_d}{\Phi_c} \tag{3.24}$$

It represents the time needed by a particle to respond to the change in the surrounding flow velocity. This number is a very significant parameter regarding the choice of an appropriate model for simulating the dispersed phase. For a

spherical particle, response time for the particles is calculated as:

$$\Phi_d = \frac{\rho_d d_\alpha^2}{18\mu_c} \tag{3.25}$$

here ρ_d denotes the density of the particle, d_α denotes the particle diameter and μ_c is the dynamic viscosity of the continuous phase. Response time for the flow is respectively:

$$\Phi_c = \frac{d_c}{u_x} \tag{3.26}$$

where d_c and u_x are the diameter of the capillary and mean axial velocity, respectively. If $St << 1$, the particle has a small response time compared to the characteristic flow time and it tends to follow the flow. Thus, the particle is coupled to the fluid and the relative velocity between the phases is accordingly small. However, if $St >> 1$, the particle velocity is barely influenced by the flow.

Adjusting the time step

The time step can be controlled by computing the Courant number. This is a significant factor affecting the stability and computational time of transient calculation. Co is defined in [103] as follows:

$$Co = max\left\{\left|\frac{u_c \Delta t}{\Delta x}\right|, \left|\frac{u_\alpha \Delta t}{\Delta x}\right|\right\} \tag{3.27}$$

Δt denotes the time step and Δx is the distance between the centre of two neighbouring cells in the specified direction. The Courant number is also calculated based on the relative velocity between the dispersed and the continuous phases as following:

$$Co_r = \left|\frac{u_r \Delta t}{\Delta x}\right| \tag{3.28}$$

The Co must be less than unity $Co < 1$ to ensure accurate results, improve the stability of the solution procedure and establish acceptable convergence. However, a very small Co lead to the loss of computational time. In other words, if the mesh of the computational domain is very fine (i.e. Δx is very small), the denominator of Eq. 3.27 is correspondingly small. For a constant Co this leads to a small time step during the running of the simulation, and vice versa.

3.3.3 Solution procedure for two-phase flow

After applying the finite volume method to the discretised Navier-Stokes equations, the resulting set of the coupled pressure-velocity equation is solved by implementing a PISO algorithm (Pressure implicit with splitting of operator) which was originally presented by Issa [104]. This method involves momentum predictor and pressure corrector steps. Thus, the solution sequence can be summarised as in Fig. 3.6.

3.3.4 Population balance equation

In order to consider the polydispersity in the capillary membrane during backwash and observe a the distribution of the potential agglomerates, the population balance equation (PBE) is introduced in this section. This method describes the evolution of the multiphase flow for a large number of particles over time. It accounts for the interaction of particles among themselves, so that the particles can aggregate into larger particles and breakup into smaller particles. These processes are considered by deriving an adequate equation for the particle distribution function (PDF) and choosing suitable internal and external coordinates, such as particle volume and spacial coordinate, respectively. External coordinate refers to the motion of a particle in physical space whereas internal coordinate concerns internal properties. The general form of the population balance equation for particle distribution function $f(x, \upsilon, t)$ in volume υ as defined by Ramkrishna [105], is:

$$\frac{\partial f(\boldsymbol{x}, \upsilon, t)}{\partial t} + \nabla.[\boldsymbol{u}_\alpha f(\boldsymbol{x}, \upsilon, t)] = S_k(\boldsymbol{x}, \upsilon, t) \tag{3.29}$$

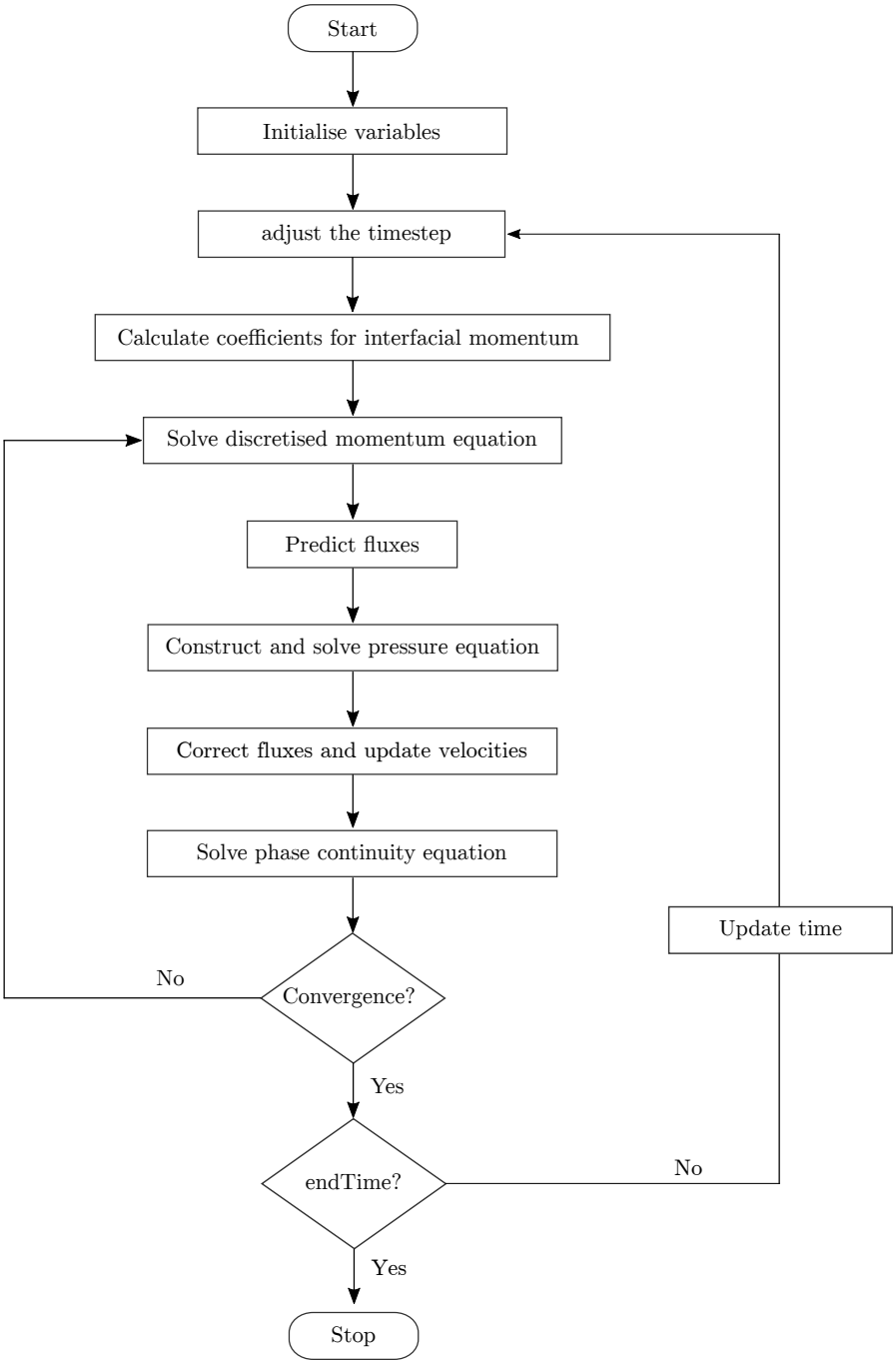

Figure 3.6: Flow chart for PISO algorithm.

here S_k is the source term due to the aggregation and breakage and is given as

$$S_k(\boldsymbol{x}, v, t) = B_a - D_a + B_b - D_b \tag{3.30}$$

and $f(\boldsymbol{x}, v, t)$ for monovariate distribution is the number of particles with particle volume v per unit volume at position $\boldsymbol{x}$ and time t, which may also be called particle distribution function. The r.h.s. of Eq. 3.29 includes the birth and death of particles due to their interactions. On the l.h.s. of the Eq. 3.29 is the convection of the particles for each particle volume v. $\boldsymbol{x}$ and v are external and internal coordinates, respectively. Eq. 3.29 includes an integral form resulting from the birth and death terms as well as the differential form from the transport equation. The birth rate of particles due to aggregation is:

$$B_a = \frac{1}{2}\int_0^v e(v - v', v')f(\boldsymbol{x}, v - v', t)f(\boldsymbol{x}, v', t)dv' \tag{3.31}$$

The death rate of particles due to aggregation is:

$$D_a = \int_0^\infty e(v, v')f(\boldsymbol{x}, v, t)f(\boldsymbol{x}, v', t)dv' \tag{3.32}$$

and $e(v, v')$ aggregation frequency. The birth rate of particles due to breakage is:

$$B_b = \int_v^\infty \vartheta(v')b(v')P(v|v')f(\boldsymbol{x}, v', t)dv' \tag{3.33}$$

$\vartheta(v')$ is the daughter particle size distribution and $P(v|v')$ is the conditional probability of particle v' generating a daughter particle v. The death rate of particles due to breakage is:

$$D_b = b(v)f(\boldsymbol{x}, v, t) \tag{3.34}$$

and $b(v)$ is the breakup frequency.

3.3.5 PBE solution methods

The population balance equation (PBE) is a complicated mathematical form due to the inclusion of internal coordinates which change continuously due to changes in particle properties resulting from breakup and aggregation. Many methods have been proposed to treat this complexity since a direct solution is computationally very expensive. These include, among others, the Monte Carlo

method [106, 107], the classes method (CM) [108, 109], the quadrature method of moments (QMOM) [110, 111] and the direct quadrature method of moments (DQMOM) [112]. The direct quadrature method of moments (DQMOM) reduces the computational expense since few abscissas can describe particle size distribution. (DQMOM) uses quadrature approximation to the particle distribution function and is based on tracking some points of the distribution function which represent the system instead of tacking the whole (PDF). These points are weights and abscissas of a quadrature approximation and can be calculated in the computational domain by solving their transport equation.
The summation of the Dirac delta function transforms the integral expression of the particle distribution function (PDF), $f(\boldsymbol{x}, \upsilon, t)$, which appears in the population balance equation, [102, 113], and for a monovariate case, the function $f(\boldsymbol{x}, \upsilon, t)$ is approximated by Riemann approach to:

$$f(\boldsymbol{x}, \upsilon, t) = \sum_{\alpha=1}^{n} w_\alpha(\boldsymbol{x}, t)\delta[\upsilon - \xi_\alpha(\boldsymbol{x}, t)] \tag{3.35}$$

here δ is the Dirac delta function and n is the number of the delta function or the number of the quadrature n-point which will be tracked. Weighted abscissas is defined as $\varsigma_\alpha = \xi_\alpha w_\alpha$. The transport equations of the weights and weighted abscissas in the (DQMOM) approximation can be formulated:

$$\frac{\partial w_\alpha(\boldsymbol{x}, t)}{\partial t} + \nabla[\boldsymbol{u}_\alpha(\boldsymbol{x}, t) w_\alpha(\boldsymbol{x}, t)] = \theta_\alpha \qquad \alpha = 1, .., n \tag{3.36}$$

$$\frac{\partial \varsigma(\boldsymbol{x}, t)}{\partial t} + \nabla[\boldsymbol{u}_\alpha(\boldsymbol{x}, t) \varsigma(\boldsymbol{x}, t)] = \kappa_\alpha \qquad \alpha = 1, .., n \tag{3.37}$$

θ_α and κ_α are source terms of the (DQMOM) transport equations for weight and weights abscissas, respectively. Inserting Eq. 3.35 in the population balance equation Eq. 3.29 includes the derivation of the Dirac delta distribution [112]. Taking the moments of the resulting equation and with some mathematical manipulations together with the transport equations for weights and weighted

abscissas in Eqs. 3.36 and 3.37, the linear system is given [102]:

$$(1-k)\sum_{\alpha=1}^{n}\xi_{\alpha}^{k}\theta_{\alpha}+k\sum_{\alpha=1}^{n}\xi_{\alpha}^{k-1}\kappa_{\alpha}=S_{k}^{(n)} \qquad k=0,..,2n-1 \tag{3.38}$$

The solutions of the Eqs. 3.38, 3.36 and 3.37 are fully coupled. Solving Eqs. 3.36 and 3.37 in $(\boldsymbol{x},t)$ domain requires the source terms θ_{α} and κ_{α} which can be found by solving the linear system Eq. 3.38 at every point of the computational domain.

$$\begin{aligned} S_{k}^{(n)} &= \frac{1}{2}\sum_{\alpha=1}^{n}\sum_{\beta=1}^{n}[(\xi_{\alpha}+\xi_{\beta})^{k}-\xi_{\alpha}^{k}-\xi_{\beta}^{k}]e(\xi_{\alpha},\xi_{\beta})w_{\alpha}w_{\beta} \\ &\quad +\sum_{\alpha=1}^{n}b(\xi_{\alpha})w_{\alpha}[\vartheta(\xi_{\alpha})\pi_{k}(\xi_{\alpha})-\xi_{\alpha}^{k}] \end{aligned} \tag{3.39}$$

where $S_{k}^{(n)}$ is the k^{th} moment of the source term approximated by n-point quadrature. This term contains the considered processes (aggregation and breakage) and $\pi_{k}(\xi_{\alpha})$ is defined as:

$$\pi_{k}(\xi_{\alpha})=\int_{0}^{\xi_{\alpha}}\upsilon^{k}P(\upsilon|\xi_{\alpha})d\upsilon \tag{3.40}$$

Then the characteristic diameter d_{α} can be calculated:

$$d_{\alpha}=\left(\frac{6\xi_{\alpha}}{\pi}\right)^{1/3} \tag{3.41}$$

and the overall phase fraction of the dispersed phase:

$$\sum_{\alpha=1}^{n}r_{\alpha}=\int_{0}^{\infty}\upsilon f(\boldsymbol{x},\upsilon,t)d\upsilon\simeq\sum_{\alpha=1}^{n}\xi_{\alpha}w_{\alpha}=\int_{\alpha=1}^{n}\varsigma_{\alpha} \tag{3.42}$$

When the solution of Eq. 3.39 is found, any internal variable can be calculated. By coupling the CFD and PBE, the characteristic diameter can be obtained from Eq. 3.41 and Sauter diameter from Eq. 3.43:

$$d_{s}=\left(\frac{6}{\pi}\right)^{1/3}\frac{\sum_{\alpha=1}^{n}\xi_{\alpha}w_{\alpha}}{\sum_{\alpha=1}^{n}\xi_{\alpha}^{2/3}w_{\alpha}} \tag{3.43}$$

Simulating the polydisperse flow and including the particle-particle interaction can be achieved by coupling Eulerian multiphase flow and the population balance equation using velocity. The work done by Rusche [114] is extended to consider multiphase flow and then coupled with DQMOM [112] to solve the population balance equation. The coupling CFD-PBE is implemented in OpenFOAM code to obtain polydispersed multiphase flow solver [102, 113]. These studies provide the discretisation procedure and formulation of CFD-PBE coupling algorithms in OpenFOAM. The code is then used for the simulations of polydispersed flow which are conducted in this thesis for tracking the evolution of the particle size distribution.

3.3.6 Modelling and boundary conditions

Defining the boundary conditions which match the realistic conditions is crucial for carrying out the simulations. For the simulation of multiphase flow, it is assumed that the computational domain is constrained to the flow inside the inner diameter of the capillary membrane and not inside the porous wall. This assumption saves computational costs in terms of both time and storage requirements. However, the wall-normal velocity of the water entering the capillary is calculated by solving the coupling of Navier-Stokes and Darcy-Forchheimer equations in the porous wall as defined in the previous section, see section 3.2.4. The analysis of the backwash process is performed by considering three capillary configurations operated in dead-end mode. These models have a length of 980 mm and an inner diameter of 1.4 mm.

- The first capillary configuration is a theoretical particle distribution. It assumes that the particles are suspended and homogeneously distributed in the water without adhesive and friction against the wall. The volume fraction of the particles at the beginning of the simulation is considered to be 10 % of the capillary's total volume. This configuration represents the behaviour of the suspended particles within the process of backwashing. It may appear in part of the capillary in addition to other particle distributions. It is step towards building and developing a numerical

model, in addition to investigating and characterising particle motion inside the dead-end capillary. This configuration is illustrated in Fig. 3.7.

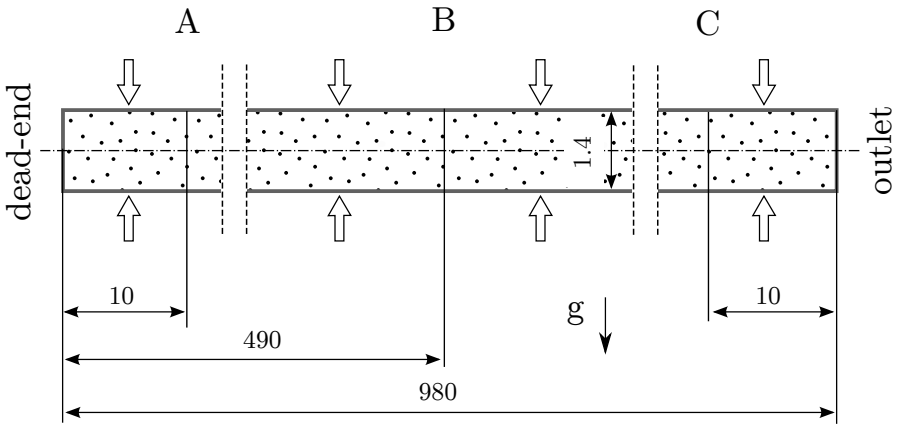

Figure 3.7: The homogeneous particle distribution inside the capillary membrane and the position of control lines A, B and C for the evaluation of velocity and particle distribution during backwashing. All dimensions in the figure are in mm.

The water is considered as a continuous phase whereas the particles are treated as a dispersed phase with uniform particle size. The computational domain is subdivided in 3 Mio of finite hexahedral volumes by generating uniformly distributed mesh across and along the considered domain in Ansys-ICEM. This level of mesh refinement fulfills the mesh sensitivity analysis and is adopted to predict the solution apart from the mesh distribution and number.

- The second capillary configuration involves significantly realistic backwash process conditions in terms of the initial particle distribution inside the capillary. This distribution can be encountered after running a filtration process. In this type, the particles are deposited on the inner wall of the capillary membrane forming a ring with a thickness of 125 μm. The highest value for the particle volume fraction, which also is defined as packing density, is 0.5, as seen in Fig. 3.8. Even particle distribution is realistic particle distribution and is delivered by the experimental measurements as a result of performing a filtration process on a single

capillary. Hereby, experimentally defined particle distribution and particle size in the capillary are applied as initial conditions. This particle

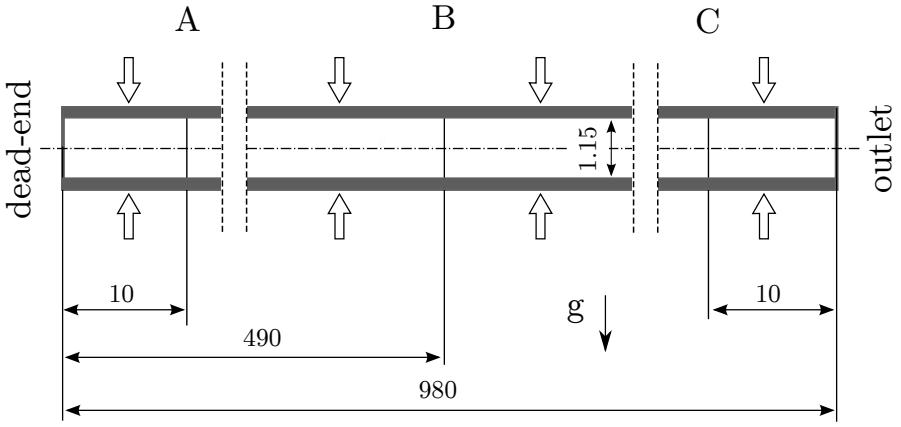

Figure 3.8: Even particle distribution inside the capillary membrane after running a filtration process. The initial packing density of the deposited particles is 0.5 and the thickness is 0.125 mm. The positions of control lines A, B and C for the evaluation of velocity and particle distribution during backwash are similarly defined. All dimensions in the figure are in mm.

distribution assumes an equal build-up of the cake layer which is assumed to positively influence the efficiency of the backwash process [13]. Additionally, for the current configuration, the capillary is a non-porous wall and composed only of the inner diameter of 1.4 mm. Here, 7 Mio structured control volumes are necessary to cover the computational domain and ensure a mesh independent solution. In the vicinity of the wall, the gradient of the variables demands a fine mesh because it is relatively high compared with the gradient at the capillary centre. Hereby, the element size decreases towards the capillary surface with a maximum element ratio of 25 to capture the deposited layer at a good resolution since accurate information near the capillary surface is important. The mesh in a cross-section of the capillary is shown in Fig. 3.9.

- The third capillary configuration is uneven particles deposited in the capillary. In this investigated case, the deposited particles form a layer on

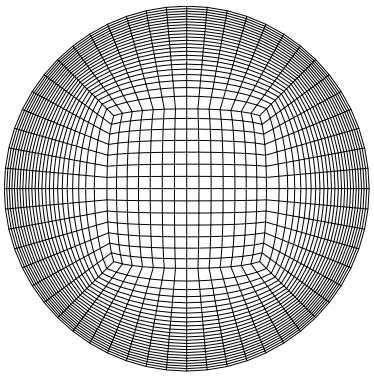

Figure 3.9: A cross-section of the capillary membrane showing the mesh in the computational domain and near the capillary surface in the radial direction.

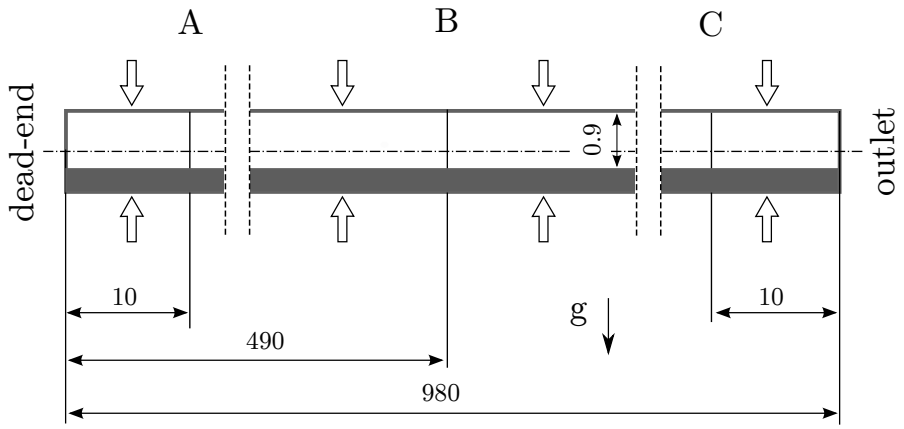

Figure 3.10: Uneven particle distribution inside the capillary membrane. The initial packing density of the deposited particles is 0.5 and the height is 0.5 mm .

the lower section of the capillary with a height of 500 μm and packing density of 0.5, as illustrated in Fig. 3.10. Thus, the considered distribution provides non-equal membrane permeability and therefore, particle removal differs from that of even particle deposition. However, with the assumption that particles are detached from the surface at the beginning of the simulation, the flow rate is not influenced by the deposited layer and is considered constant. The mesh for this case is the same than for case 2 (see Fig. 3.9). This is a theoretical particle distribution. Nevertheless, it may appear in a segment of the capillary in the form of a fouling layer. The results should provide a prognosis of the particle

distribution at which the backwash achieves high effectiveness in terms of the remaining particles in the capillary. Comparison of the removal of particles for even and uneven particle distribution is carried out.

In all the previous cases, the convergence criterion for each variable is set to 10^{-5}. A Courant number below 0.8 assures a stable calculation run and specifies an appropriate time step of 10^{-5} s for the defined mesh, according to Eq. 3.27. A Gaussian linear scheme is implied for the approximation and interpolation. A first order, bounded and implicit time discretisation scheme is specified for the solution.

Boundary conditions for two-phase flow simulations

Various boundary conditions are implemented in numerical simulations in order to specify the effects of operating conditions on the performance of the backwash process and to improve membrane cleaning efficiency. Therefore, the investigation of above mentioned capillary configurations concerns the influence of the size and density of the particle in the dispersed phase and the flux of water on particle behaviour and distribution. Furthermore, the particle motion is observed during different backwash velocity profiles. Because the backwash process interacts with different kinds of particles in terms of size and density, the numerical simulations cover a wide range of particle properties. Moreover, the behaviour of the particles is characterised for various operating pressures and at different time functions. These pressure profiles are illustrated in Fig. 3.11. These pressure profiles allow the same amount of water to flow through the capillary during 5 s of backwashing.

- P1(t): Apply constant pressure of 3 *bar* for 2 s then decrease it slowly within 2 s to reach 1 *bar* and after that keep it constant for 1 s.
- P2(t): Increase the operating pressure from zero to 3 *bar* within 1 s and keep the pressure constant for a certain time (2.5 s) then decrease it fast to reach 1 *bar* and continue backwashing the capillary for 1 s.
- P3(t): Increase the operating pressure slowly from 1 *bar* at the beginning

to 3 *bar* within 2 *s*. Keep the pressure constant for 1 *s* and then decrease it slowly to the initial value within 2 *s*.

These pressure profiles are applicable in the experiments and used for backwashing the capillary.

It is considered that the capillary has the following patches: inlet (capillary wall), outlet and wall (dead-end). At the inlet, uniform flow velocity is perpendicular to the capillary wall and has a constant value along the capillary length, as illustrated in Figs. 3.7, 3.8 and 3.10 where the patches are also shown. Converting the operating pressure to an appropriate inlet velocity enables the operation of the backwash process on the basis of inlet velocity instead of pressure. The velocity at the inlet varies according to the operating pressure. The corresponding velocity for each operating pressure is calculated by simulating a single-phase flow in the capillary with a porous wall. This relation is obtained in the next chapter. The outlet pressure concerns atmospheric pressure for water as well as for the particles. In addition, the wall is defined as no-slip patch for both water and particles, so the relative velocity between the phases and the wall is zero. The simulations were run for transient and laminar flow. The particles considered in this section are mono-disperse non-deformable spherical and smooth particles with a constant diameter.

Boundary conditions for multiphase flow simulations

Describing the evolution of potential accumulation areas inside the capillary is achieved by considering polydisperse particles. The filtered particles have different origins and may vary in diameter size and density. Therefore, the simulation model is developed to consider the polydisperse multiphase flow of the backwash process, [102, 113]. In this section, the motion of the polydisperse particles is captured by solving the multiphase flow with and without the effect of coupling with Population balance equation.

The computational domain considered in Fig. 3.7 is accepted here, since the number of control volumes is tested for mesh independent solution. For

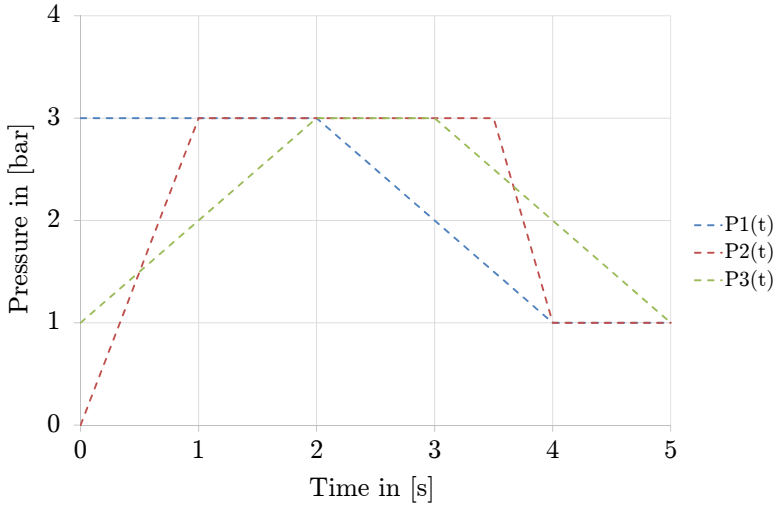

Figure 3.11: Different operating pressure profiles.

multiphase flow, the particle behaviour is simulated at an operating pressure of 2 *bar* and with a homogeneous initial particles distribution. The initial volume fraction of the involved particles is 0.1. The particles are divided into the three phases 1, 2 and 3. For case I, the particles do not agglomerate or breakup, although they have different diameters. The particle diameter and the initial volume fraction are explained in Table 3.2.

Table 3.2: Particle properties and volume fraction for polydispersed flow without consideration of agglomeration and breakage, case I.

dispersed phase	density kg/m^3	particle diameter μm	volume fraction
phase 1	1050	7	0.0334
phase 2	1050	12	0.0333
phase 3	1050	17	0.0333

For case II, the particles interact among themselves and due to their collision can aggregate and build agglomerates or break up and create smaller particles, see Table 3.3. Thus, the simulation model includes the effect of the agglomeration and breakage in order to observe the possible formation of plugs which may cause capillary clogging. Here, the case is referred to as case II, as detailed in Table 3.2. In both cases, the particles have same density. In these

calculations, the volume fraction of particles in the capillary is constant while the particles interact with each other and with the continuous phase.

Table 3.3: Particle properties and volume fraction for polydispersed flow with consideration of agglomeration and breakage, case II.

dispersed phase	density kg/m^3	particle diameter μm	volume fraction
phase 1	1050	7	0.040
phase 2	1050	12	0.056
phase 3	1050	17	0.004

The simulation is performed with an adaptive time step and transient state. The maximum Courant number in the domain is kept below 0.4 which corresponds to maximum time step of $10^{-5}\,s$.

Chapter 4

Results and Discussion

4.1 Validation of steady state flow simulation model

The flow through the porous wall and inside the capillary membrane operated in dead-end mode was simulated. The operating parameters for the numerical simulation match those used in the experiment in terms of applied pressure and capillary permeability. The range of boundary conditions applied in this numerical simulation is explained in Table 3.1. This range is adapted for experiments commonly used for the UF in dead-end capillary membrane. The validation of the results is realised by comparing the flux at the outlet for the experimentally measured and simulated values. Fig. 4.1 shows a high level of agreement between the simulation and the experiment with very small deviations due to the accuracy of the measurements.

4.2 Flow in porous walls

Both the simulation and the experiment show that the flow rate is directly proportional to the applied pressure. An increase in the outer pressure on the capillary is accompanied by an increase in the water flow rate at the outlet.
Fig. 4.2 shows the axial and radial velocity profiles at laminar flow condition along different control lines placed at different distances from the capillary axis

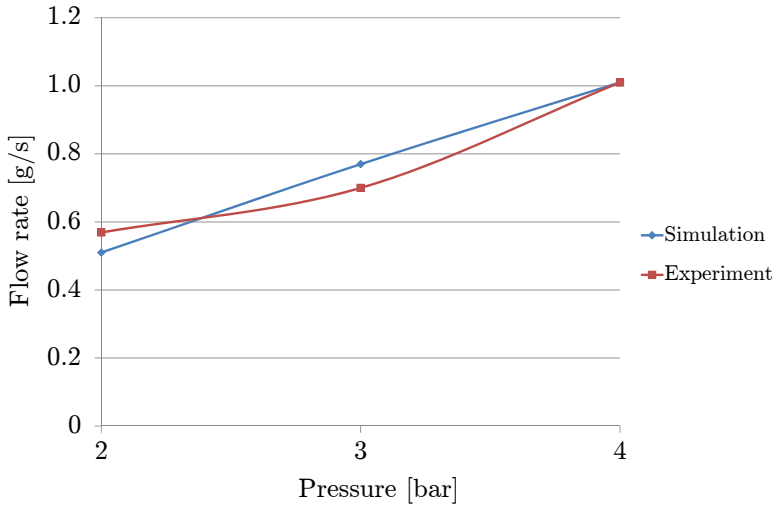

Figure 4.1: Validation of flow rate.

when an operating pressure of 2 *bar* is applied. These control lines are illustrated in Fig. 3.3. The dimensionless variable L^* denotes the normalised length of the capillary which begins at zero at the dead-end and ends at one at the outlet. Regarding the flow rate balance, the axial velocity increases from zero at the dead-end towards the outlet, where the maximum value is reached. The axial velocity increases over the capillary length towards the outlet. The maximum axial component of the velocity is observed exactly on the capillary axis at the patch outlet. For the flow at a distance of $r = 0.7\ mm$, which is at the interface between the porous wall and the inner capillary surface and along the capillary, the axial velocity is very low, and at $r = 1\ mm$ (in the porous wall) refers to negligible tangential variation in the flow. However, the radial velocity component at the interface and in the porous wall has a constant value along the capillary length. It can be supposed that the velocity in the porous wall is composed only of a radial component whereas inside the capillary the dominant component is the axial velocity.

The pressure distribution along the three control lines A, B and C across the capillary is shown in Fig. 4.3. Here, the $r*$ is in the abscissa which denotes the normalised radius of the capillary where zero is on the axis. The dimensionless form simplifies the presentation of the results independent of the scale. Over the

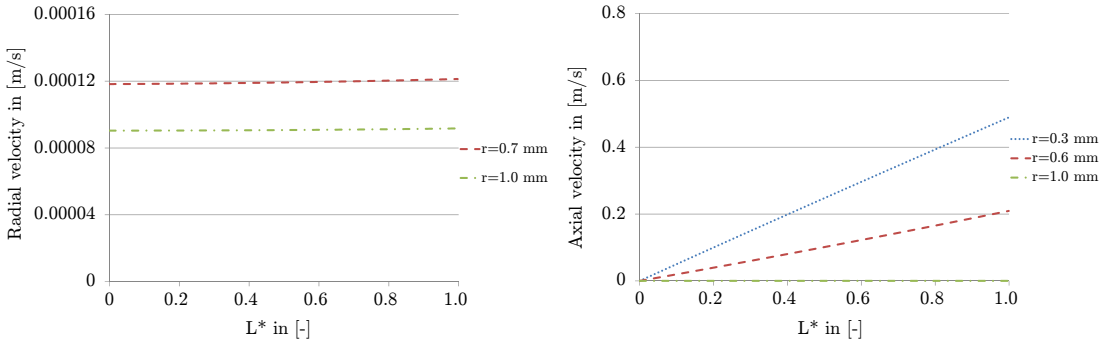

Figure 4.2: Axial and radial velocity profiles at different control lines along the capillary at 2 *bar* operating pressure.

cross-section, the porous wall absorbs the high operating pressure, which reaches a relatively low and constant value in the inner capillary.

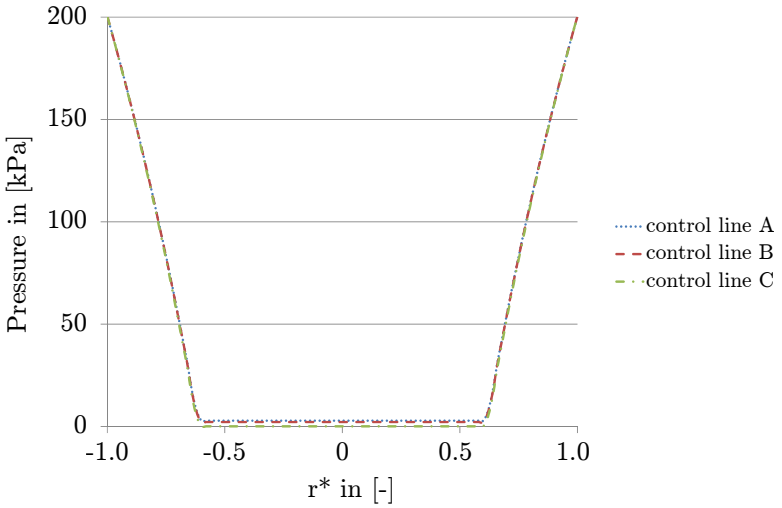

Figure 4.3: Pressure across the capillary at three control lines A, B and C at 2 *bar* operating pressure.

4.2.1 Effect of operating pressure

Because the pressure gradient is the driving force for the backwash process, determining the pressure drop inside the capillary during different operating conditions is of increasing interest. The numerical results show that the

pressure changes along the capillary length for various operating pressures. As it is expected, the pressure inside the capillary increases when the applied pressure increases. The flow rate reduces towards the dead-end, thus increasing the pressure inside the capillary. The pressure starts with a value of zero at the outlet and increases to its maximum at the dead-end. Increasing the operating pressure improves the removal of suspended particles because as the pressure gradient inside the capillary increases it has consequences on the axial velocity Fig. 4.4. The radial velocity profile has a constant value over the capillary

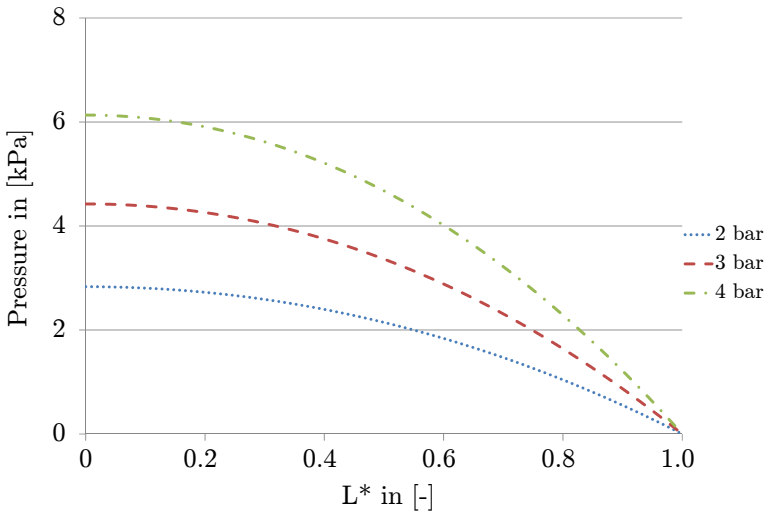

Figure 4.4: Pressure at the capillary axis for different operating pressure and permeability of 160 $L/(m^2\ h\ bar)$.

length independent of the operating pressure. In Fig. 4.5, the radial velocity is plotted against the capillary length at the interface between the porous wall and inner capillary surface $r = 0.7\ mm$ for different operating pressures. The profile variation from the dead-end to the outlet is very small and the velocity is considered as constant. This assumption of uniform normal-wall velocity is found to be a reasonable approach and is applicable for further multiphase simulation when the permeable wall is neglected. The radial velocity at inlet for a non-porous capillary membrane is based on the results obtained from Fig. 4.5 and summarised in Table 4.1.

For axial velocity, increasing the pressure gradient leads to significant changes in the driving force which controls flow rate and axial velocity, as referred in

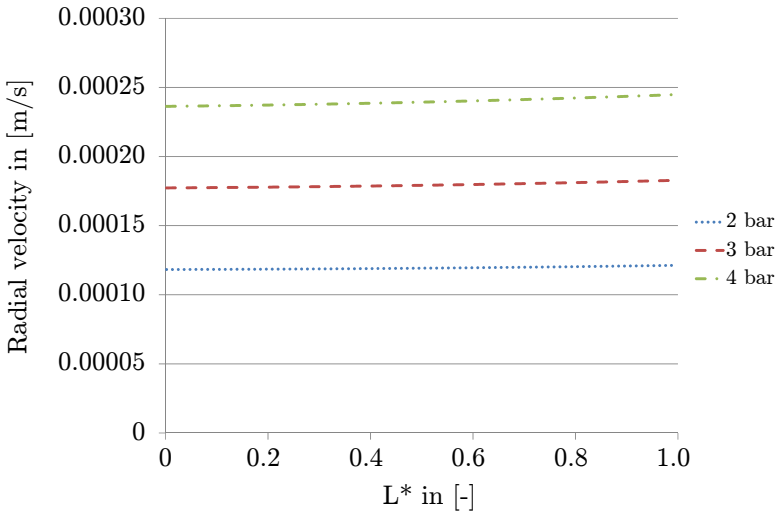

Figure 4.5: Radial velocity at the interface between porous wall and inner capillary surface $r = 0.7\ mm$ for different operating pressures and permeability of 160 $L/(m^2\ h\ bar)$

Table 4.1: Radial velocity at inlet and average axial velocity at outlet for different operating pressure and permeability of 160 $L/(m^2\ h\ bar)$.

Operating pressure *bar*	Radial velocity at inlet m/s	Average axial velocity at outlet m/s
1	$3.60\ 10^{-5}$	0.14
2	$7.18\ 10^{-5}$	0.27
3	$1.07\ 10^{-4}$	0.40
4	$1.43\ 10^{-4}$	0.52

Fig. 4.6. The fluid accelerates towards the outlet, giving different maximum velocities and subsequently different Reynolds numbers. The Reynolds number recorded for the axial velocity in the capillary at the outlet is calculated in Table 4.2 for different operating pressures.

Fig. 4.7 illustrates the relation between the drop inside the capillary for different values of the flux. In is clear that if the flux increases, the pressure drop increases.

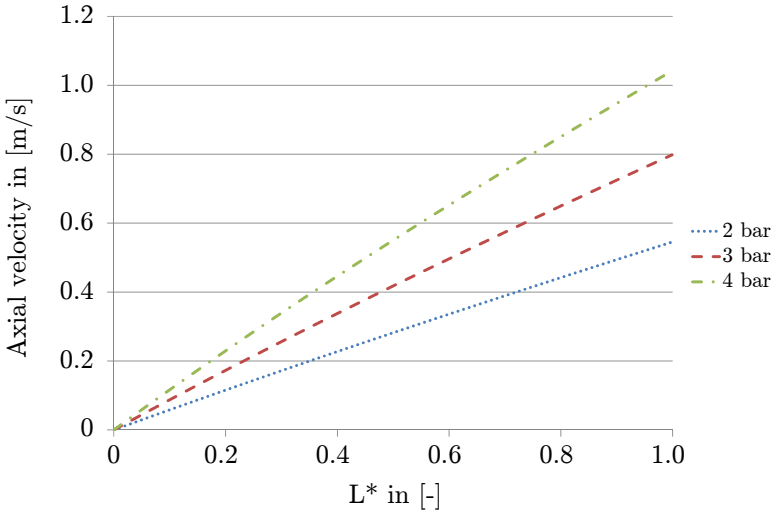

Figure 4.6: Axial velocity at the capillary axis for different operating pressures and permeability of 160 $L/(m^2\ h\ bar)$

Table 4.2: Reynolds number and flow rate at different operating pressures and permeability of 160 $L/(m^2\ h\ bar)$.

Operating pressure bar	Flow rate m^3/s	Reynolds no.	Flux $L/(m^2\ h)$
1	$2.55\ 10^{-7}$	196	130
2	$5.05\ 10^{-7}$	381	257
3	$7.55\ 10^{-7}$	560	384
4	$1.01\ 10^{-6}$	729	514

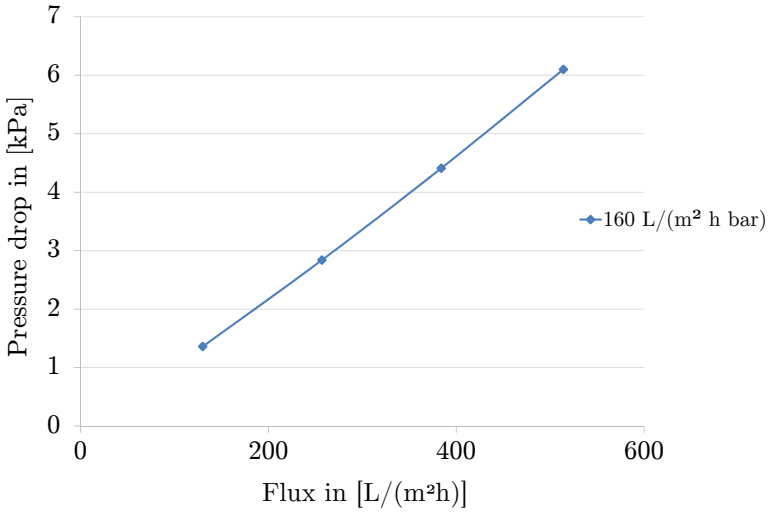

Figure 4.7: Variation of pressure drop inside the capillary as a function of the flux for membrane permeability of 160 $L/(m^2\ h\ bar)$.

4.2.2 Effect of membrane permeability

The fouling layer decreases membrane permeability and forms additional resistance for the water flow through the capillary. The total membrane resistance results from the sum of all resistance involved in series models, namely membrane resistance, irreversible fouling resistance and cake layer resistance. Therefore, the thickness of the fouling layer has a significant influence on the pressure drop inside the capillary and on backwashing flux. In this thesis, variation in membrane permeability due to the formation of a fouling layer is taken into account.

Table 4.3 summarises the flow rate resulting from various membrane permeability values at constant operating pressure. The linear relation between flux and permeability is observed with small deviation caused by numerical errors. The flow rate through the porous wall increases with the destruction of the fouling layer, which changes resistance towards allowing more water to enter the capillary membrane. Thus, increasing the permeability increases significantly the flow rate through the membrane when keeping the operating pressure constant. Fig. 4.8 presents the relationship between the fouling layer

Table 4.3: Reynolds number and flow rate at different permeabilities and 2 *bar* operating pressure

Permeability $L/(m^2\ h\ bar)$	Flow rate m^3/s	Reynolds no.	Flux $L/(m^2\ h)$
80	$2.53\ 10^{-7}$	191	128
160	$5.05\ 10^{-7}$	381	257
400	$1.24\ 10^{-6}$	950	630

and the pressure inside the capillary. The pressure and the related driving force are higher when membrane permeability declines for a constant operating pressure. It is assumed that the formation of the fouling layer is a modification of membrane permeability. Thus, the removal of the deposited particles increases the pressure since it enhances membrane permeability. Based on the driving force inside the capillary, the estimated axial velocity at the capillary axis shows a proportional relationship to membrane permeability (Fig. 4.9). The greater the membrane permeability, the higher the axial velocity caused by

the higher pressure gradient.

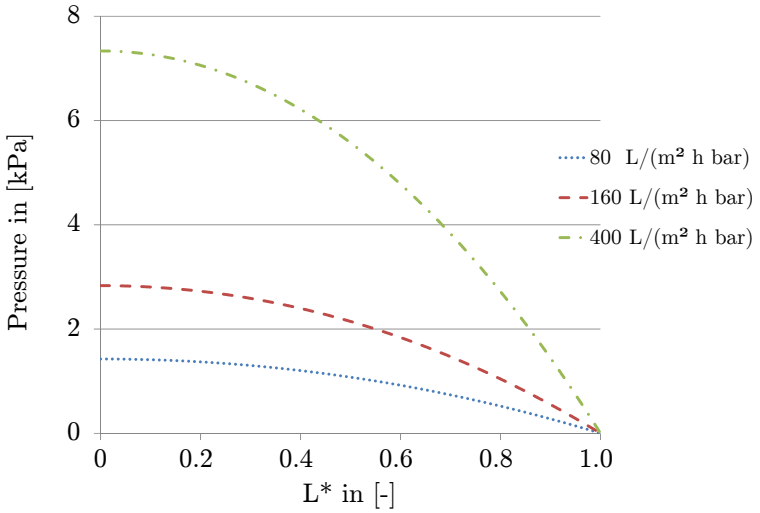

Figure 4.8: Pressure at the capillary axis for different membrane permeabilities and 2 *bar* operating pressure.

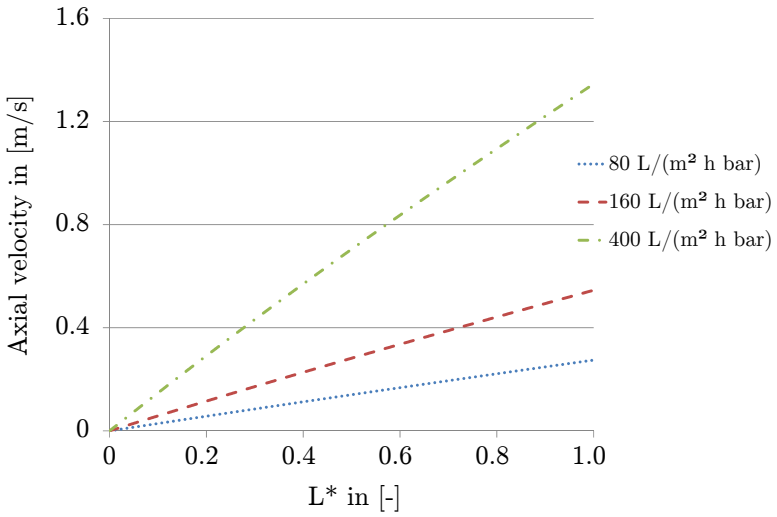

Figure 4.9: Axial velocity at the capillary axis for different membrane permeabilities and 2 *bar* operating pressure.

For high permeability, the flow can pass easily through the porous wall and the radial velocity increases. However, the profile remains constant over the

capillary length apart from the permeability value (Fig. 4.10). These small changes in radial velocity from the dead-end to the outlet have no considerable influence on the flow entering the capillary. Thus, again the assumption of a normal-wall velocity is an acceptable approach and can be used for further simulation without consideration of the flow in the porous wall.

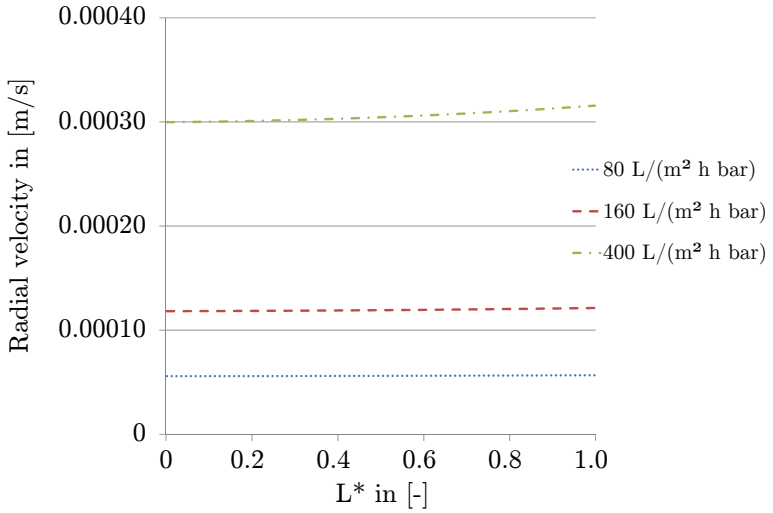

Figure 4.10: Radial velocity at the interface between the porous wall and inner capillary surface for different membrane permeabilities and 2 *bar* operating pressure.

4.3 Tightly adhered particles

The formation of cake layers plays a crucial role in the velocity distribution inside the capillary during the backwash process, and thus on the shear stress near the capillary surface. The tightly impermeable deposit layer on the membrane surface is denoted in the evaluation as bulges. Thus, in order to cover a wide range of uneven particle deposit configurations, different bulge lengths, positions and depths inside the non-porous capillary membrane are investigated. These configurations are explained in Fig. 3.5. All the simulations are carried out for flux resulting from operating pressures, 2 *bar* and 3 *bar* and permeability of 160 $L/(m^2\ h\ bar)$.

Velocity distribution

Evaluating the velocity distribution inside the capillary is essential in order to estimate the influence of shear stress on the bulges. The velocity distribution depends on the capillary section as the velocity accelerates towards the outlet. However, in all sections and due to the boundary conditions (no-slip) in the interface bulges and fluid, velocity is zero.

In the first section I next to the dead-end which picked up three bulges, the maximum velocity observed is in the centerline of the third bulge, as shown in Fig. 4.11. It reaches at $L^* = 0.07$ velocity of 0.04 m/s and 0.07 m/s for operating pressures of 2 bar and 3 bar, respectively. The flow velocity is heavily dependent on the shape and depth of the bulges.

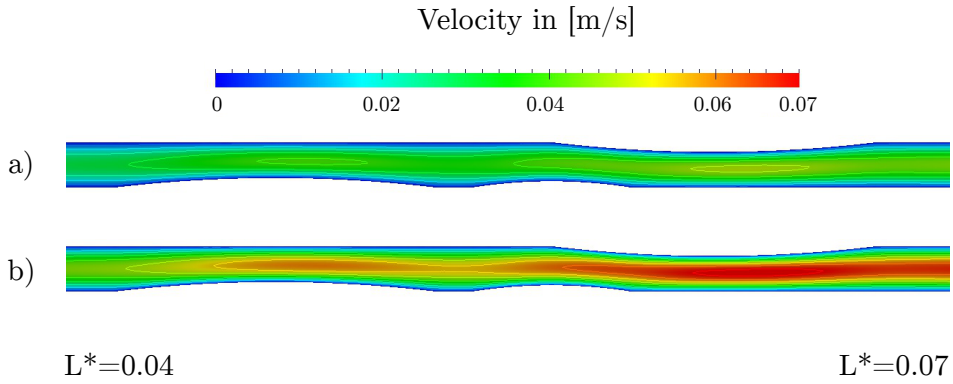

Figure 4.11: Velocity distribution at different bulge (cake layer) thicknesses in the vicinity of the dead-end (section I) for two operating pressures, a) 2 bar and b) 3 bar.

In the second section II, the velocity increases rapidly, especially in the narrowing between two bulges. The velocity observed at this position is 0.35 m/s for 2 bar operating pressure and 0.45 m/s for 3 bar. After the fluid passes through the narrowing, the velocity decreases to 0.25 m/s and to 0.28 m/s, as shown in Fig. 4.12.

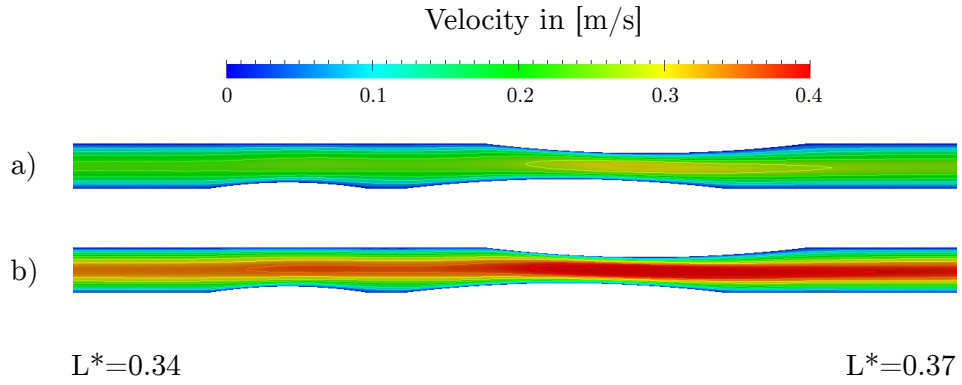

Figure 4.12: Velocity distribution at different bulge (cake layer) thicknesses in section II and arrangements for two operating pressures, a) 2 *bar* and b) 3 *bar*.

In section III, it is assumed that the impermeable layers grew simultaneously and next to each other during the filtration process. The velocity varies between zero at the bulges where no-slip boundary condition is adjusted and the highest value is observed directly in the narrowing. The velocity in the bulges region reaches 0.4 m/s and 0.6 m/s for operating pressure 2 *bar* and 3 *bar*, respectively, as illustrated in Fig. 4.13.

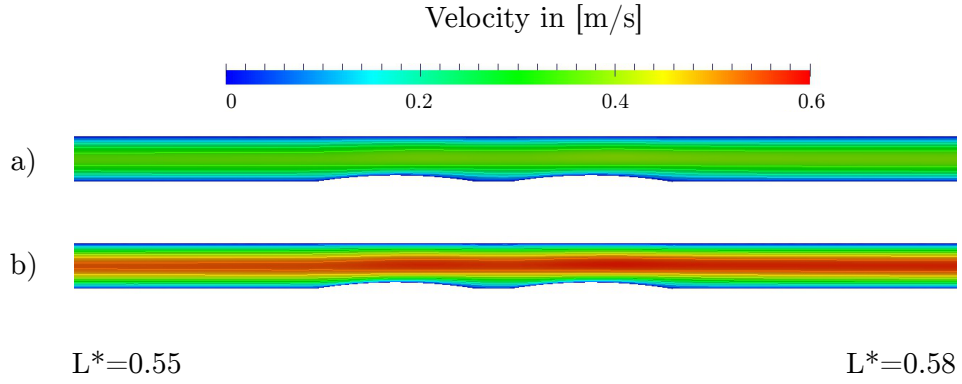

Figure 4.13: Velocity distribution at different bulge (cake layer) thicknesses in section III and arrangements for two operating pressures, a) 2 *bar* and b) 3 *bar*.

In section IV, the impermeable layers have grown opposite to each other, causing the capillary to straighten. The same tendencies are recorded here, i.e. high fluid velocity in the narrowing. As the flow rate is constant, the velocity at this narrowing increases and achieves its maximum value. This value depends

on the distance between the two bulges. When the distance is about 40% of the capillary diameter, the simulation shows a higher velocity in the narrowing than that at the outlet. The velocity at the outlet is 0.48 m/s for 2 bar operating pressure and 0.6 m/s in the narrowing, whereas the velocity for 3 bar operating pressure is 0.7 m/s at the outlet and 0.8 m/s in the narrowing, see Fig. 4.14. However, at the capillary wall, the velocity is at its minimum and adjusted to the inlet velocity given in Table 4.1.

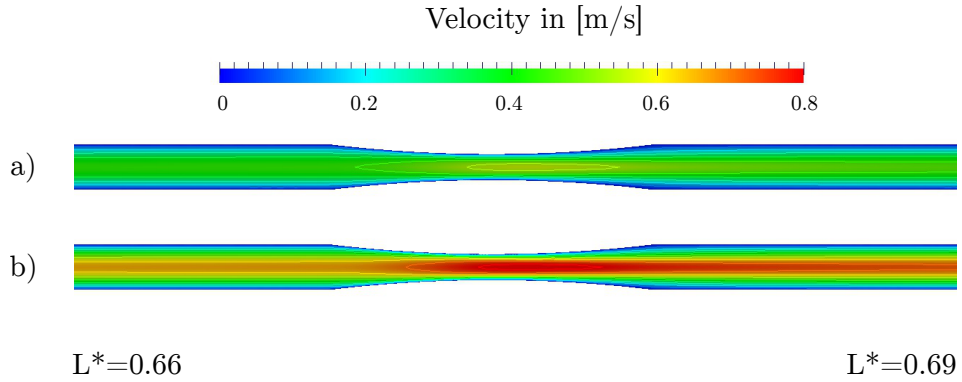

Figure 4.14: Velocity distribution at different bulge (cake layer) thicknesses in section IV and arrangements close to the outlet for two operating pressures, a) 2 bar and b) 3 bar.

Shear stress

Increasing the shear stress during backwashing improves removal of the cake layer. The flow over the membrane surface induces shear stress which disrupts the detachment of the particles. Thus, the investigation of shear stress inside the capillary membrane has a significant influence on understanding the detachment mechanism of the adhered particles. The shear stress value is determined by the velocity gradient, as calculated in Eq. 3.3. However, velocity varies in the capillary according to bulge position and arrangement, which also causes different shear stress values.

Considering a clean capillary before the formation of the cake layer and during the backwash flow, the evaluation of shear stress on the membrane surface

where the velocity is at its maximum value varies between 0 at the dead-end and 3 Pa and 5 Pa at the outlet for 2 bar and 3 bar, respectively, as shown in Table 4.2. However, these values change with the evolution of cake layers as they straighten the capillary diameter and the velocity changes accordingly. The exponential increase in velocity from zero at the bulges (no-slip boundary condition) with the distance towards the capillary centre induces a higher shear stress at the surface of the bulges than in the flow. As mentioned above, the inlet velocity for the non-porous capillary is explained in Table 4.1.

The shear stress in the first section I ranges from 0 Pa at the dead-end to 0.2 Pa for 2 bar operating pressure and 0.3 Pa for 3 bar, as shown in Fig. 4.15. The highest shear stress is observed on the surface of the second and third bulges surface where the velocity gradient is higher due to the narrowing of the capillary. Hence, sweeping away the tightly deposited particles in this section using the backwash flow becomes difficult due to low shear stress and, therefore, an effective backwash process in terms of flushing out the tightly deposited particles is accordingly difficult.

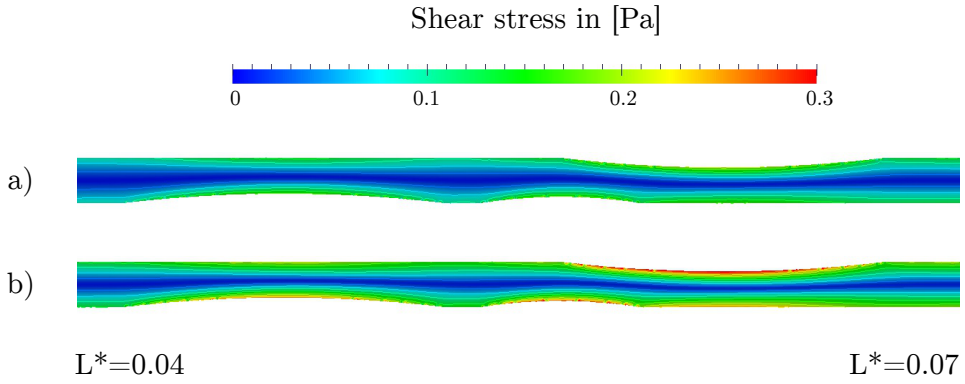

Figure 4.15: Shear stress at different bulge (cake layer) thicknesses in the vicinity of the dead-end (section I) for two operating pressures, a) 2 bar and b) 3 bar.

In section II and as demonstrated in Fig. 4.16, higher shear stress is observed. The maximum value is 2 Pa for 2 bar operating pressure and 3 Pa for 3 bar. Increasing the operating pressure leads to higher shear stress. This relatively high shear stress has a better impact on the tightly deposited particles and can

cause the transfer of these particles from the membrane surface to the bulk flow.

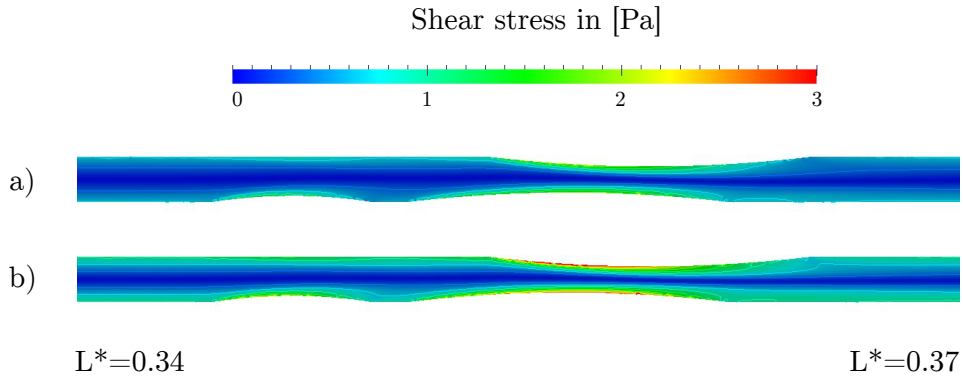

Figure 4.16: Shear stress at different bulge (cake layer) thicknesses in section II and arrangements for two operating pressures, a) 2 *bar* and b) 3 *bar*.

In section III, Fig. 4.17, the simulations show the shear stress on two bulges located next to each other, which have the same depth in the capillary. The values for shear stress calculated on the bulges' surface barely differ. The maximum shear stress value in this section is on the bulge surface for both operating pressure: 2 *Pa* for 2 *bar* and 3 *Pa* for 3 *bar*.

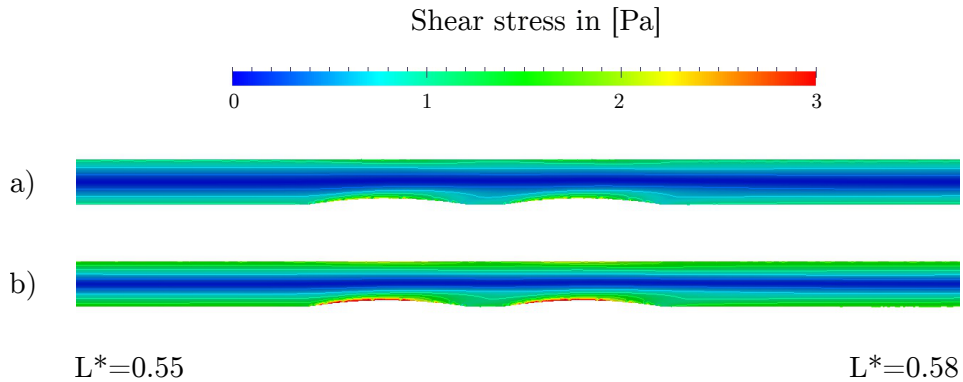

Figure 4.17: Shear stress at different bulge (cake layer) thicknesses in section III and arrangements for two operating pressures, a) 2 *bar* and b) 3 *bar*.

Fig. 4.18 shows the shear stress on two bulges opposite to each other. The shear stress values obtained on the bulges' surface, 4 *Pa* and 5 *Pa* for operating

pressure 2 *bar* and 3 *bar*, respectively, are the highest in the considered capillary. The probability of detachment occurring for tightly deposited particles is elevated in the direction of the capillary outlet where shear stress increases due to the increase in flow rate.

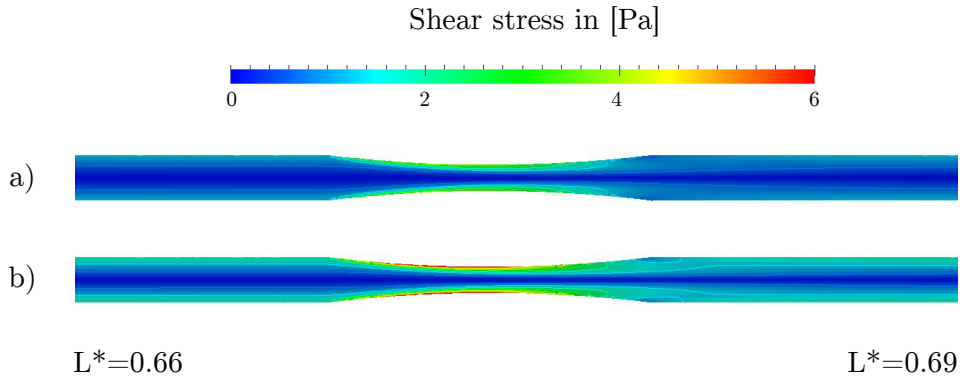

Figure 4.18: Shear stress at different bulge (cake layer) thicknesses in section IV and arrangements close to the outlet for two operating pressures, a) 2 *bar* and b) 3 *bar*.

4.4 Conclusion for single phase flow

The flow of the water inside the capillary during the backwash process is simulated. These simulations are carried out under realistic and applicable boundary conditions to the backwash process of capillary membrane. The pressure drop inside the capillary as well as flux for different operating pressure is estimated. It is observed that, the variation of the radial velocity along the capillary length is small and can be neglected for further simulations which consider the motion of the particles. This can be ascribed to the small variation of the pressure inside the capillary compared to the applied pressure. Moreover, the flux and velocity profile for different membrane permeability is obtained. This change in permeability represents either membrane permeability or the formation of a fouling layer. This is a reasonable approximation as the fouling layer has a porous structure. The developed model shows a good agreement in terms of water flow rate with the experiments performed on a single capillary.

Furthermore, a possible deformation of the capillary structure or impermeable sectors of the capillary are taken into account. The simulation model contains bulges distributed randomly on the inner capillary surface at the dead-end vicinity, in the middle and near the outlet of the capillary. In practical situations in the capillary, impermeable sections are the result of pore blocking or the formation of an extremely dense cake layer. For these bulges, the numerical model predicts the velocity profile in the narrowing and the shear stress induced on the bulges in the capillary. These values can change according to the position of the bulges, their form and depth in the capillary. However, this model can differ from reality if the bulges reveal a flow through them. In this case, the bulges undergo less shear stress as the velocity gradient decreases over them. The simulation results show high shear stress is induced on the bulges compared to that on the membrane surface in the bulges' vicinity. This high shear stress increases the probability of removing the impermeable cake layer.

In the horizontal capillary, the height difference is quite small and thus gravity has a negligible effect. Therefore, for further simulations, the inward flow is composed of a radial velocity component with a constant magnitude over the capillary length.

4.5 Homogeneous particle distribution

A transient simulation of the backwash process is carried out in a capillary membrane operated in dead-end mode. The behaviour and the distribution of the particles is investigated under different operating conditions. The evaluation of the results in this study is performed in terms of particle volume fraction in the control volume. The simulation results are evaluated by inserting control lines A, B and C inside the capillary at a distance of 10 mm from the dead-end, in the middle and at 10 mm from the outlet across the capillary, respectively, as shown in Fig. 3.7.
The operating pressure is transferred to backwash flux over the capillary length, as presented in Table 4.1. The velocity profile entering the capillary is defined based on the results obtained for the capillary with porous wall. Thus, the effects of the porous wall are implicitly taken into account by adjusting the appropriate boundary conditions. The latex particles properties in terms of density (1050 kg/m^3), shape and size are used for the dispersed phase.
A number of numerical simulations have been carried out to analyse the distribution of the particles, taking into account the influence of the backwash flux, particle size and density on the particle behaviour. The main focus is on the removal of the particles and their distribution in the capillary, in addition to the fluid velocity pattern. To estimate what portion of particles remains in the capillary during the backwash process, it is assumed that the initial fraction of particles inside the capillary is 100 %. Due to particle removal, this fraction decreases over the course of backwashing. The capillary is thus clean when this value approaches zero.
The evaluation of the particle behaviour is expressed by the local volume fraction which represents the volume fraction at a specific position in the capillary. This value is set to 0.1 as the initial value for the whole capillary.

As study case, a backwash process with an operating pressure of 2 bar is considered. The particles are latex with a constant size of 10 μm (mono-disperse) and initially have a homogeneous distribution in the capillary. The schematic of the capillary is illustrated in Fig. 3.7.

Stokes number

Calculations for Stokes number according to the relation given in Eq. 3.24 are shown in Table 4.4. All velocity values are calculated for single phase flow. Furthermore, because flow velocity is not constant over the capillary length, the maximum velocity estimated at the outlet is used for the calculation. The computed Stokes number refers to particles following the flow and thus, the particles which are tightly coupled to the fluid have a similar velocity to it.

Table 4.4: Stokes number calculated at different operating pressures.

Operating pressure bar	Average axial velocity at outlet m/s	Stokes no.
1	0.14	0.0006
2	0.27	0.0012
3	0.40	0.0017
4	0.52	0.0022

Velocity profile

Observing the axial velocity profile of the fluid during the simulation shows that the parabolic velocity profile is almost reached in cross-sections B and C of the capillary. Fig. 4.19 shows the fluid velocity achieved in the investigated case over time and at control lines A, B and C. The axial velocity increases towards the outlet due to the fluid injection along the capillary. It tends to be symmetrical to the capillary axis. The tendency to symmetrical velocity is attributed to the negligible gravitational effects compared with drag effects.
In the vicinity of the dead-end (control line A), the fluid velocity profile shows symmetric distribution with a maximum value of 0.0055 m/s when the particle concentration is also symmetrical to the capillary axis. After 5 s, the maximum velocity of the fluid is found above the zones where a high volume fraction of particles exists, with a value of 0.007 m/s. The upward shifting of the parabolic velocity profile can be attributed to particle enrichment area in the lower half, where the flow resistance increases. In the middle of the capillary (control line B), the maximum axial velocity is 0.257 m/s and a parabolic profile is observed. At the outlet (control line C), the maximum axial velocity reaches 0.57 m/s.

A)

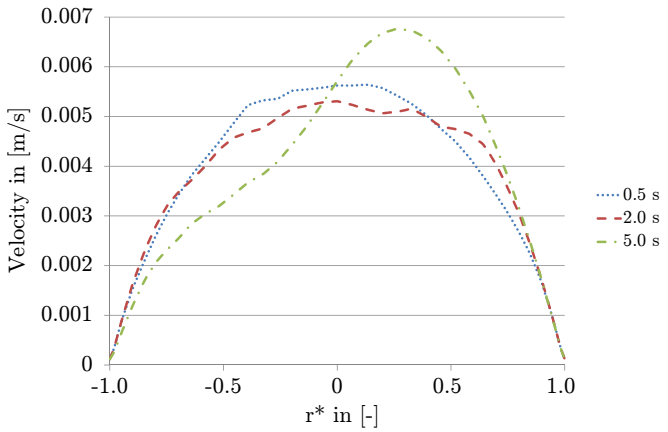

B)

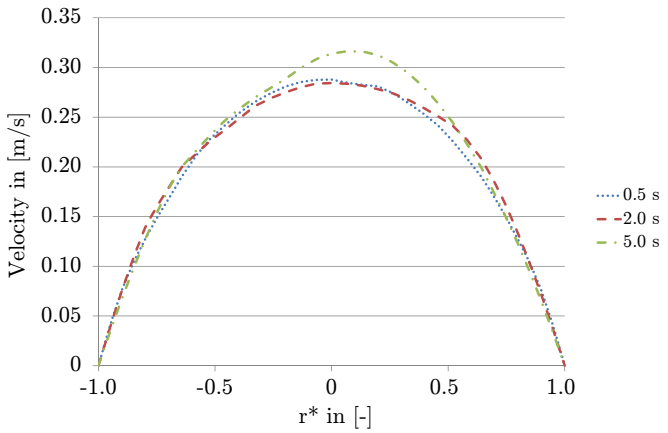

C)

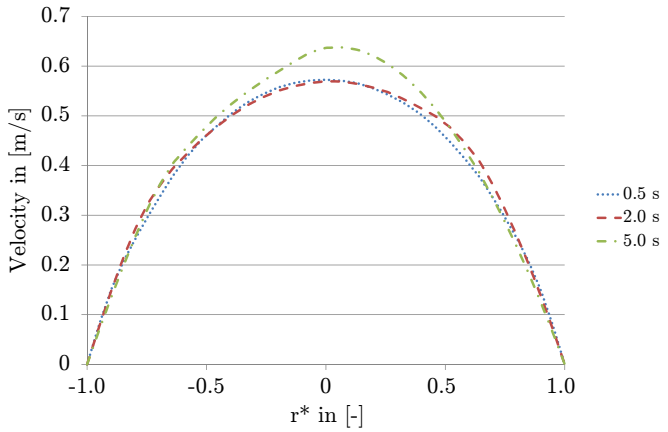

Figure 4.19: Velocity profile at control lines A, B and C for operating pressure of 2 bar and particle size of 10 μm and density of 1050 kg/m^3.

The deviation from symmetry becomes insignificant when the flow velocity increases and overcomes flow resistance caused by the accumulation of particles. The dominant velocity component during backwashing is the axial component which changes over the capillary length (see Fig. 4.19) and is responsible for the transport of the particles towards the outlet. The radial velocity has a relatively low values, but it carries the particles towards the capillary centre. With the existence of gravity, the stagnation point for the radial velocity is shifted to the lower half of the capillary, as shown in Fig. 4.20.

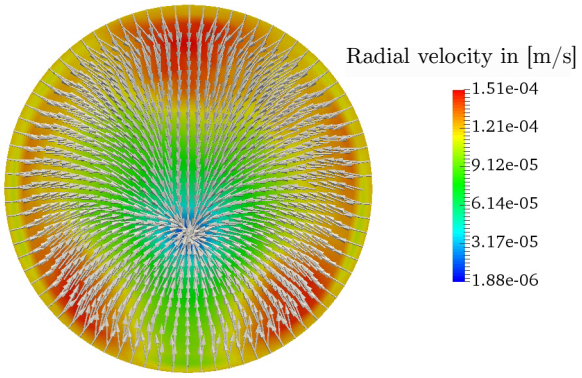

Figure 4.20: Vector plot of radial velocity in a cross-section placed at control line A at the beginning of the simulation when particle distribution is homogeneous in the capillary membrane for operating pressure of 2 bar and particle size of 10 μm and density of 1050 kg/m^3.

Over time, a secondary flow develops in the capillary due to the gravitational effect and heterogeneous distribution of the particles in cross-section (see Fig. 4.21). The homogeneous distribution of the particles at the beginning of the simulation forms uniform flow resistance against the fluid entering from the inlet patch. As the particles are transported towards the capillary centreline, and more specifically to the lower half of the capillary, due to the effect of gravity, the fluid entering the lower part of the capillary encounters a higher resistance due to the accumulation of particles. Thus, instead of penetrating the accumulated particles, the fluid flows in a circle around the mass of the particles

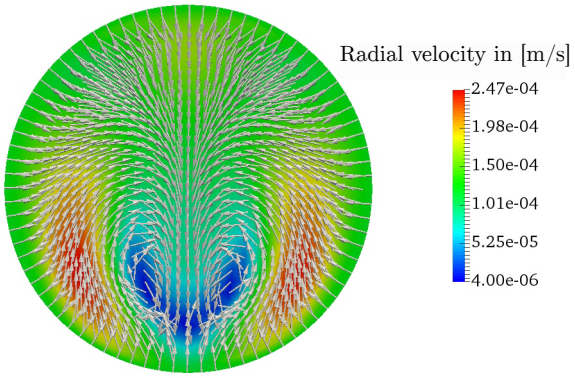

Figure 4.21: Vector plot of radial velocity in a cross-section placed at control line A for operating pressure of 2 *bar* and particle size of 10 μm and density of 1050 kg/m^3.

and meets the fluid entering the capillary from the upper part. As a result, the secondary flow is induced in two recirculation zones in the capillary cross-section, as shown in Fig. 4.21. Therefore, the secondary flow reaches its maximum value near the membrane and has an upward flow, whereas it has a downward flow in the centre of the capillary. Its strength depends on the non-homogeneous distribution of the suspended particles and the particle size, which determines the drag force effect on them. If the size of particles is small, the drag force is accordingly small and the entering flow does not encounter high resistance. Similarly, the flow exerts on large size particles with a high drag force. The secondary flow could also strongly affect the distribution of the particles in the cross-section when it appears in zones with a high concentration of particles. This secondary flow is noticeable in the vicinity of the dead-end when it is less disturbed by axial velocity. The development of the radial flow from concentric to secondary flow, at 0.5 and 5 *s*, respectively can be seen in Figs. 4.20 and 4.21 and the corresponding particle distribution at the mentioned time is shown in Fig. 4.22.

Particle distribution

The suspended particles are subject to the force of gravity and the induced hydrodynamic force. In case of size 10 [μm] particles, the lift force as well as the virtual mass has a very limited influence on the distribution of particles due to the low relative velocity between the phases, as well as the small size of the particles. The particles follow the flow and have almost the same velocity, as shown in Table 4.4. They tend to accumulate in the lower half of the capillary and far from the wall. The high concentration of particles in these zones can be attributed to the radial flow in the capillary which transports the particles towards these zones, as shown in Fig. 4.20. Furthermore, the gravity effect has a significant impact on shifting the zones of high particle concentration from the middle to the lower half of the capillary. The particle distribution in cross-section in the vicinity of the dead-end $L^* = 0.01$ over time is represented in Fig. 4.22. The simulation shows that at the beginning of the backwash process and as the fluid enters the capillary, the suspended particles are carried towards the centre of the capillary by the radial velocity of the flow. Thus, over time, parts of the capillary near the inlet become clean and the particle portion is almost equal to zero. These clean zones spread in the cross-section of the capillary and after 5 s, the particles accumulate in the lower half of the capillary, whereas the upper part of the capillary is relatively clean. The particle accumulation zone shifts away from the centre due to the transport of particles from the circumference of the capillary and the gravity effect. The zones with a high concentration of particles are functions of the backwash flux. That means the gravitational effect becomes negligible when the axial velocity increases and the convective effects in the direction of the outlet becomes more noticeable. The zones with a high particle concentration are separated from the membrane by a zone of clear fluid. The high concentration zones are situated in the lower half of the capillary.

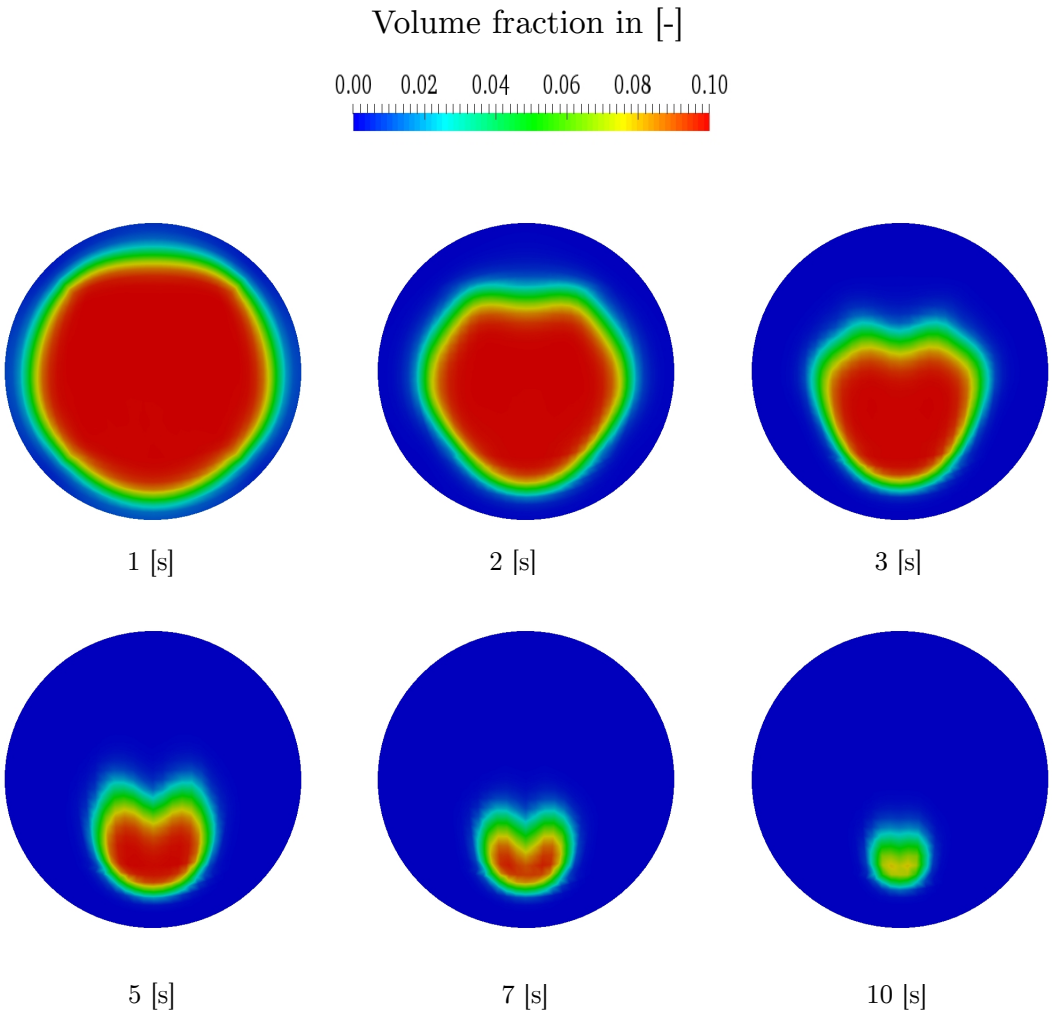

Figure 4.22: Particle distribution over cross-section at control line A for particle diameter of 10 μm and density of 1050 kg/m^3 during backwash process.

Pressure drop

Predictions regarding the pressure over the capillary axis is shown in Fig. 4.23. As expected, the maximum pressure is observed at the dead-end side and decreases towards the outlet, where it is atmospheric pressure. Furthermore, there is a pressure variation in the radial direction due to the gravity effect. However, this has a limited effect on the velocity profile. At the beginning of the backwash process the pressure is relatively high and the decrease in the volume fraction of the particles inside the capillary over time contributes to

decrease in the pressure drop. When the capillary is completely recovered the pressure becomes very similar to the values calculated in Fig. 4.4. This indicates the influence of the volume fraction of particles on the pressure drop in the capillary.

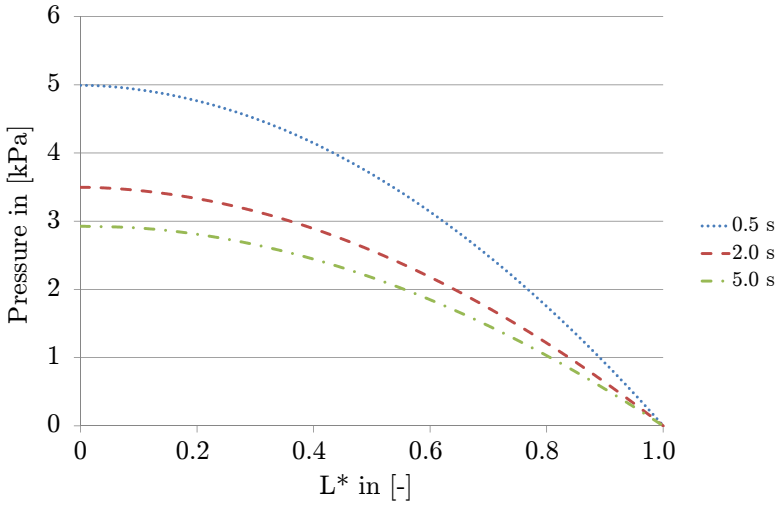

Figure 4.23: Pressure distribution over the capillary axis at operating pressure of 2 bar and particle size of 10 μm and density of 1050 kg/m^3.

4.5.1 Effect of operating pressure

In order to investigate the efficiency of the backwash process under different operating pressures, a simulation was carried out with operating pressures of 1, 2 and 3 bar and the removal of the particles from the capillary membrane at these pressures was compared. The effect of the operating pressure on the removal of the particles is presented in Fig. 4.24. It reveals that the portion of particles in the computational domain is inversely proportional to the operating pressure and resultant flux.

It can be seen that nearly 65 % of particles leave the capillary within 5 s for an operating pressure of 1 bar. The portion of the removed particles increases to 90 % after 5 s for an operating pressure of 2 bar. However, the particles are almost all flushed out of the capillary (95 %) when the operating pressure

increases to 3 *bar*.

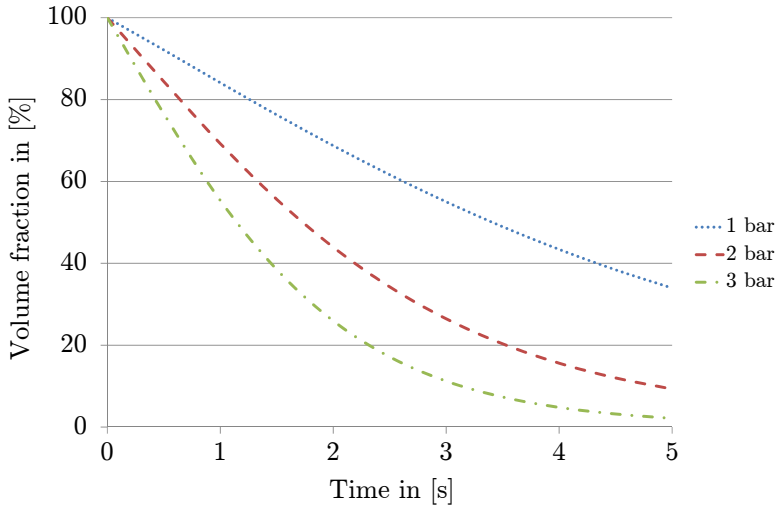

Figure 4.24: Recovery of the volume fraction of particles with diameter of 10 μm and density of 1050 kg/m^3 through different operating pressures in percent.

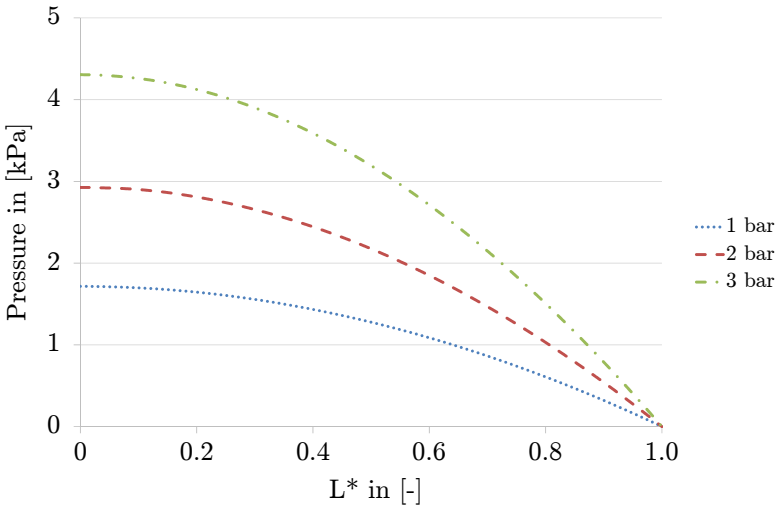

Figure 4.25: Pressure distribution inside the capillary membrane for different operating pressures after 5 *s* of simulation.

Variation of the pressure distribution over the capillary length for different operating pressures 1, 2 and 3 *bar* is shown in Fig. 4.25. It is obvious that the

lower the operating pressure, the smaller the pressure drop inside the capillary. For an operating pressure of 1 *bar*, the pressure drop after 5 *s* of simulation is 1.7 *kPa* whereas for 3 *bar* operating pressure, the pressure drop is much higher and reaches 4.3 *kPa*. The corresponding removed particle portions after 5 *s* are shown in Fig. 4.24. Increasing the operating pressure leads to higher drag force resulting from increasing the flow velocity inside the capillary. Thus, this high drag force causes a large pressure drop.

The secondary flow at the above mentioned operating pressure is shown in Fig. 4.26. The induced secondary flow reveals two recirculation zones for 1 *bar* operating pressure. However, when the operating pressure increases, the secondary flow in the capillary cross-section almost vanishes, as seen in Fig. 4.26b, and the radial flow becomes concentric with a centre in the lower half of the capillary. The accumulation of the particles does not form significant resistance against the entering fluid when the operating pressure increases to 3 *bar*. Thus, for low operating pressure (1 and 2 *bar*), the flow inside the capillary in a cross-sectional plane will create secondary flow due to the change in the particle distribution. Fig. 4.27 shows the particle distribution for the

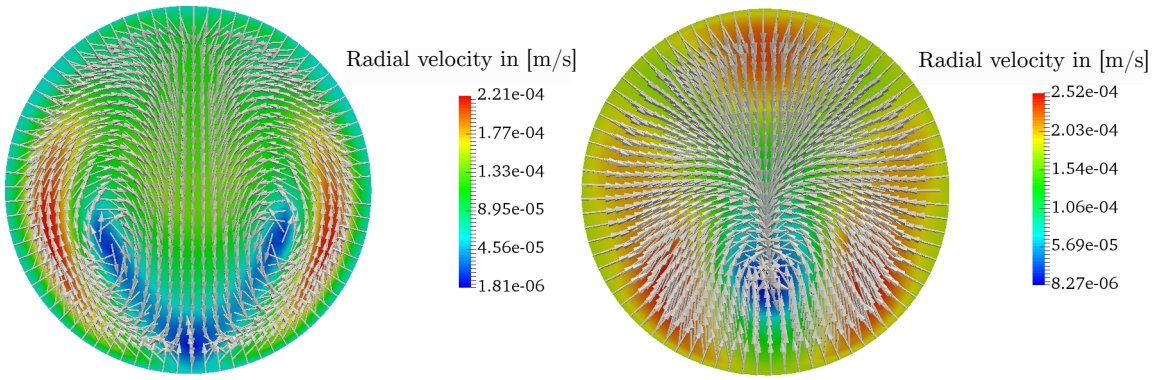

a) b)

Figure 4.26: Vector plot of secondary flow after 5 *s* of simulation for a) 1 *bar* and b) 3 *bar* operating pressure on capillary cross-section located at control line A.

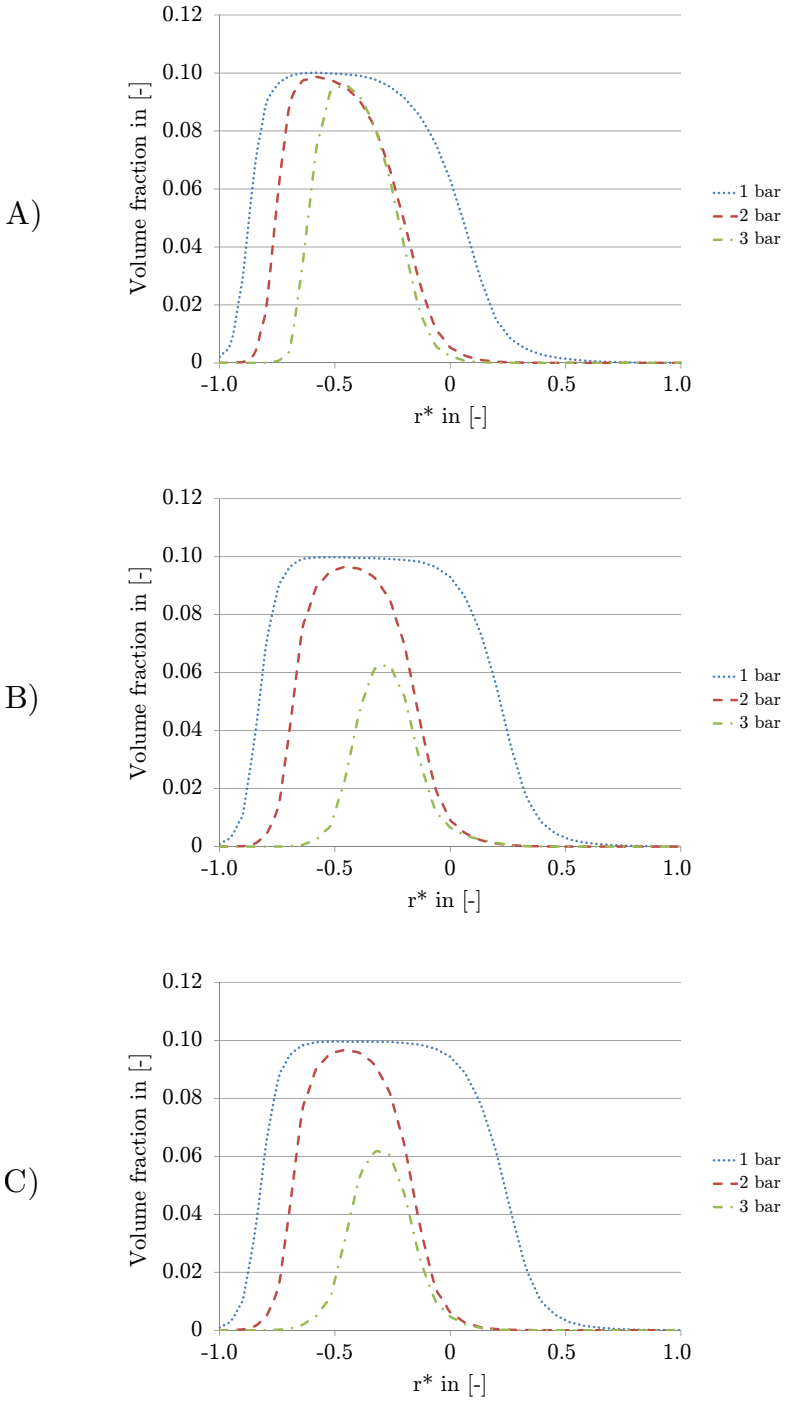

Figure 4.27: Volume fraction at control lines A, B and C for operating pressures of 1, 2 and 3 *bar* and particle size of 10 μm after 5 s of simulation.

considered operating pressure at control lines A, B and C. It is obvious that the particles accumulate in certain positions. This position is a stagnation point of the radial velocity. For low operating pressure, the particles are distributed over a wide area in the capillary cross-section. This area becomes smaller when the operating pressure increases due to the transport of particles in the radial direction. However, according to Fig. 4.24, approximately 40 % of particles remain in the capillary after 5 $[s]$ and these particles cover a broad area in a vertical plane. Comparing the fluid velocity distribution on control lines A, B and C for different operating pressures reveals different velocity patterns, as shown in Fig. 4.28. This comes from the fact that the particles do not have the same distribution and enrichment areas for all the operating pressures over the selected cross-sections (see Fig. 4.27). Furthermore, the resistance resulting from the particles strongly affects the velocity profile. In the vicinity of the dead-end, control line A, low operating pressure 1 *bar* leads to a wide distribution of particles over the cross-section and hence, the velocity profile has an almost parabolic form. When the operating pressure increases, the particles accumulate in the lower half of the capillary and form significant resistance to the fluid flow. This resistance disturbs the parabolic profile and causes a profile shift to the upper capillary part. The shift peaks sharply when the operating pressure increases to 3 *bar*.

Over control line B, C, Fig. 4.28, and when the flow increases, a relatively similar velocity profile to that over control line A is observed. However, the profile is slightly shifted at operating pressure of 2 *bar* due to the appearance of the particle accumulation areas. At operating pressure of 3 *bar*, the velocity profile has a symmetric parabolic distribution. This is ascribed to the low number of particles remaining in the capillary (6 %) and the flow resistance on the selected cross-section after 5 s of simulation is accordingly small.

A)

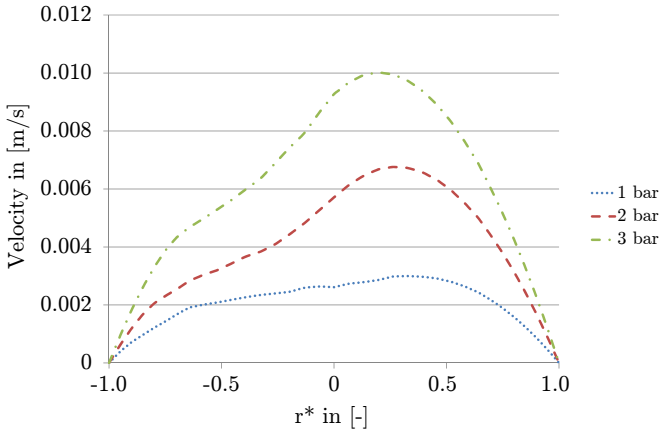

B)

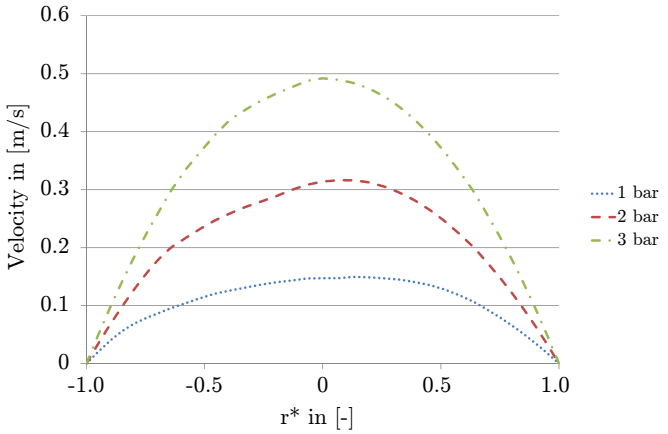

C)

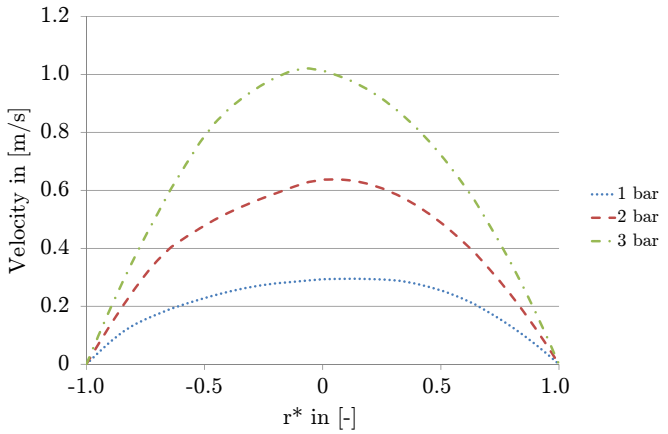

Figure 4.28: Velocity distribution of fluid at control lines A, B and C for operating pressures of 1, 2 and 3 *bar* and particle size of 10 μm and density of 1050 kg/m^3 after 5 s of simulation.

4.5.2 Effect of particle density

In order to study the particle recovery characteristics, different particle densities are simulated. In addition, these densities cover the latex particles of 1050 kg/m^3 and quartz particles which have a density of 2700 kg/m^3. The simulation here takes place at operating pressure of 2 bar and particle size of 10 μm. The heavy particles tend to settle on the membrane due to the gravity effect rather than be transported out of the capillary by the fluid. This tendency can be recognised when recovery of particles with two different densities is compared. In Fig. 4.29 and after 5 s of backwashing, it is found that the heavy particles mostly remain in the capillary, rather than the light particles which have approximately the same density as the fluid when the process is operated with the same conditions and particle size. After 5 s of the simulation, the portion of quartz particles remaining (2700 kg/m^3) is about 20 % of the initial value, whereas for latex particles (1050 kg/m^3) this portion has, remarkably, halved. In other words, due to the larger inertia moment, heavy particles move more slowly and towards the membrane surface. This behaviour postpones the particles leaving the capillary since particle enrichment areas appear at regions where the fluid velocity is low.

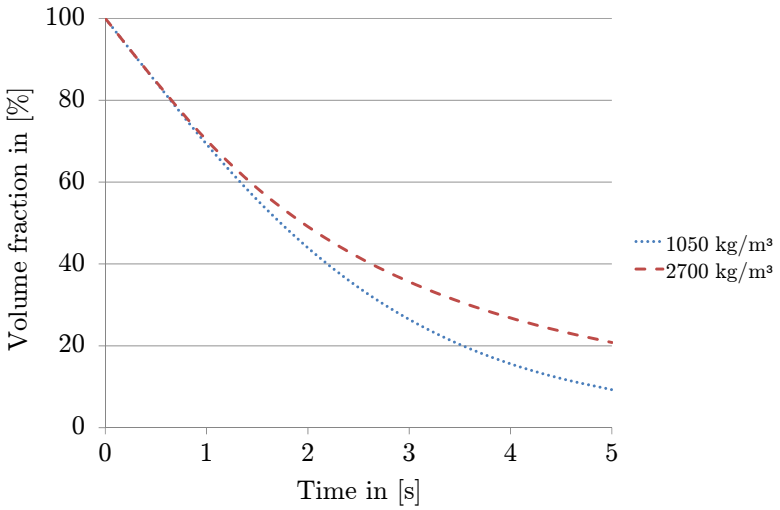

Figure 4.29: Recovery of the volume fraction of particles with diameter 10 μm at operating pressure of 2 bar for different densities in percent.

The accumulation of the particles near the membrane surface was found to be higher and closer to the membrane surface for heavy particles than for light particles. Due to the gravitational settling effect, the heavy particles have a high concentration gradient on the lower part of the capillary. The fluid entering from the inlet separates the particles from direct contact with the membrane. This also prevents the particles from depositing on the membrane surface and thus, reducing the performance of the backwash process. Furthermore, the density of the particles plays a significant role in the pressure

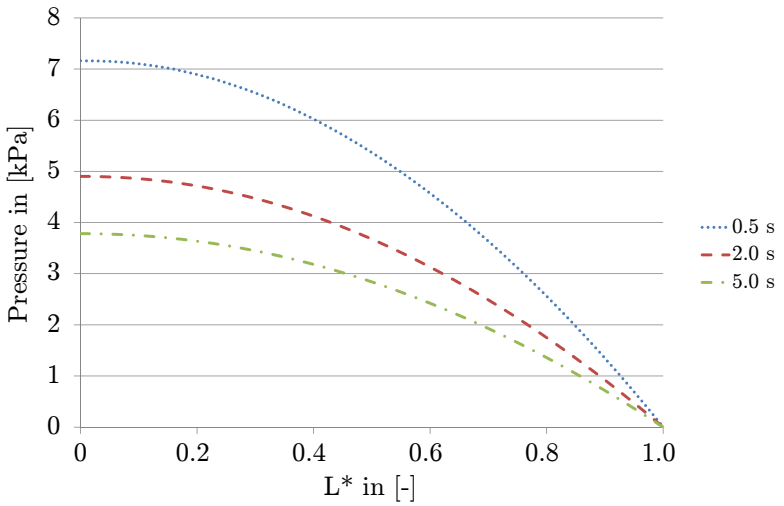

Figure 4.30: Pressure distribution over the capillary axis at 2 *bar* operating pressure and particle density of 2700 kg/m^3 and diameter of 10 μm.

drop inside the capillary. It is apparent from comparing Figs. 4.30 and 4.23 that the pressure distribution after 5 s for particles with a density of 2700 kg/m^3 is more than that for particles of 1050 kg/m^3. This is attributed to the need for higher energy to flush out the heavier particles. The influence of the particle volume fraction on the pressure distribution inside the capillary can also be recognised. Increasing the portion of the particles in the capillary is accompanied by an increase in the pressure drop.

The gravitational effect is dominant and causes particle accumulation areas on the bottom of the capillary, as illustrated in Fig. 4.31. The upper part of the capillary becomes relatively clean after 5 s of the simulation when, the particles

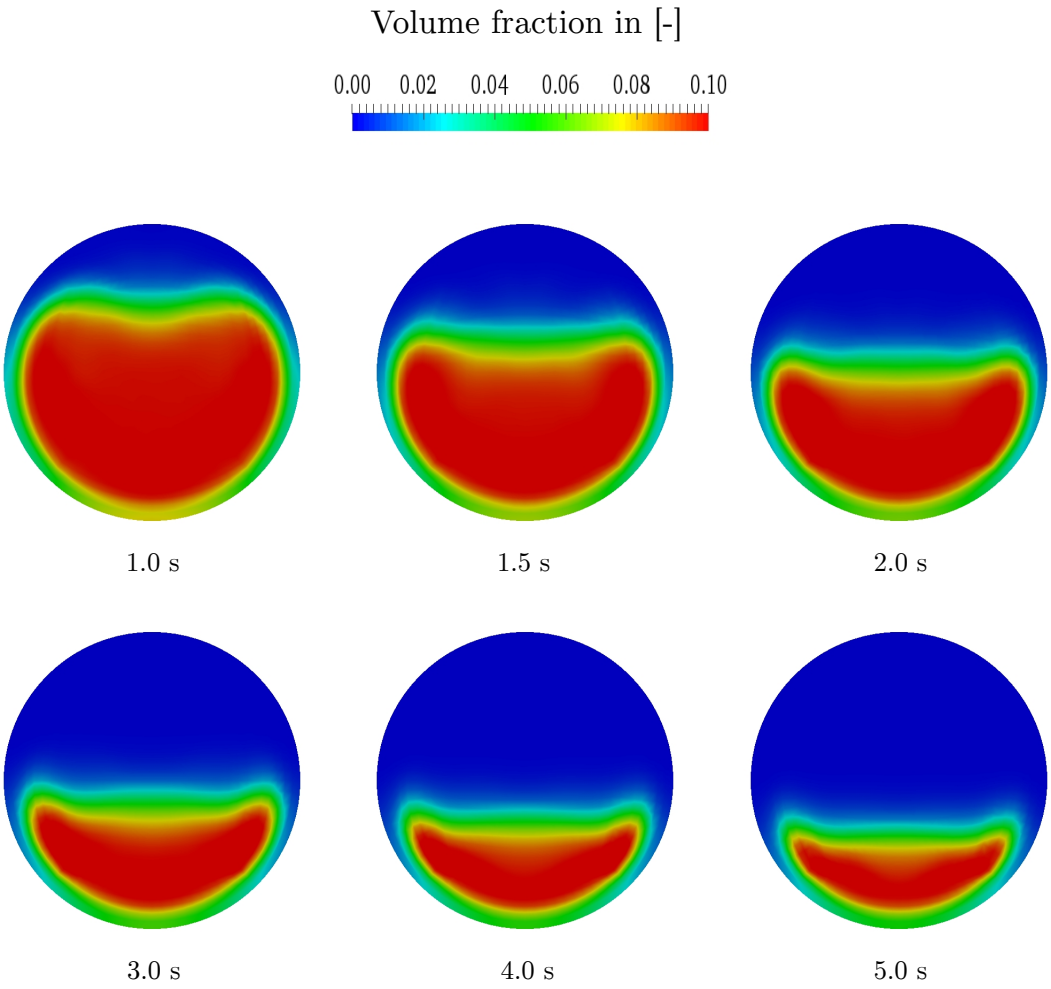

Figure 4.31: Particle distribution over capillary cross-section located at control line A for particles of 10 μm diameter and density of 2700 kg/m^3.

fall and fill the lower section of the capillary. Again, this non-homogeneous accumulation shifts the velocity profile and causes a deviation from symmetry at control lines A, B and C, as shown in Fig. 4.32. Furthermore, the peak velocities at the control lines exhibit higher values than for the same parameters with lighter particles, as in Fig. 4.19. These peaks appear due to the wider flow resistance caused by the wider distribution of particles over the lower half of the capillary after 2 s of the simulation. For heavier particles the maximum velocity on control lines A, B and C is 0.0072 0.35 and 0.69 m/s, respectively.

A)

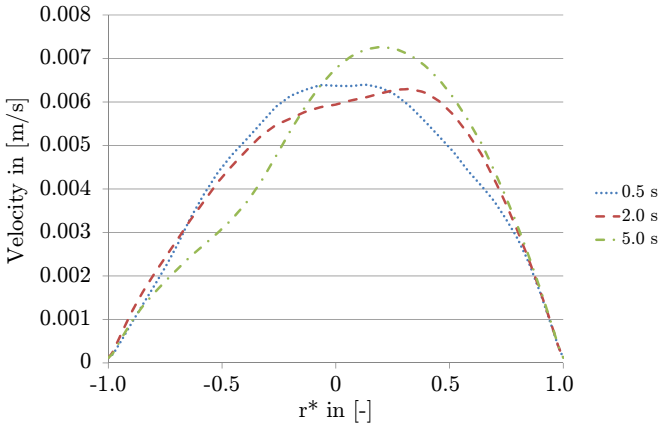

B)

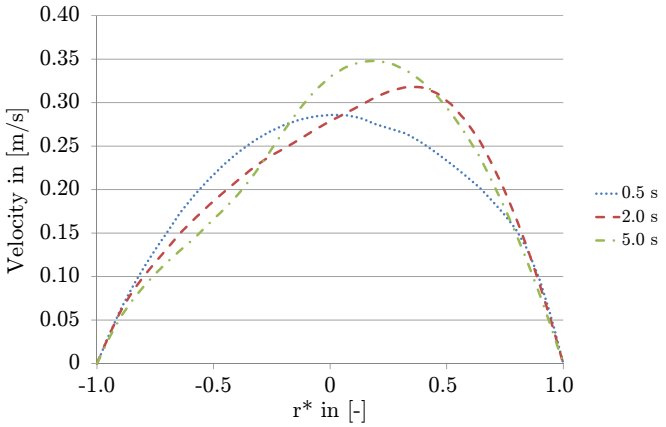

C)

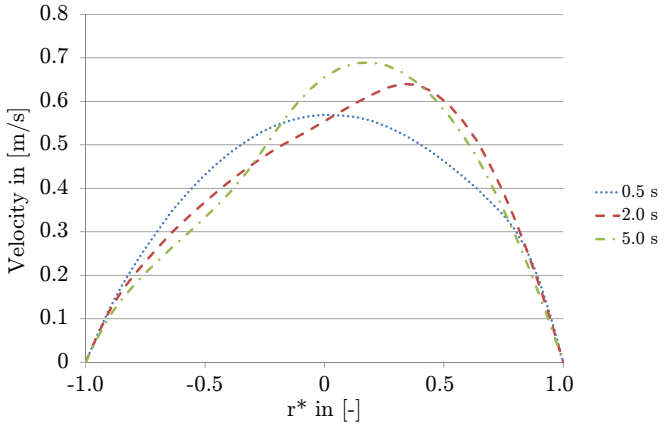

Figure 4.32: Velocity profile at control lines A, B and C for operating pressure of 2 bar and particle diameter of 10 μm and density of 2700 kg/m^3.

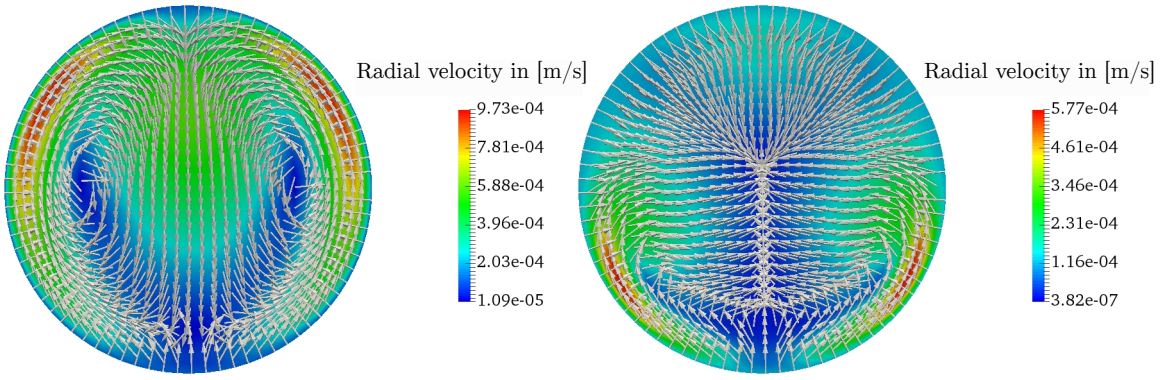

a) b)

Figure 4.33: Vector plot of radial flow after a) 0.5 s and b) 5 s of the simulation for 2 bar operating pressure and particle density of 2700 kg/m^3 at a location on control line A.

The heterogeneous distribution of the particles leads to a secondary flow in the radial direction. After 0.5 s of the simulation, the particles partly settle towards the bottom of the capillary, allowing the fluid to flow upwards, close to the membrane in the upper capillary section. Since the particles do not occupy the whole cross-section, an upward flow is induced in the opposite direction to gravity, which in turn enhances the downward flow in the centre of the capillary. In this case, a secondary flow develops with two recirculation zones, upward near the membrane and vertically downward in the centre. The strength of the secondary flow depends on the gap between the accumulated particles and the membrane. In the case of non-homogeneous particle distribution, the secondary flow has an inverse proportional relationship to the gap or clean area. The secondary flow induced after 0.5 s of the simulation is depicted in Fig. 4.33a. After 5 s the secondary flow is restricted to the lower section of the capillary. Here, the upper section is almost clean and the particles accumulate in the lower section, as seen in Fig. 4.31. Likewise, a small gap between the particles and the membrane drives the fluid upward and secondary flow is induced, as shown in Fig. 4.33b.

4.5.3 Effect of particle size

In Fig. 4.34, the removal of different sized particles is plotted as a function of the backwash time at a constant operating pressure of 2 *bar*. The removal of the particles appears to be almost non-sensitive to changes in particle size in the studied range. For particles with a diameter ranging from 2 to 20 μm, the particles remaining in the capillary after 5 s of backwashing are the same, and constitute about 10 % of the initial volume fraction. The momentum transfer from the fluid to the suspended particles seems to be similar for the studied particle size range. The drag force exerted on the particles is related to particle diameter. However, under the conditions considered, this correlation does not significantly influence either the distribution of the particles, nor their removal. For 2 μm diameter particles, there is a deviation from the identical pathway for other sizes due to the small particle inertia, i.e. small particles are transported faster out of the capillary, as shown in Fig. 4.34. In contrast, for particles with a 10 and 20 μm diameter, different behaviour is imperceptible. Thus, the variation in particle size does not significantly affect particle removal. The development of secondary flow in the cross-section of the capillary is observed independent of particle size.

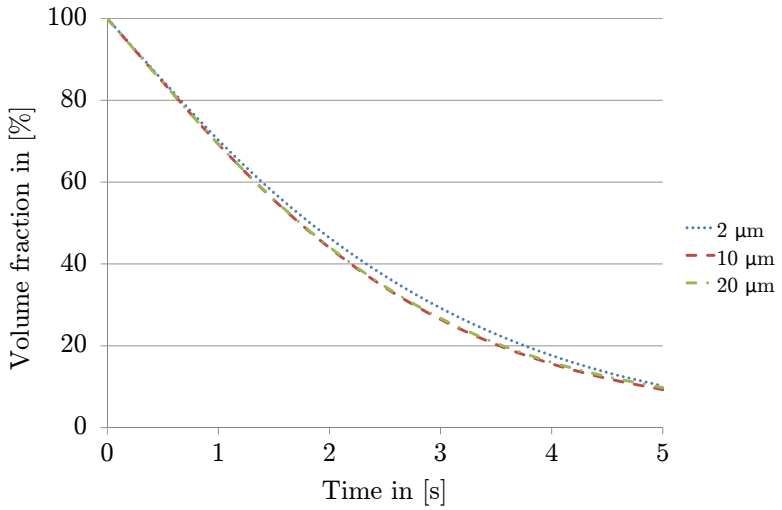

Figure 4.34: Recovery of the volume fraction of particles of different sizes in percent.

4.6 Even particle deposition

The capillary configuration investigated in this section is more realistic and can appear in the capillary after running the filtration process in dead-end mode. The particles are uniformly deposited on the membrane on the inner surface of the capillary with a thickness of 125 μm and packing density of 0.5. This initial distribution is depicted in Fig. 3.8. Numerical simulations have been run for 5 s quantifying the effect of the particle density and size in addition to different operating pressure profiles which are applied to perform the backwash process. These pressure profiles are illustrated in Fig. 3.11. The considered particles are mono-disperse with a constant diameter. Evaluation of the particle behaviour involves two definitions: the local volume fraction and the volume fraction expressed in percent. The first definition refers to the value at a certain position, whereas the other definition is used to describe the removal of the particles during the backwash, independent of the initial volume fraction, i.e. portion of particles is 100 % at the beginning and decreases over time until reaching a clean state at 0 %.

Velocity profile

The velocity profile indicates the same tendency along control lines A, B and C over time with different maximum values. The velocity distribution is shown in Fig. 4.35. After 0.5 s, the particles are still symmetrically distributed over the cross-section and barely detach from the membrane. The velocity profile is accordingly symmetrical. The buckling curve near the membrane results from the accumulation of particles where the velocity deceases. In other words, the accumulation of particles near the membrane and the absence of particles in the centreline region lead to the development of sharply curved parabolic velocity profiles.

Within 2 s at control line A, the velocity profile bends toward the upper half of the capillary as the particle concentration decreases. Moreover, the velocity in the lower half becomes slower due to the high concentration of particles,

A)

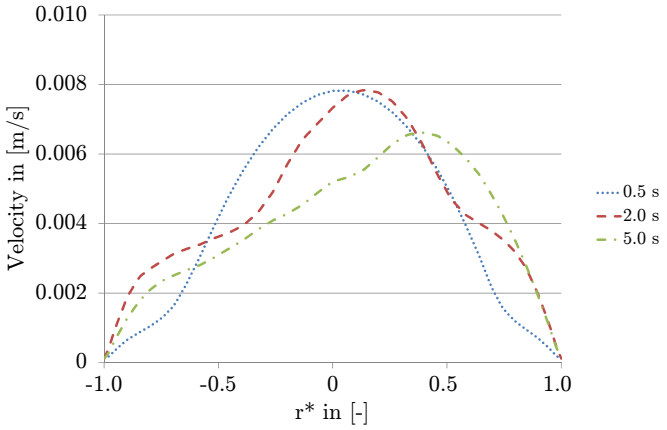

B)

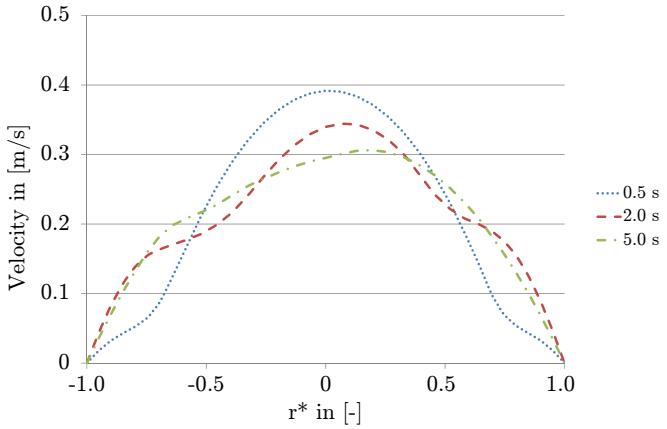

C)

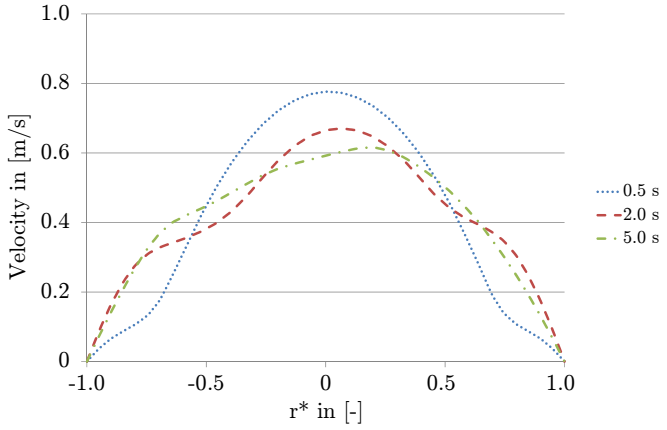

Figure 4.35: Fluid axial velocity at control lines A, B and C at operating pressure of 2 *bar* and particle size of 10 μm and density of 1050 kg/m^3.

whereas the velocity profile at control lines B and C maintains its symmetrical form with a small upward bend.

After 5 s, the upper half of the capillary is almost clean and some of the particles are removed from the capillary while the others accumulated in the lower half with a small volume fraction. This again shifts the peaks of the velocity profile upward. The maximum velocity at a control line is dependent on the concentration of particles over that line, which changes over time.

During the backwash process, a secondary flow is induced in the capillary cross-section which has a significant impact on particle distribution. The secondary flow appears when the resistance caused by the particles is not uniformly distributed in the capillary cross-section. Fig. 4.36 shows the development of the secondary flow over the simulation time of 5 s.

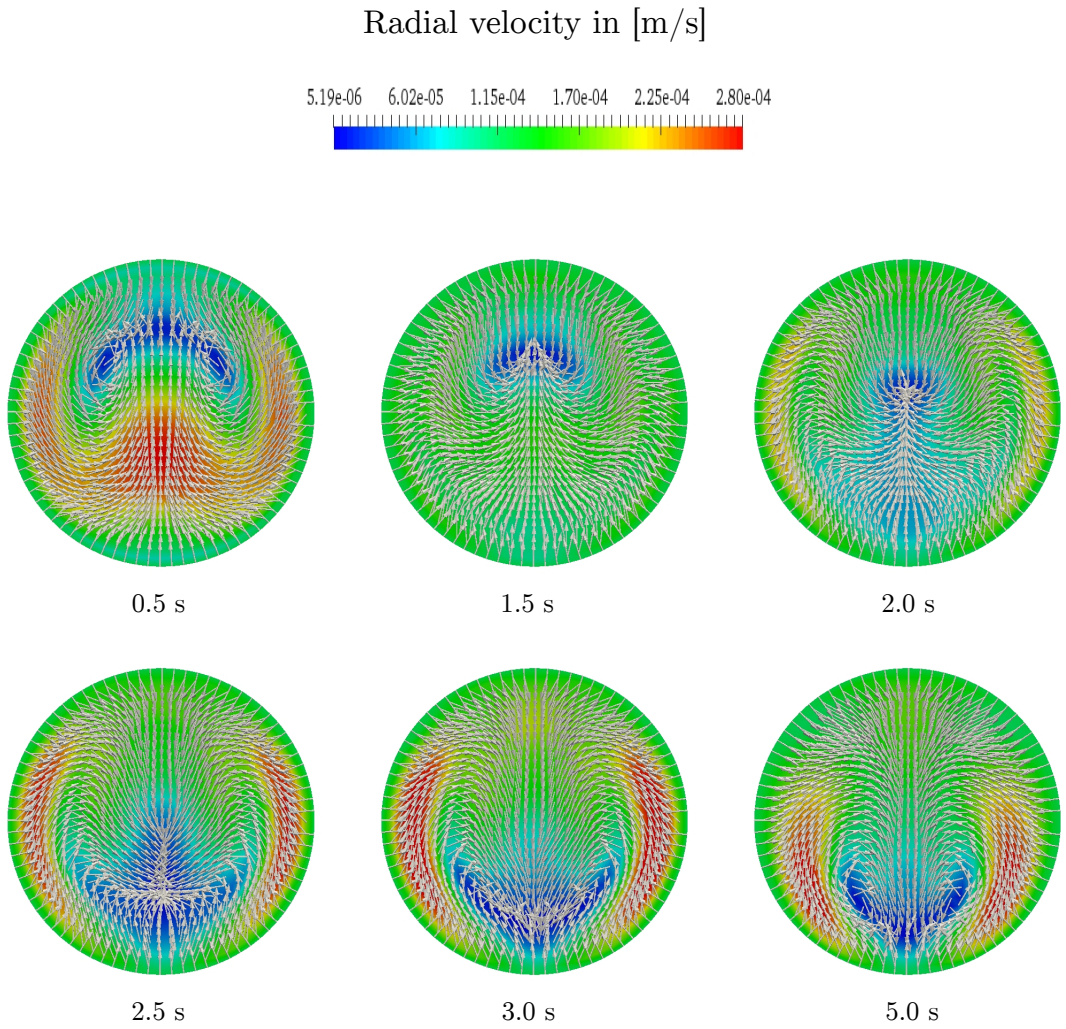

Figure 4.36: Vector plot of secondary flow over the simulation time for 2 *bar* operating pressure and particle size of 10 μm at a location on control line A.

The following section includes more details about the origin of the secondary flow and its correlation with the particle distribution.

Particle distribution

In the vicinity of the membrane, the concentration of particles decreases as a result of the permanent entry of clean fluid. The deposited particle layer is transported in its annular form toward the capillary centre, and becomes

narrower. Fig. 4.37 shows the change in the particle distribution over the control lines during the backwash process. Here, three stages of particle distribution can be distinguished. The first stage can be seen after 0.5 s, when the particles detach from the membrane and move in the direction of the capillary centreline due to radial velocity. Some of the particles are flushed out of the capillary, carried by the fluid axial velocity. Here, almost symmetrical distribution of particles is observed in the three positions, A, B and C, with peak values referring to the initial volume fraction of 0.5. The particles have not yet reached the centre of the capillary and the volume fraction in the axis region is therefore zero. The second stage reveals a deviation from symmetrical particle distribution due to secondary flow effects. At this stage, the volume fraction of particles in the lower half of the capillary is much greater than in the upper half and is disseminated over a wider area. Moreover, the annular form of the particle volume fraction becomes thin in the upper half and thick in the lower half due to the accumulation of particles. This stage is achieved within 2 s of the simulation. The third stage appears after 5 s of simulation. The particles reach the centre of the capillary, driven from the vicinity of the membrane, and the volume fraction in the upper half is almost zero. The particles accumulate in the lower half and at the same time the volume fraction decreases due to the flushing out of the capillary. The fluid axial velocity is responsible for the transport of the particles towards the outlet whereas the radial velocity has an important roll in the distribution of particles inside the capillary.

A better understanding of the correlation between fluid velocity and particle concentration can be achieved by comparing Figs. 4.35 and 4.37. Fluid velocity increases when particle concentration decreases. This relationship can be clearly observed on control lines A, B and C. Fig. 4.38 also shows the development of the secondary flow in the capillary cross-section over time in addition to the variation in the recirculation zones according to changes in particle distribution. At the beginning, the fluid entering the membrane drives the deposited layer towards the capillary centreline. After 0.5 s, a gap between the membrane and the deposited layer arises where the volume fraction is very small. The fluid in this gap flows downwards due to the gravitational effect. This motion induces

A)

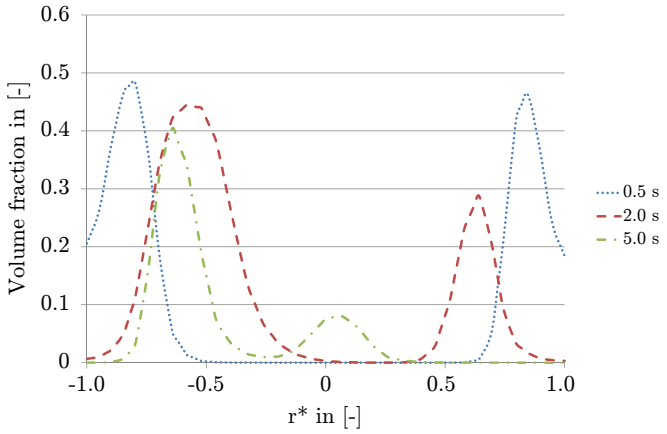

B)

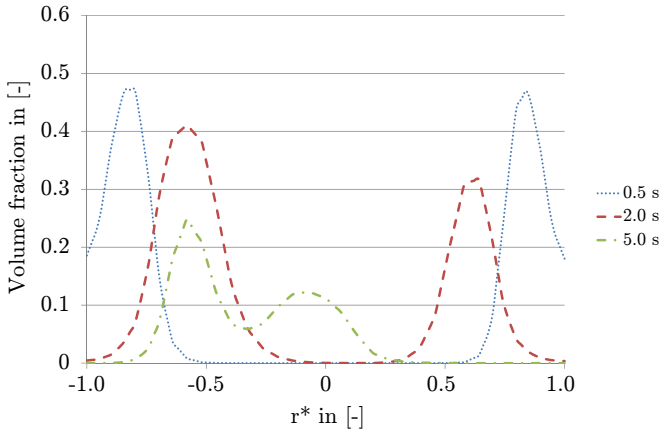

C)

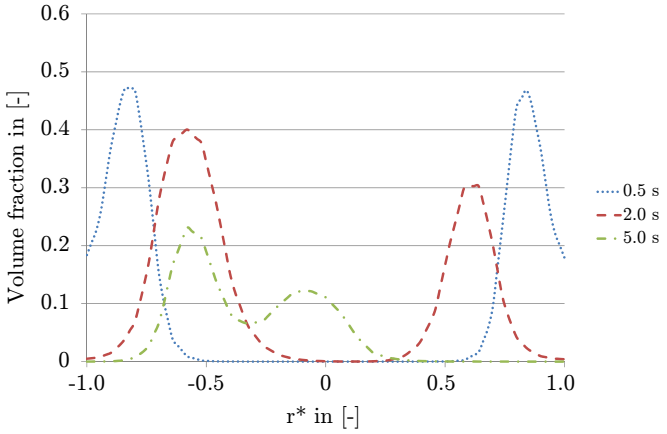

Figure 4.37: Local volume fraction of particles on control lines A, B and C, operating pressure of 2 bar and particle size of 10 μm and density of 1050 kg/m^3.

two recirculation zones inside the deposited layer. The layer restricts them. The secondary flow drives a portion of the particles from the upper half of the capillary to the lower half. Thus, the volume fraction drifts from symmetrical distribution and decreases as a result of the axial fluid velocity which transports the particles to the outlet. Over time, these two recirculation zones become smaller as the deposited layer is displaced towards the centreline. After approximately 2 s, the recirculation zones vanish from inside the deposited layer and begin to form around it. However, the decrease in particle volume fraction in the upper capillary half compared with that in the lower half induces recirculation zones around the deposited layer. The outer recirculation zones are shown after 3 s in Fig. 4.38.

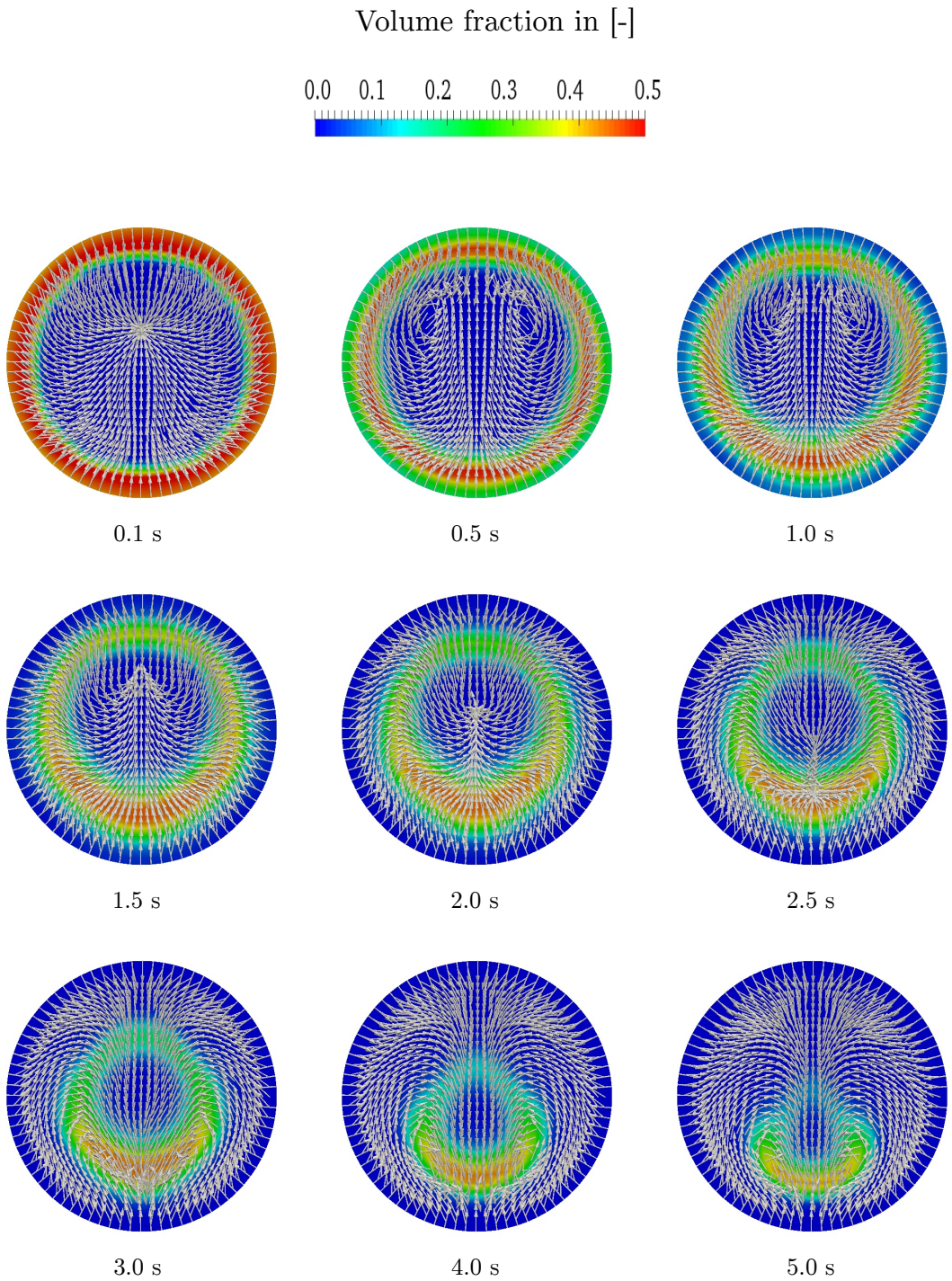

Figure 4.38: Vector plot of secondary flow and particle volume fraction over the simulation time for 2 *bar* operating pressure and particle size of 10 μm at a location on control line A.

Pressure drop

The pressure drop depends on the volume fraction of particles inside the capillary, among other things. For the case under investigation this value is initially 18 % of the total capillary volume. A high volume fraction is associated with large pressure drop. In Fig. 4.39, the pressure distribution inside the capillary over time is illustrated. The highest pressure value is observed at the dead-end, whereas the lowest is an atmospheric pressure at the capillary outlet. Initially, there is a large pressure drop inside the capillary of 5.6 kPa. The pressure drop increases while the deposited particles are being carried from the membrane towards the capillary centre. When the membrane is almost clean and the majority of particles have been removed from the capillary, the pressure drop decreases and reaches about 3.2 kPa after 5 s.

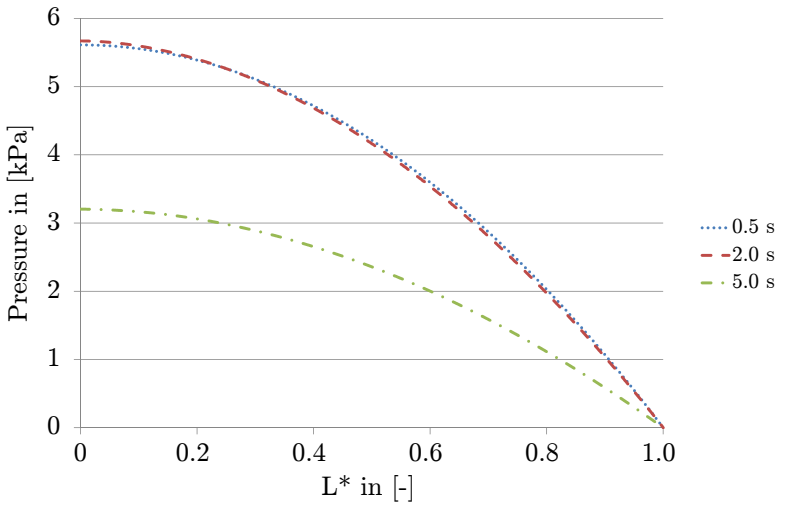

Figure 4.39: Pressure distribution over the capillary axis at operating pressure of 2 bar and particle size of 10 μm and density of 1050 kg/m^3.

Comparing the values for the pressure drop with these obtained in the previous section (see Figs. 4.23 and 4.39), it is obvious that they are similar despite the different initial distribution of the particles. However, they are not identical because the particle volume fraction after 5 s is not the same in both cases.

4.6.1 Effect of operating pressure

Describing the removal of particles and their behaviour inside the capillary membrane is achieved by incorporating different operating parameters in the calculation for realistic deposition of particles. For this reason, three operating pressures, 1, 2 and 3 *bar* are applied to the capillary membrane for a constant particle diameter of 10 μm in order to transport the deposited particles towards the capillary outlet. This enables evaluation of the efficiency of the backwash process. For an operating pressure of 1 *bar*, it can be observed that after 5 *s* of the simulation, more than 50 % of particles remain in the capillary. Increasing the operating pressure to 2 *bar* reduces the particles remaining in the capillary to 18 %. A large portion of the particles (nearly 95 %) located on the membrane are removed within the first 5 *s* with an operating pressure of 3 *bar*. The numerical results show a high level of agreement with the experimental data done by Keller, et al. [115]. They performed three experiments involving backwashing a capillary membrane filtered with silica particles with a mean particle size of 5 μm under a constant operating pressure of 3 *bar*. They found that the recovery of the particles after 5 *s* of backwashing is about 93 %. The recovery of the particles for three backwashing pressures is depicted in Fig. 4.40.

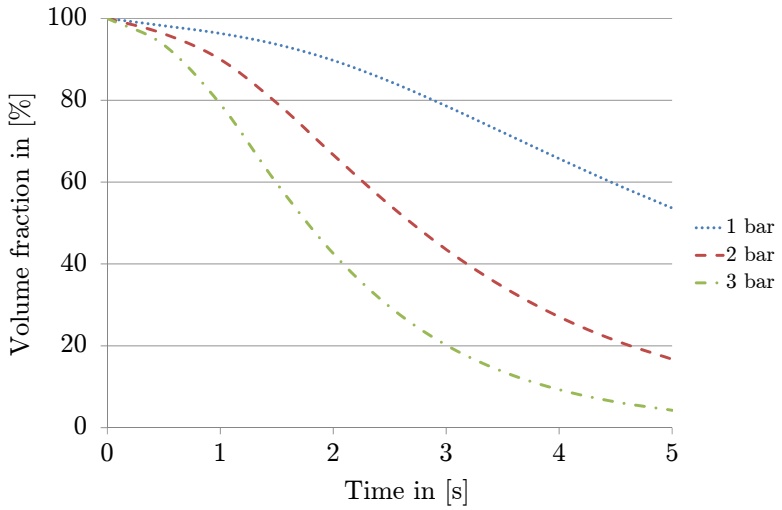

Figure 4.40: Recovery of the volume fraction of particles with diameter of 10 μm and density of 1050 kg/m^3 through different operating pressures in percent.

The amount of water which is used for backwashing the capillary for different operating pressures during 5 s is given in Table 4.5

Table 4.5: The volume of water used for the backwashing the capillary under different operating pressures and over the backwashing time.

Operating pressure bar	Amount of used water mL
1	1.28
2	2.53
3	3.78
4	5.05

It is of interest to observe the development of the velocity over time in the different positions inside the capillary: control lines A, B and C. Fig. 4.41a shows the velocity distribution over the control lines after 5 s of simulation at three operating pressures. For 1 bar operating pressure, the velocity at the control lines is very small compared with that for 3 bar operating pressure. The difference in the efficiency of the backwash process in removing the particles from the capillary can be ascribed to this. Furthermore, the velocity profile for the cases under investigation has a similar tendency, i.e. velocity increases in the zones where the volume fraction decreases. This means the maximum velocity can vary according to changes in particle distribution over the cross-section.

Near the dead-end, the low velocity and the high concentration of particles in the lower half of the capillary have significant effects on the velocity profiles. The previously mentioned factors result in an upward shift in the maximum velocity where the resistance of the particles is low. The velocity profile thereby deviates from the symmetrical. The maximum velocity for operating pressures 1, 2 and 3 bar on control line A is 0.0034, 0.0065 and 0.012 m/s, respectively. The resistance caused by the particles can be overcome when the flow velocity increases, which is seen on control lines B and C in Fig. 4.41a. The maximum velocity on control line B after 5 s for operating pressures 1, 2 and 3 bar is 0.16, 0.31 and 0.48 m/s, respectively, whereas for the same operating pressures the maximum velocity on control line C is 0.3, 0.61 and 0.98 m/s, respectively.

Particle distribution is influenced by both the radial and axial velocity in the capillary. On the one hand, radial velocity transports the particles towards the capillary centreline and thus changes the particle distribution in the cross-section. On the other hand, axial velocity drives the particles in the direction of the outlet and thus contributes to the cleaning of the capillary. The impact of radial velocity is clearly seen near the membrane where the particles accumulate at a distance of 0.5 mm from the membrane, where zones of high particle concentration appear. In contrast, radial velocity causes a decrease in the volume fraction in these accumulation zones. The higher the flow velocity, the smaller the volume fraction in these zones.

For instance, at 1 bar operating pressure, the particle distribution has an annulus form. Due to the radial velocity, the deposited layer is detached from the membrane and driven towards the capillary axis. After 5 s at control line A, the volume fraction of particles in the upper half of the capillary (0.1) decreases faster than in the lower half (0.47) due to the secondary flow which carries the particles downwards. Thus, the volume fraction there has a relatively high value, as seen in Fig. 4.41b. The volume fraction has the same tendency at control lines B and, C but with different values because of a higher axial velocity which carries the particles out of the capillary. For operating pressures 2 and 3 bar, the deposited layer tends to behave similarly, with the difference that the portion of particles in the upper capillary half reaches the capillary centreline with lower volume fraction values due to higher axial velocity there.

Observing the pressure drop inside the capillary during the backwash process shows that the pressure drop first increases when the deposited particle layer begins to detach from the membrane. It reaches its peak value before it starts to decrease. Many factors influence this peak value, including operating pressure, particle diameter and density and the thickness of the deposited layer. The profile of the pressure drop can vary from a sharp peak at an operating pressure of 3 bar where the maximum pressure drop over the capillary length is reached after 0.8 s, to a more flat profile at an operating pressure of 1 bar. This

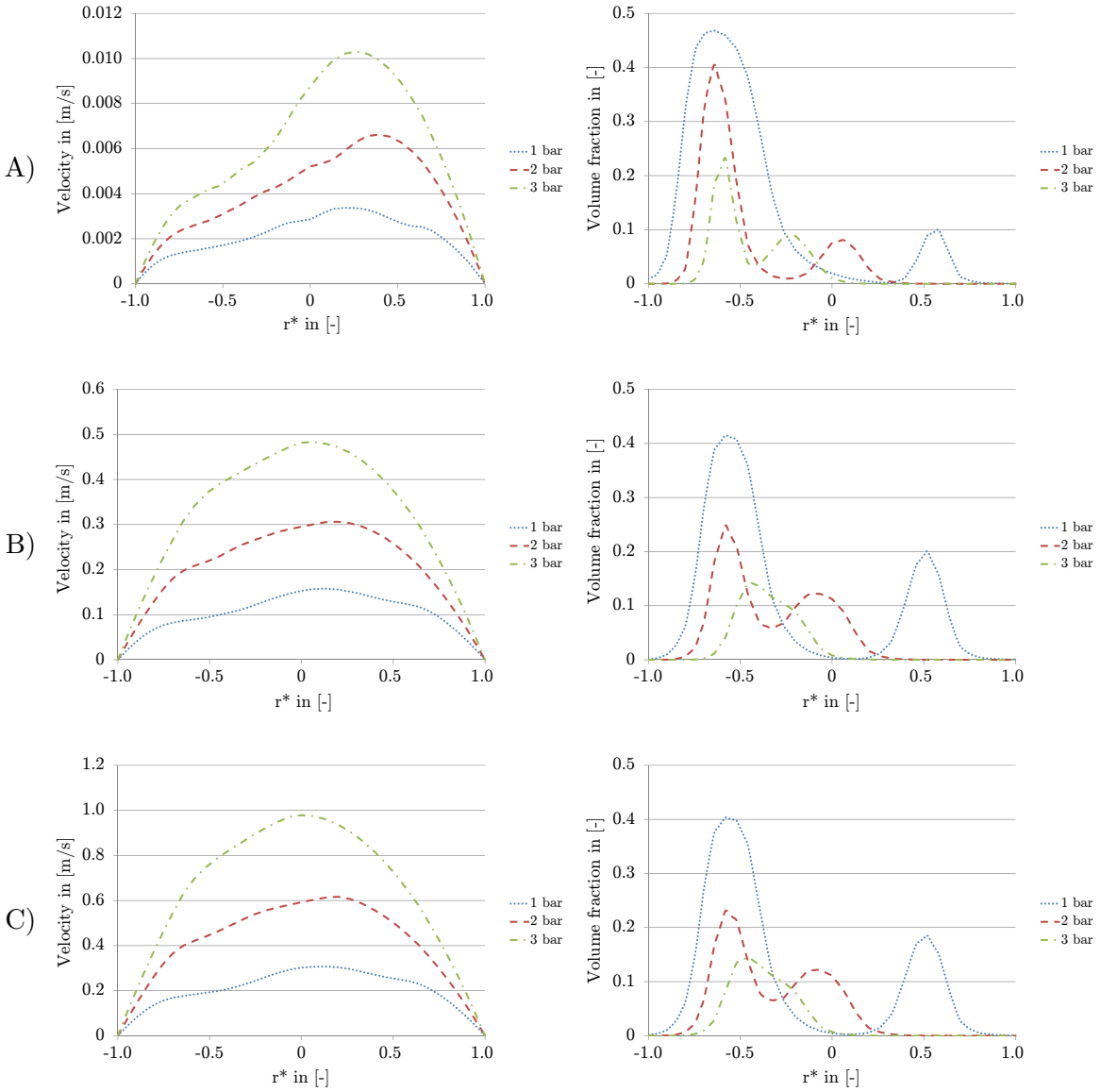

Figure 4.41: At control lines A, B and C a) fluid velocity distribution and b) particle distribution at different operating pressures and particle size of 10 μm and density of 1050 kg/m^3 after 5 s of simulation.

happens due to the fact that high pressure is required to drive the deposited particle layer away from the membrane. When the particles leave the membrane, the pressure drop begins to decrease. Keeping the other parameters

constant, pressure drop has a proportional relationship to operating pressure. This relation is seen in addition to the pressure drop profile in Fig. 4.42. As the particles reach a certain distance from the membrane in the capillary, the pressure drop begins to decrease. This distance also depends on the operating parameters and the properties of the particles. Therefore, the flat pressure drop profile is observed when the operating pressure is low and the fluid velocity accordingly small. In contrast, for high operating pressure, faster fluid velocity determines a sharp peak in the pressure drop profile.

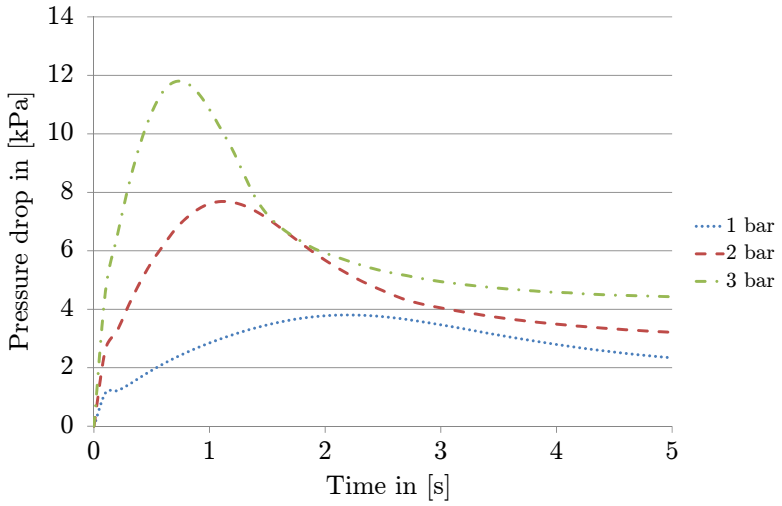

Figure 4.42: Pressure drop inside the capillary membrane over the simulation time for different operating pressures and particles with diameter of 10 μm and density of 1050 kg/m^3.

4.6.2 Effect of particle density

Heavy particles do not follow the fluid and tend to settle down. This behaviour makes the removal of particles much more difficult compared to the removal of particles with a density similar to that of the fluid. A comparison of the removal of particles of two different densities under the same operating conditions is shown in Fig. 4.43. Around 50 % of the heavy particles remain in the capillary after 5 s of the simulation. The result confirms that transport efficiency falls when particle density increases. That means in order to flush

heavy particles out of the capillary an extension of the backwashing time is required. According to the curve tendency in Fig. 4.43, to achieve a clean capillary, the backwashing time must be doubled.

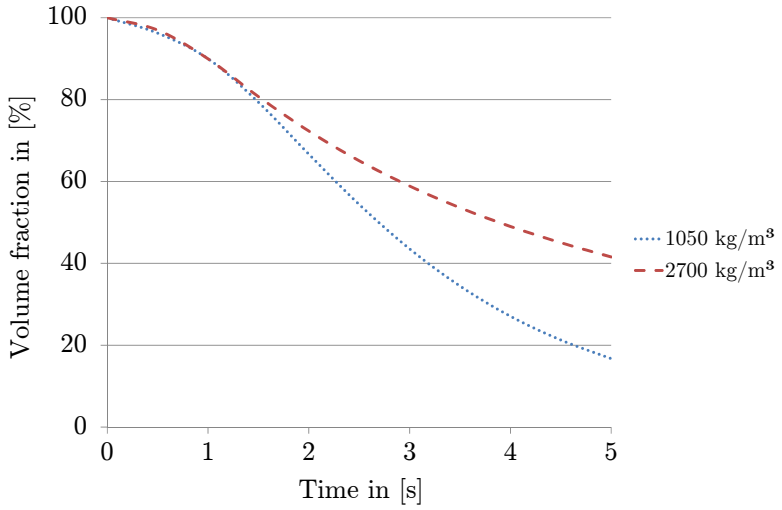

Figure 4.43: Recovery of the volume fraction of particles with diameter of 10 μm and density of 2700 kg/m^3 and 1050 kg/m^3 in percent at operating pressure of 2 bar.

The simulation shows that in the case of heavy particles a secondary flow occurs in the cross-section of the capillary, see Fig. 4.44. This secondary flow has a significant influence on the distribution of particles inside the capillary. Furthermore, a complicated relationship governs the particle distribution and secondary flow. They influence each other. At the beginning of the simulation, the secondary flow transports particles from the upper half of the capillary to the lower half. Moreover, this motion is encouraged by the gravitational effect. Although particles are flushed out of the capillary by the axial fluid velocity, particles from the upper half compensate for the loss in volume fraction and thus, the particle accumulation region appears in the lower half of the capillary. The fluid continuously entering the capillary prevents the accumulation region from coming into contact with the membrane and a gap filled with fluid forms between them. This is lifted by a certain distance, according to the operating pressure and particle density, among other factors. The formation and development of particle accumulation region near the lower membrane causes a

high potential clogging of the capillary or even the lower part of the capillary, especially when the packing density of the particles in this region reaches the initial packing density of the deposited layer. Furthermore, this region extends the backwashing time due to the low axial velocity which dominates in them.

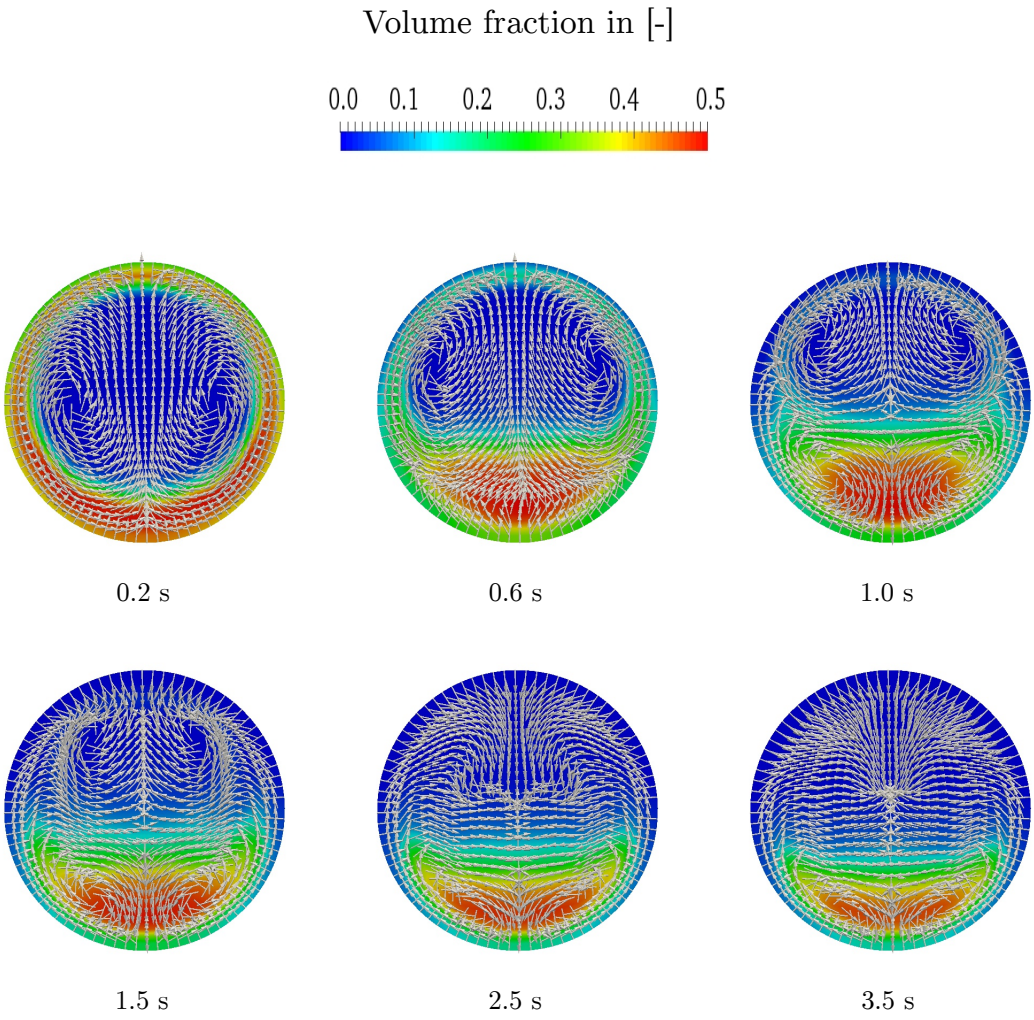

Figure 4.44: Vector plot of secondary flow and particle volume fraction over the simulation time for 2 *bar* operating pressure and particle size of 10 μm and density of 2700 kg/m^3 at a location on control line A.

The origin of secondary flow is uneven distribution of particles, as mentioned above. The development of the secondary flow with recirculation zones, in addition to its relationship with the distribution of the particles is shown in

Fig. 4.44. When a portion of the particles is still in the upper part of the capillary, the induced secondary flow reveals two recirculation zones, one on each side of a vertical plane. Over time and when the volume fraction of particles noticeably increases in the lower part of the capillary, the flow of the fluid displays high resistance, caused by the accumulated particles. Thus, the recirculation zones become smaller bounded by the accumulated particles from the bottom part. As the accumulation region becomes thicker, additional two recirculation zones are generated in the lower half of the capillary. These zones can be clearly seen after about 1 s of the simulation and in each capillary quarter. This is due to more non-homogeneous distribution of particles in the capillary cross-section. As the upper part is completely clean, the fluid entering reverses direction from downwards to upwards. Simultaneously, the two recirculation zones induced in the upper part slowly vanish and the accumulation region becomes wider. Here, after 3.5 s of the simulation, the volume fraction of the particles decreases due to the axial fluid velocity, however, the secondary flow disappears when the capillary is completely empty of particles.

Similar behaviour is observed on the other control lines. The particles leave the upper part of the capillary within a short time due to the induced secondary flow and gravitational effect and accumulate in the lower part, as shown in Fig. 4.45b. Following this, the volume fraction decreases when the particles move towards the outlet. The axial velocity has a shifted profile due to the particle distribution across the capillary section. This profile changes over time according to the particle distribution. Fig. 4.45a illustrates the axial velocity on control line C.

At the beginning the pressure drop inside and over the length of the capillary increases to transport the heavy particles away from the membrane. The greater the density difference between the particles and the carrier fluid, the greater the pressure drop. Fig. 4.46 shows a peak value which exceeds 10 kPa after 0.8 s for heavy particles. After this, the pressure drop begins to decrease. This moment depends on the particle density and the thickness of the deposited

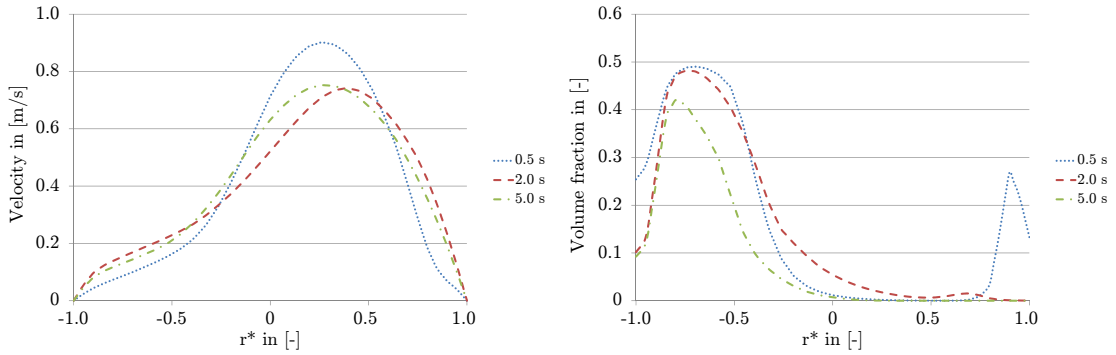

a) b)

Figure 4.45: At control line C, a) Velocity distribution and b) local volume fraction of particles with density of 2700 kg/m^3 and diameter of 10 μm and 2 bar operating pressure over the simulation time.

layer, among other things. The two lines in Fig. 4.46 which represent the pressure drop for different particle densities meet when all the particles are flushed out of the capillary.

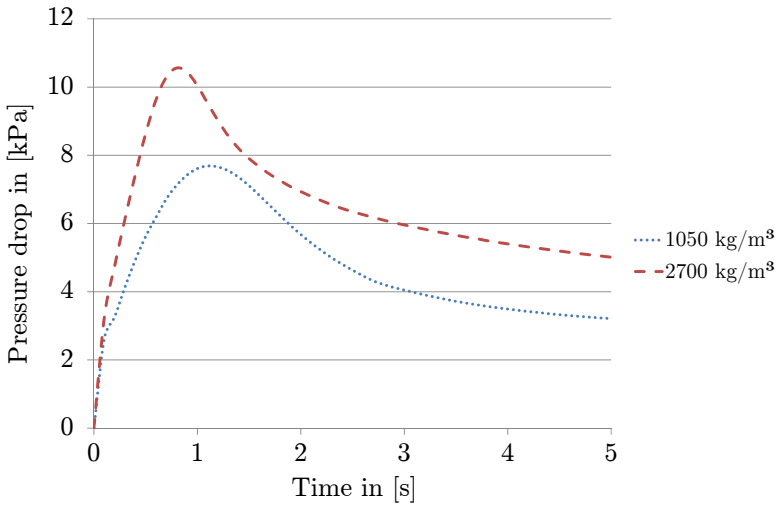

Figure 4.46: Pressure drop inside the capillary membrane over the simulation time for particles with diameter of 10 μm and different particle densities at operating pressure of 2 bar.

4.6.3 Effect of particle size

To highlight the effect of particle size during the backwash process, the simulation is carried out for particles with different diameters, namely, 2, 10 and 20 μm. These particles have the same material properties in term of density and shape and are subjected to the same operating parameters. Fig. 4.47 shows the efficiency of the backwash process over time for different particle diameters. The removal of particles with different diameters under the same operating conditions is about 82 % after 5 s. Small particles (2 μm) follow the streamlines and are flushed out faster than larger ones (10 and 20 μm) due to the fact that inertial and gravitational effects are insignificant for small particles. In contrast, the larger particles display quite similar behaviour and removal efficiency.

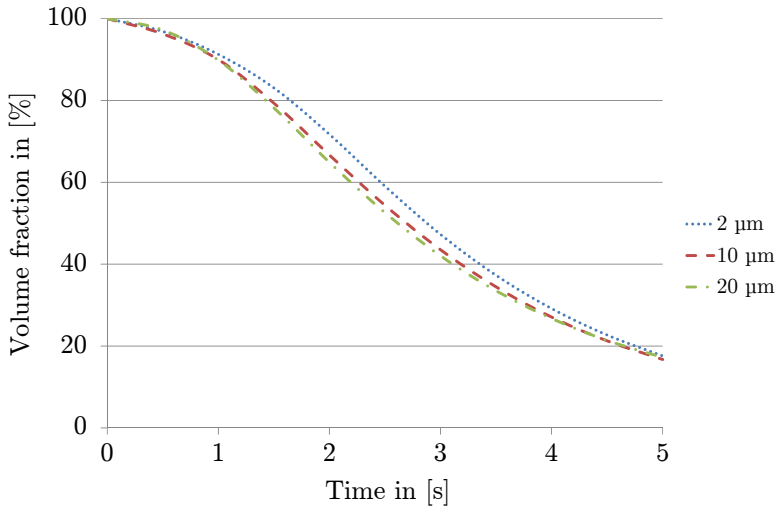

Figure 4.47: Recovery of the volume fraction of particles with density of 1050 kg/m^3 and different diameters in percent at operating pressure of 2 bar.

For a deposited layer with particles with a small diameter, symmetrical particle distribution in horizontal and vertical planes is observed during the simulation. On control lines A, B and C (see Fig. 4.48a), the particles have less of a tendency to settle and instead remain suspended in the carrier fluid. This symmetrical distribution around the capillary axis is disturbed after about 3 s due to the induced secondary flow over the capillary cross-section. Secondary

flow develops when the particle distribution deviates from a symmetrical distribution. However, the concentration of particles with a diameter of 20 μm displays a gradual increase in a downwards direction due to the significant gravitational effect. The accumulation of the particles in the lower half of the capillary can be seen in Fig. 4.48b. Gravity induces the settling of the particles which in turn causes a deviation from symmetrical distribution around the capillary axis. As a result, secondary flow develops and then contributes to the particle distribution in the capillary cross-section. Thus, for larger particles, secondary flow is induced within a very short time whereas for smaller particles the formation of this secondary flow is accompanied by the appearance of the gravity effect on their distribution. In other words, the deposition of large particles onto the lower part of the membrane is much greater than for small particles which remain mostly symmetrically suspended in the cross-section. Larger particles accumulate on the lower membrane and thereby disturb the backwash process when particles plug the capillary.

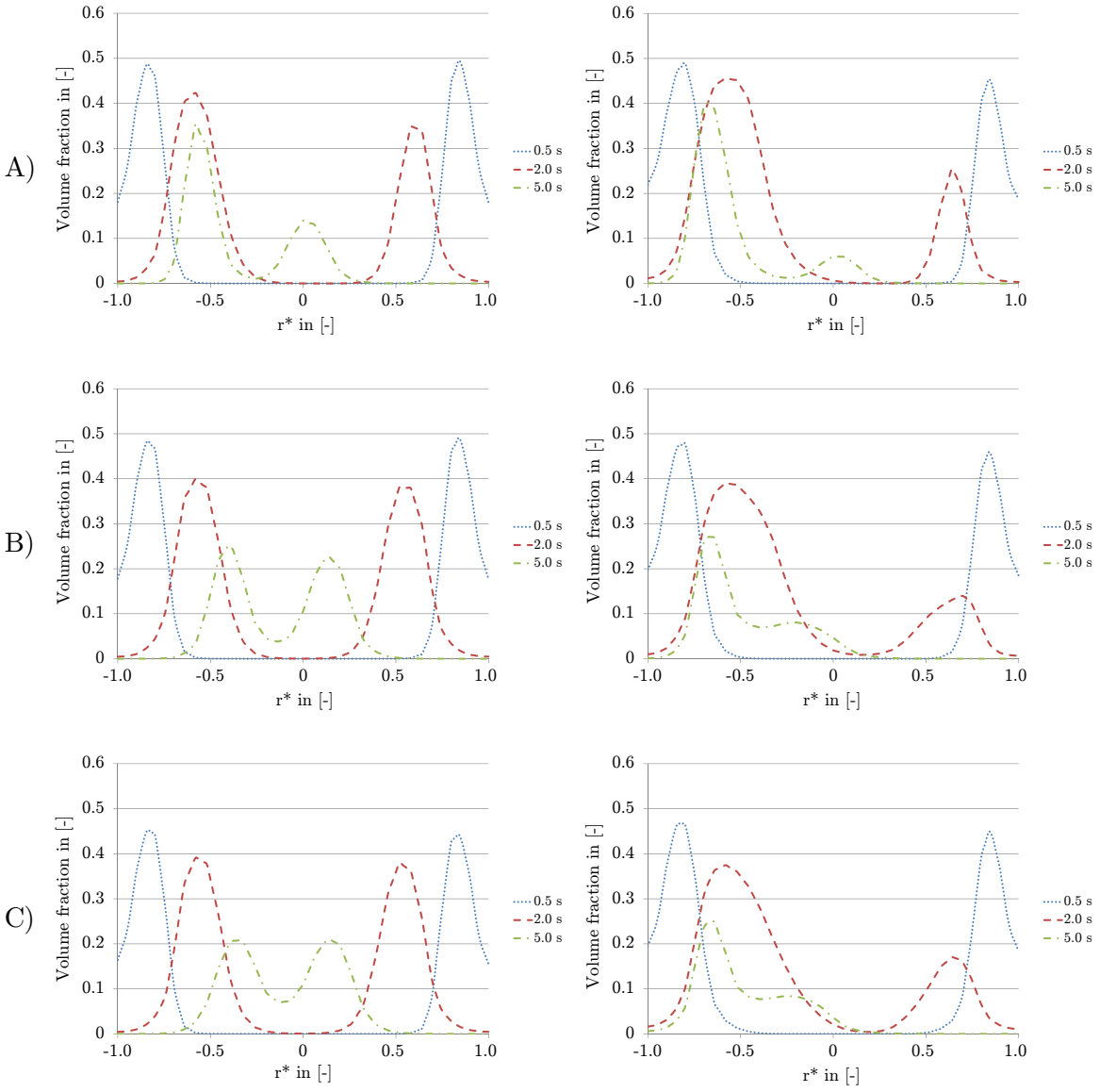

Figure 4.48: Particle distribution at control lines A, B and C for different particle diameters: a) particle diameter of 2 μm and b) particle diameter of 20 μm at 2 *bar* operating pressure over the simulation time.

4.6.4 Effect of pressure profile

Further analysis of the backwash process is performed by considering different operating pressure profiles. These profiles are illustrated in Fig. 3.11 and allow the same amount of backwashing water to enter the capillary. The volume of water used in order to backwash the considered capillary and referred to by the profiles within the backwash time (5 s) is 2.83 mL. The particle removal diagram in Fig. 4.49 shows that variation of the operating pressure during the backwash process has a negligible effect on the efficiency of the particle removal. After 5 s of backwashing, the portion of the remaining particles is similar for the applied pressure functions, however the trend of each function differs according to the entered volume of backwashing water. When the operating pressure is high (3 bar), the particles are transported out of the capillary faster, whereas the efficiency of particle removal decreases when the operating pressure declines. Thus, the profile of the operating pressure does not play a significant role when the adhesive forces on the membrane are not taken into account.

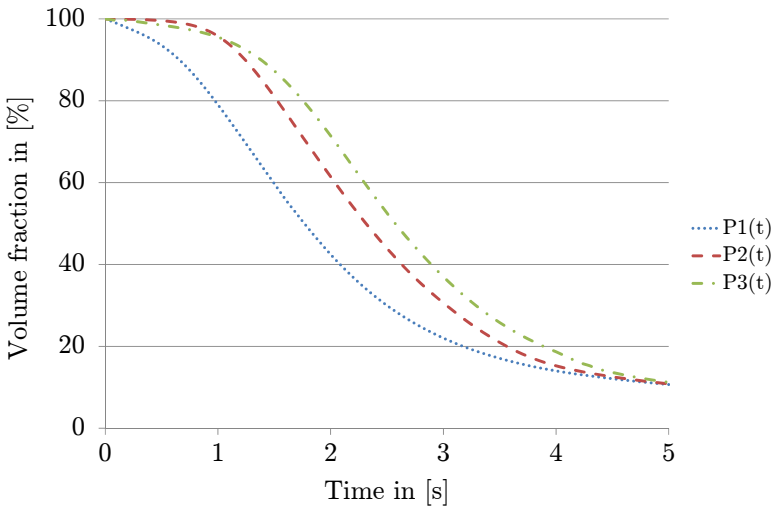

Figure 4.49: Recovery of the volume fraction of particles with density of 1050 kg/m^3 and diameter of 10 μm in percent at different operating pressure profiles.

4.6.5 Effect of tightly adhered particles

It is assumed in this section that the filtration cycles built up non-removable layers (referred to as bulges) as well as suspended particles in the capillary. To clarify the behaviour of suspended particles in the presence of non-backwashable layers, the distribution of backwashable particles exhibiting mechanical forces due to the backwash is investigated.

At the beginning of the simulation, the removable particles are deposited on the membrane with a packing density of 0.5 and thickness of 125 μm, whereas the non-backwashable particles or layers form distortions along the pathway of the suspended particles in different positions, as illustrated in Fig. 3.5. The particle distribution over section I (Fig. 3.5) is shown in Fig. 4.50. The distribution of particles inside the capillary depends on many factors which concern the particle characteristics (particle size) and flow properties (flow rate). The axial velocity of the fluid varies slightly at different capillary lengths and constricted areas. In addition to a change in the velocity gradient, the sudden change in the flow due to the bulges causes the generation of vortices and recirculation areas behind the bulges. Particles are carried by the vortices towards the membrane directly behind the narrowing where they form particle enrichment areas. This accumulation of particles between the two lower bulges after 3.3 s seen in Fig. 4.50. If the adhesion force is very strong, the particles are likely to cling to the bulges, causing the build-up of agglomerates. Furthermore, continuously passing through these narrowings and the growth of agglomerates contributes to a high possibility of capillary clogging. Moreover, due to the high shear rate which arises on the upper bulge, particles are widely disseminated in the region around the upper bulge, which causing a critical increase in the volume fraction of the particles up to 0.5 after 1.5 s, as shown in Fig. 4.50. This distribution again means potential formation of plugs inside the capillary. The regions of high particle concentration can change location according to the strength of both the shear stress and the vortices.

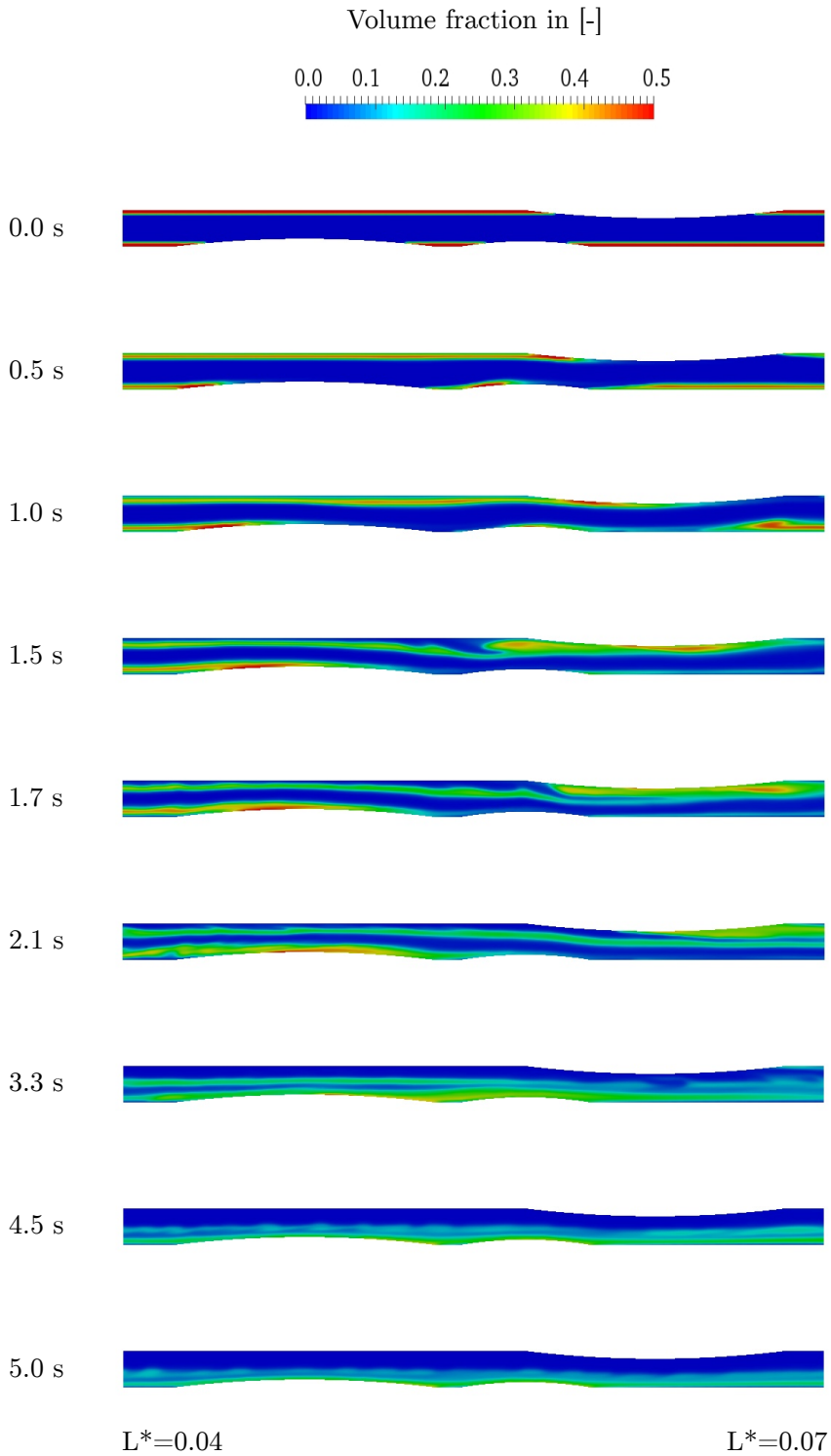

Figure 4.50: Particle volume fraction along section I of the capillary with the presence of non-backwashable particles adhered on the membrane during the backwash process operated at 2 *bar* pressure.

When the flow rate increases, the dissemination of the particles is constricted in the lower as well as the upper part of the capillary. This behaviour is seen in Fig. 4.51, which was taken in section II, illustrated in Fig. 3.5, during the backwash process with the presence of non-backwashable layers. Particles accumulate behind and on the surface of the bulges as these bulges are impermeable and the effects of the vortex behind them become more significant, as shown in Fig. 4.51 after 1 s. At the same time, the particles are lifted due to the fluid entering the capillary and flushed out of the capillary due to axial fluid velocity. This motion reduces the volume fraction of the particles in the accumulation regions. Furthermore, the particles settle in to the lower half of the capillary due to the gravitational effect. Thus, the particles accumulate in the lower half of the capillary, especially in the recirculation areas and on the impermeable sections of the membrane.

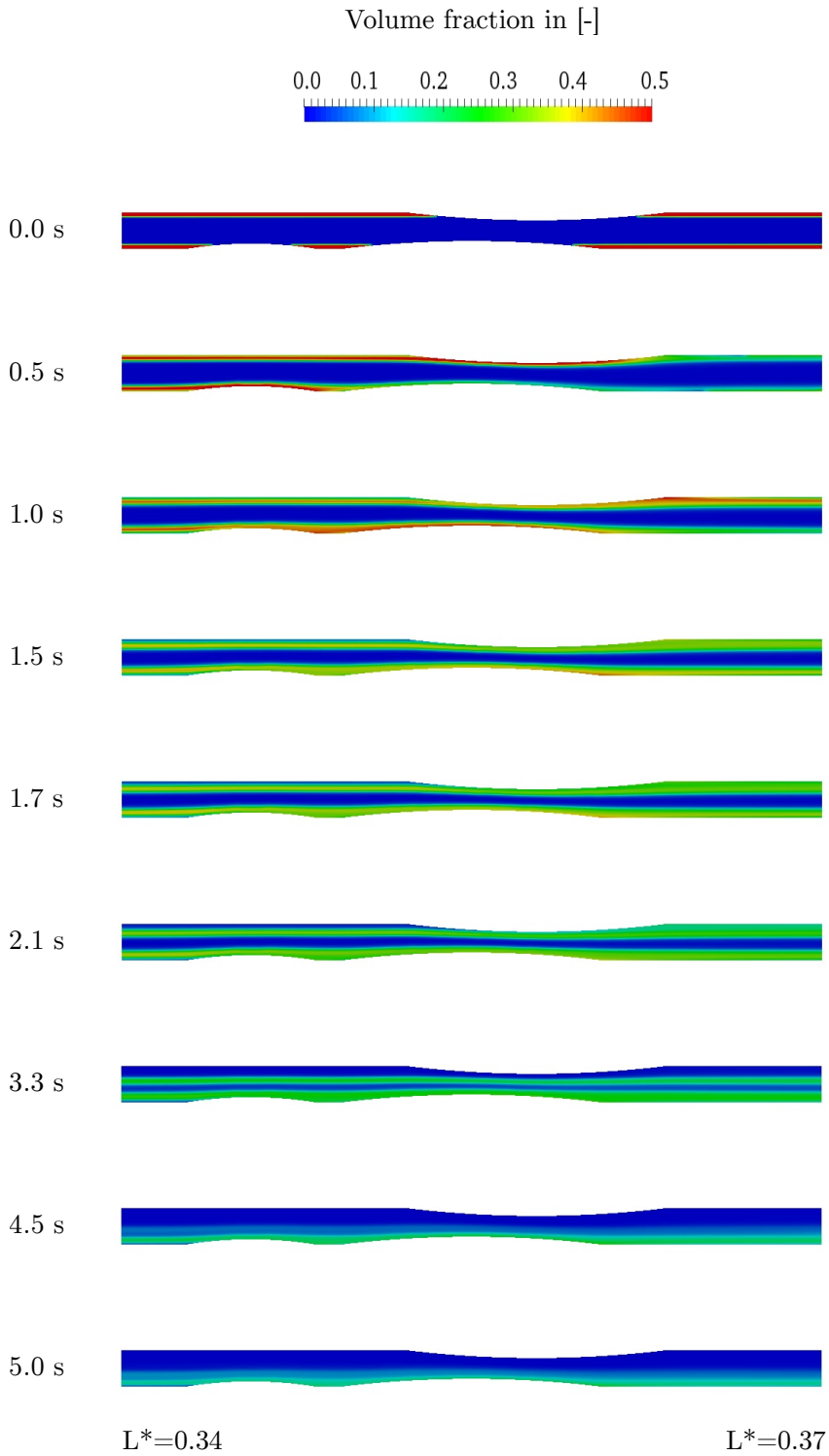

Figure 4.51: Particle volume fraction along section II of the capillary with the presence of non-backwashable particles adhered on the membrane during the backwash process operated at 2 *bar* pressure.

Comparing the removal of particles from the capillary when it contains only removable particles and when there are non-removable layers as well shows that the difference is negligible, as it accounts for 2 % of the initial volume fraction, as shown in Fig. 4.52. This refers to the fact that the presence of the non-removable layers does not hinder the removal of the suspended particles, rather it influences significantly the particle distribution inside the capillary during the backwash process.

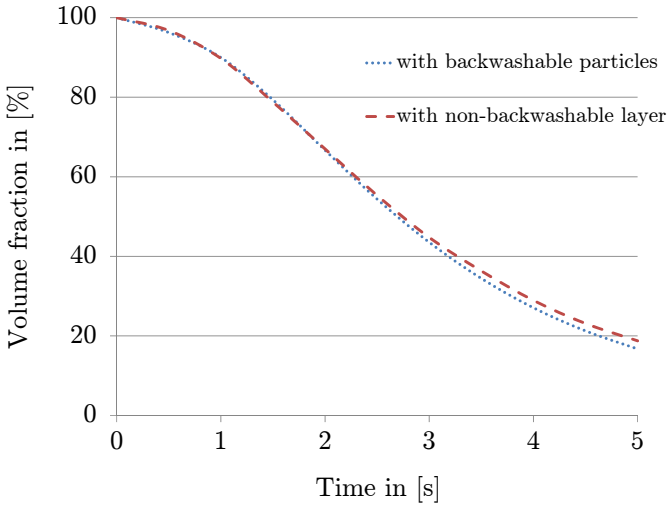

Figure 4.52: Comparison of particle removal under the same operating condition when the capillary contains only backwashable particles and when there are non-backwashable layers as well as backwashable particles.

4.6.6 Vertical configuration of the capillary

As the filtration as well as the backwash processes is found in a vertical positions and horizontal, the capillary in this section is vertically configured and the flow in the backwash process moves upwards. This calculation is performed under the assumption that the vertical configuration of the capillary allows also a constant inlet velocity over the capillary length. The assumption is not completely accurate, however its purpose is the investigation of the secondary flow inside the capillary. Hereby, the backwash process is carried out with particles which are initially evenly deposited, with a thickness of 125 μm,

particle diameter of 10 μm and an operating pressure of 2 bar. The schematic of the capillary is illustrated in Fig. 4.53.

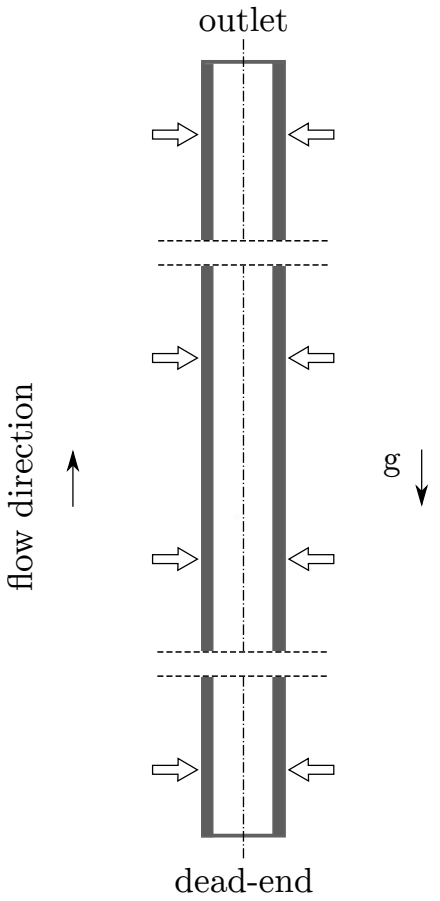

Figure 4.53: Vertical configuration of the capillary with even particle distribution. The flow in the backwash process is in the opposite direction to gravity (upward).

As expected, secondary flow does not appear since the distribution of the particles is symmetrical to the capillary axis over the simulation time. The resistance caused by the particles in the entire cross-section is symmetrical to the axis because the gravitational effect works in the opposite direction to that of the flow and does not contribute to asymmetrical particle distribution around the axis. The radial velocity as well as the particle distribution after 0.5 and 5 s is depicted in Fig. 4.54. It shows that the radial velocity is directed towards the capillary axis, driving the particles in the same direction. The fluid axial

velocity transports the particles towards the outlet, causing a reduction in the volume fraction of particles. This behaviour of the particles does not enhance the formation of accumulation areas inside the capillary during the backwash process. Therefore, the probability of capillary clogging occurring due to the development of particle enrichment areas is relatively small.

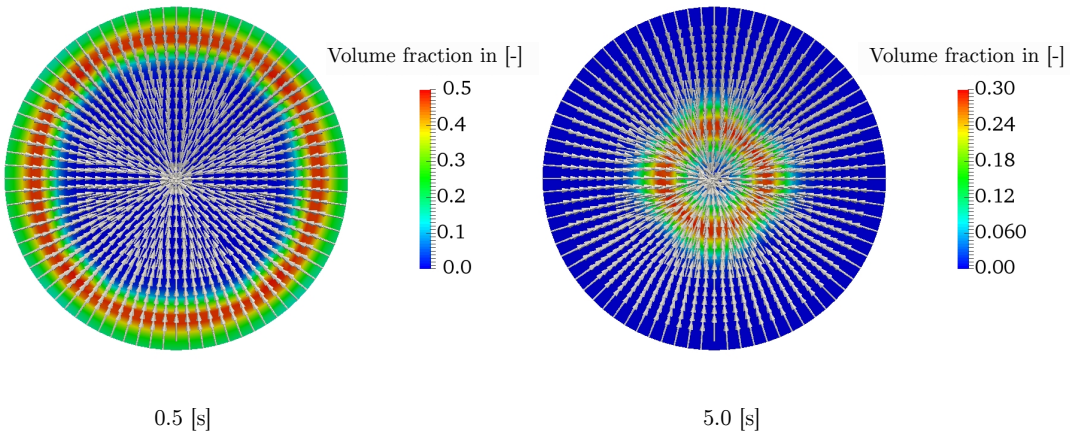

Figure 4.54: Vector plot of radial velocity and volume fraction in cross-section placed at control line A for operating pressure of 2 *bar* and particle diameter of 10 μm. The plot is taken after 0.5 and 5 s when the capillary is in vertical configuration.

However, changing the configuration of the capillary from horizontal to vertical has minimum effects on the removal of the particles. Fig. 4.55 shows that the remaining particles after 5 s backwashing for both capillary configurations represent about 16 % of the initial particle volume. That means the configuration of the capillary influences to a large extent the particle distribution inside the capillary, and less so the particle removal.

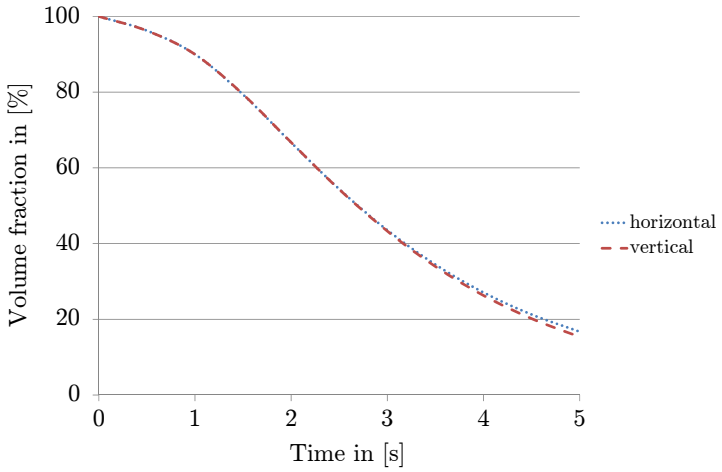

Figure 4.55: Comparison of particle removal under the same operating conditions when the capillary is placed vertically and horizontally.

Fig. 4.56 shows the pressure distribution evaluated at the capillary axis over the capillary length. It appears that the pressure drop increases compared to that for the horizontal capillary. This increases more than doubles at the beginning of the process and more than quadruples after 5 s of the simulation. The difference can be seen by comparing Figs. 4.56 and 4.39. This pressure difference between the two configurations is equal to the water column high which is transported upward.

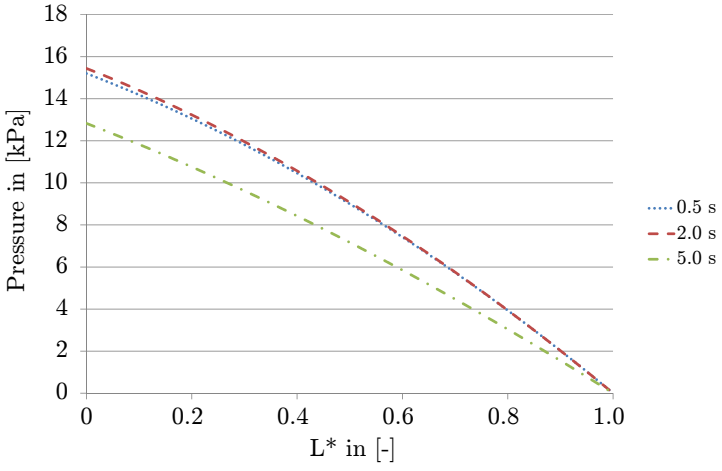

Figure 4.56: Pressure distribution in the capillary membrane placed vertically when particles are initially evenly deposited.

4.7 Uneven particle deposition

It is assumed that the filtration process finishes in uneven deposition of particles. The particles are deposited only on the lower part of the capillary with a height of 500 μm from the membrane surface and packing density of 0.5, as illustrated in Fig. 3.10. The upper part of the capillary is clean. Initially, particles with a diameter 10 μm occupy about 17 % of the total capillary volume. The portion of the particles in the capillary at the beginning is similar to that in the case of an evenly deposited layer. The capillary membrane is backwashed at an operating pressure of 2 bar. Similarly to the cases analysed above, the porous wall is not incorporated in the simulation, rather the operating pressure is converted to backwash flux which is calculated for the capillary with porous wall.

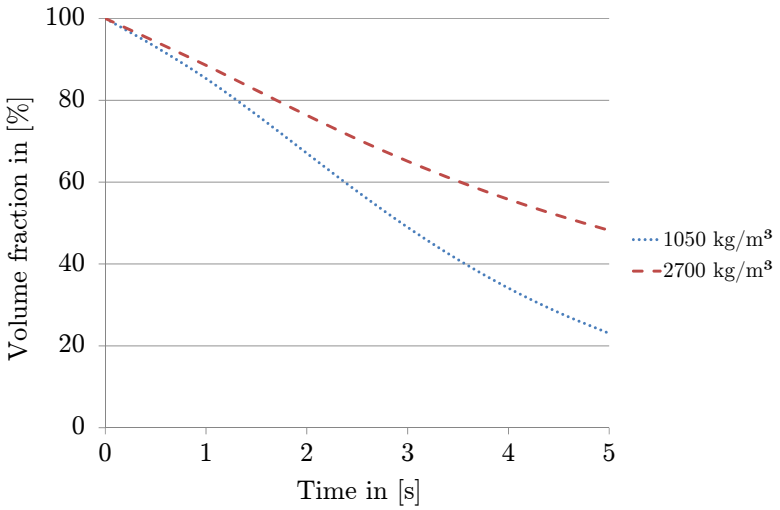

Figure 4.57: Recovery of the volume fraction of particles with diameter of 10 μm and different densities in percent at operating pressure of 2 bar.

The removal of particles with a different density from the capillary is illustrated in Fig. 4.57. Lighter particles (1050 kg/m^3) are transported faster than heavier particles (2700 kg/m^3), and thus they are flushed out of the capillary faster. The light particles remaining after 5 s of backwashing constitute about 23 % of the initial volume fraction whereas only half of the heavier particles left the

capillary over the same backwashing time. That means the backwashing time is relatively short for lighter particles compared with that of heavier particles. Estimating this time by following the tendency of the curves in Fig. 4.57, lighter particles require about 10 s to leave the capillary, whereas at least 13 s were needed to clean the capillary deposited with heavier particles. The estimated backwashing time is based on the assumptions made for this thesis.

Evaluating the velocity inside the capillary at control lines A, B and C shows shifted velocity profiles along the capillary length. If the capillary is empty of particles, a symmetrical velocity profile is expected. The asymmetrical nature of the velocity is reduced when the particle volume fraction in the accumulation regions decreases and the fluid velocity increases. This change can be seen in Fig. 4.58a after 5 s of backwashing at control lines B and C when a large portion of the deposited particles is removed. At control line A, the fluid flow has a low value which is not enough to overcome the resistance caused by the accumulated particles.

The volume fraction at control lines A, B and C is presented in Fig. 4.58b. It shows that the particles do not reach the upper half of the capillary during backwashing, rather they accumulate in the lower half of the capillary with a high volume fraction. Along the capillary, the particles are lifted up due to the entry of the fluid and a gap of clean fluid appears between the membrane and the accumulated particles. Then, some of the particles flow with the carrier fluid towards the outlet and the volume fraction of the particles on the control lines decreases. The predicted velocity at the control lines is in agreement with the particle distribution, i.e. the accumulation of the particles causes a reduction in the fluid velocity and even deviates the velocity profile from the symmetrical distribution. The accumulation of the particles and the shifted velocity profile increase the risk of capillary clogging occurring, especially when the axial velocity is very low. This is the case in the lower half of the capillary.

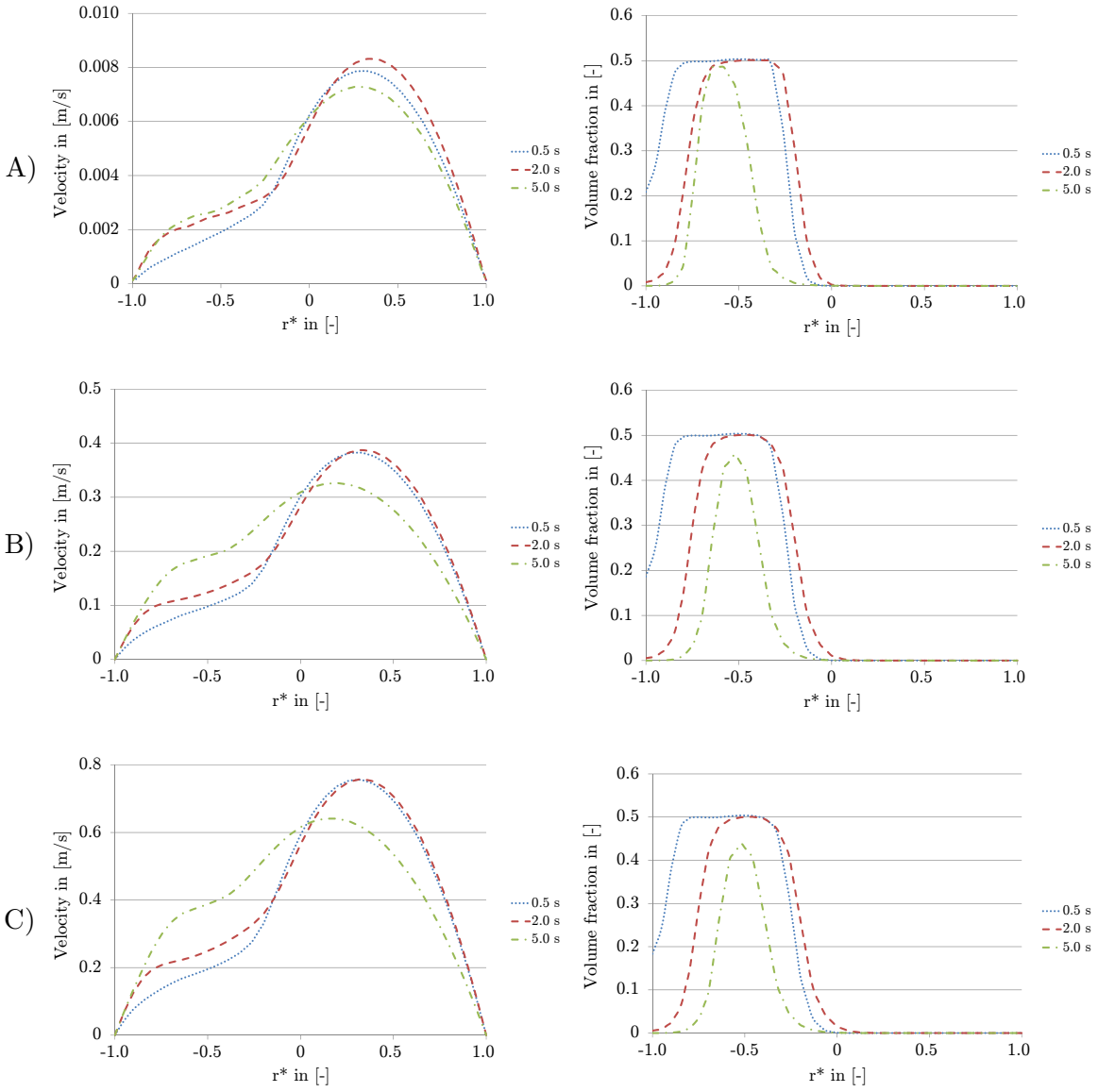

Figure 4.58: At control lines A, B and C a) the velocity distribution b) particle distribution for particles of diameter 2 μm and density 1050 kg/m^3 at 2 bar operating pressure over the backwashing time.

During the backwash process, a secondary flow is induced as the particles are heterogeneously distributed in the cross-section of the capillary. Fig. 4.59 shows the development of the secondary flow over the backwash time with particle

distribution in the background where a mutual relationship between them originates. At the beginning of the process, particles are deposited on the lower part of the capillary and the fluid entering penetrates the deposited layer. Over time, the particles are lifted up and the low particle volume fraction gap appears. Part of the fluid entering the capillary penetrates the deposited particles and simultaneously contributes to a decrease in the particle volume fraction in this gab. A small part flows parallel to the circumference of the membrane with an upward flow whereas a downward flow is observed in the middle of the capillary in a vertical plane. Thus, the secondary flow appears, as seen after 1 s in Fig. 4.59. As the particle volume fraction in the gap decreases the resistance there falls accordingly, and since the flow rate of the fluid is constant, more fluid flows parallel to the circumference of the membrane instead of entering through the accumulated particles. The secondary flow thus becomes far more distinct. The development of this secondary flow after 2 s is shown in Fig. 4.59. Due to the recirculation zones in the capillary cross-section, the width of the deposited particles in a horizontal plane becomes smaller and the secondary flow stronger till the particles are completely flushed out of the capillary because of the axial fluid velocity. In Fig. 4.59 the recirculation zones after 5 s can also be clearly seen. Hence, the particle distribution induces the secondary flow which is later responsible for the distribution of particles inside the capillary.

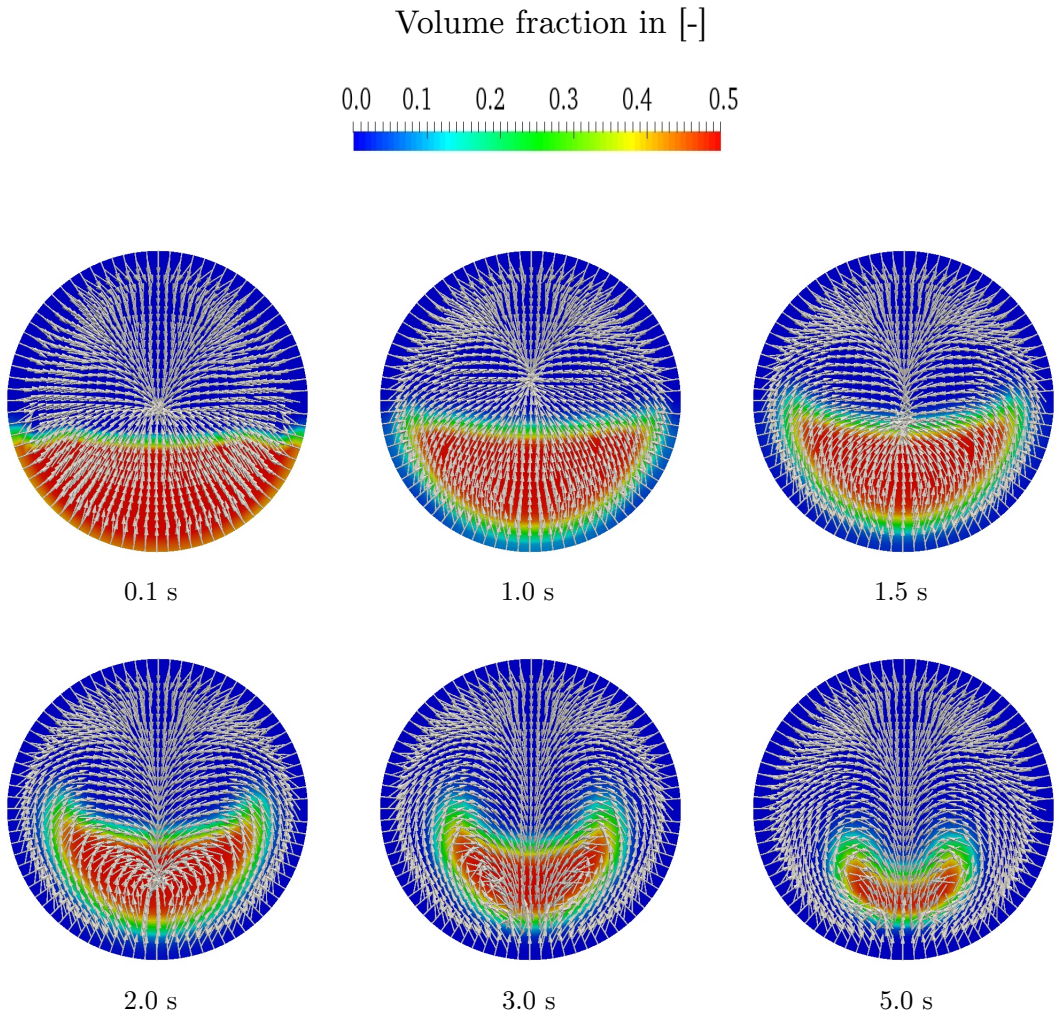

Figure 4.59: Vector plot of secondary flow and particle volume fraction over the simulation time for 2 *bar* operating pressure and particle size of 10 μm at a location on control line A.

4.8 Comparison of particle deposition

In this section, a comparison of backwash efficiency for deposited particles and homogeneously distributed ones is carried out. The backwash process is applied to the capillary with evenly and unevenly deposited particles on the membrane in addition to those homogeneously distributed in the capillary. The distribution is illustrated in Figs. 3.8, 3.10 and 3.7, respectively. In these cases,

the particles have a diameter of 10 μm and density of 1050 kg/m^3 and the process is operated at a pressure of 2 bar. The removal of the particles is shown in Fig. 4.60. Under the considered assumptions, it is obvious that if the particles are homogeneously distributed in the capillary, the backwash process will be much more effective. Conversely, for even and uneven particles deposition, removal requires either an extension of the backwash process or an increase in the operating pressure. However, uneven deposition requires the longest backwashing time. After a backwashing time of 5 s, the remaining particles when an even particles deposition is considered represent about 16 % and for uneven particle deposition is about 24 % whereas for homogeneous distribution it is the lowest of all (9 % of the initial total particle volume). This result is in agreement with the assumption made by Panglisch [13].

At the beginning of the backwash, the efficiency of the particle removal for evenly deposited particles is lower than for uneven deposition. However, after 2 s, the opposite is true. This can be ascribed to the fact that, at the beginning of the backwash, the particles are deposited evenly on the membrane and around the capillary axis where the axial velocity is at its maximum value the particle volume fraction is zero. Conversely, for the uneven deposition, at the beginning particles are closer to the axis and are transported by the axial fluid velocity towards the outlet. Due to the secondary flow explained above, the particles in the upper part of the capillary move to the lower part passing through the region where a high fluid velocity flows, as shown in Fig. 4.38. This increases the removal of the particles and thereby backwash efficiency. For the uneven particle deposition, the secondary flow affects only those particles in the lower part of the capillary and particles do not reach the region of high velocity, as shown in Fig. 4.59.

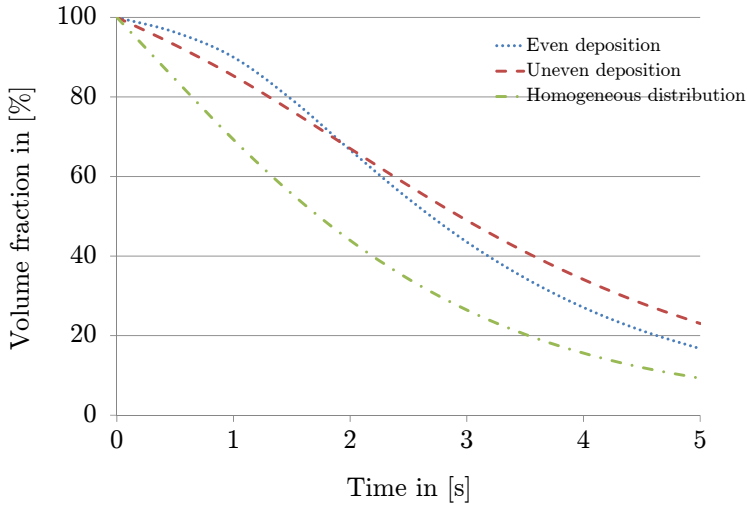

Figure 4.60: Recovery of the volume fraction of particles evenly and unevenly deposited on the membrane and homogeneously distributed in the capillary in percent. The particles have a diameter of 10 μm and density of 1050 kg/m^3 and are at an operating pressure of 2 bar.

The pressure drop will vary according to the particle density. Fig. 4.61 is a comparison of the pressure drop for two different particle densities. For both densities, the pressure drop increases in the capillary over time and reaches a maximum value after 1.3 s. However, this value is higher for heavy particles. At this point the particles are carried from the membrane surface towards the capillary centre. After this, the pressure drop slowly begins to decrease as the volume fraction inside the capillary decreases.

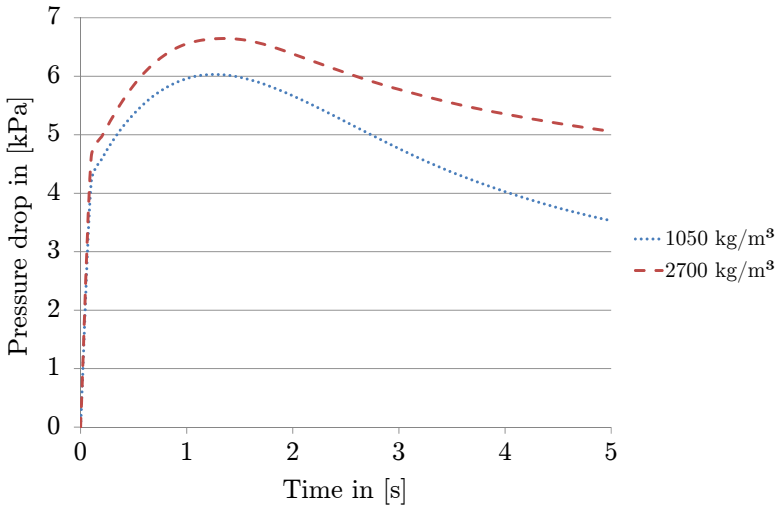

Figure 4.61: Pressure drop in the capillary for different particle densities. The particles have a diameter of 10 μm and the backwash process is operated at a pressure of 2 bar.

4.9 Consideration of polydisperse particles

The multiphase flow of particles of different sizes is considered. The initial volume fraction of the particles is 0.1 and they are homogeneously distributed inside the capillary at the beginning of the backwash process, which is operated at 2 bar operating pressure. The particles undergo virtual mass, lift and drag force.

4.9.1 Polydisperse particles without including aggregation and breakage

In this section, the particles are transported by the fluid towards the outlet without undergoing aggregation and breakage. The properties of the particles are detailed in Table. 3.2. The removal of the particles is discussed above when two-phase simulations are carried out. Thus, this section focuses on the particle distribution inside the capillary during the backwash process, which is observed at control lines A, B and C.

The velocity distribution plotted in Fig. 4.62a shows the fluid velocity at different locations in the capillary. The maximum fluid velocity increases towards the outlet as the flow rate increases over the capillary length. Furthermore, the velocity profiles are asymmetrical, especially after 5 s of the simulation when the particles are accumulated in the lower part of the capillary.

The behaviour of polydisperse particles is similar to that of each particle size separately. Fig. 4.62b shows the distribution of the fluid at control lines A, B and C. It shows particle enrichment areas in the lower half of the capillary. This can be seen by the low volume fraction of the fluid over the control lines since the sum of the simulated phases in a control volume must be equal to unity. The development of the particle accumulation areas can be ascribed to the appearance of the secondary flow in the cross-section of the capillary which is in turn caused by the asymmetrical particle distribution around the capillary axis. These particle enrichment areas, which consist of particles of different sizes and origins increases the probability of plugs forming and consequently clogging the capillary and stopping the process.

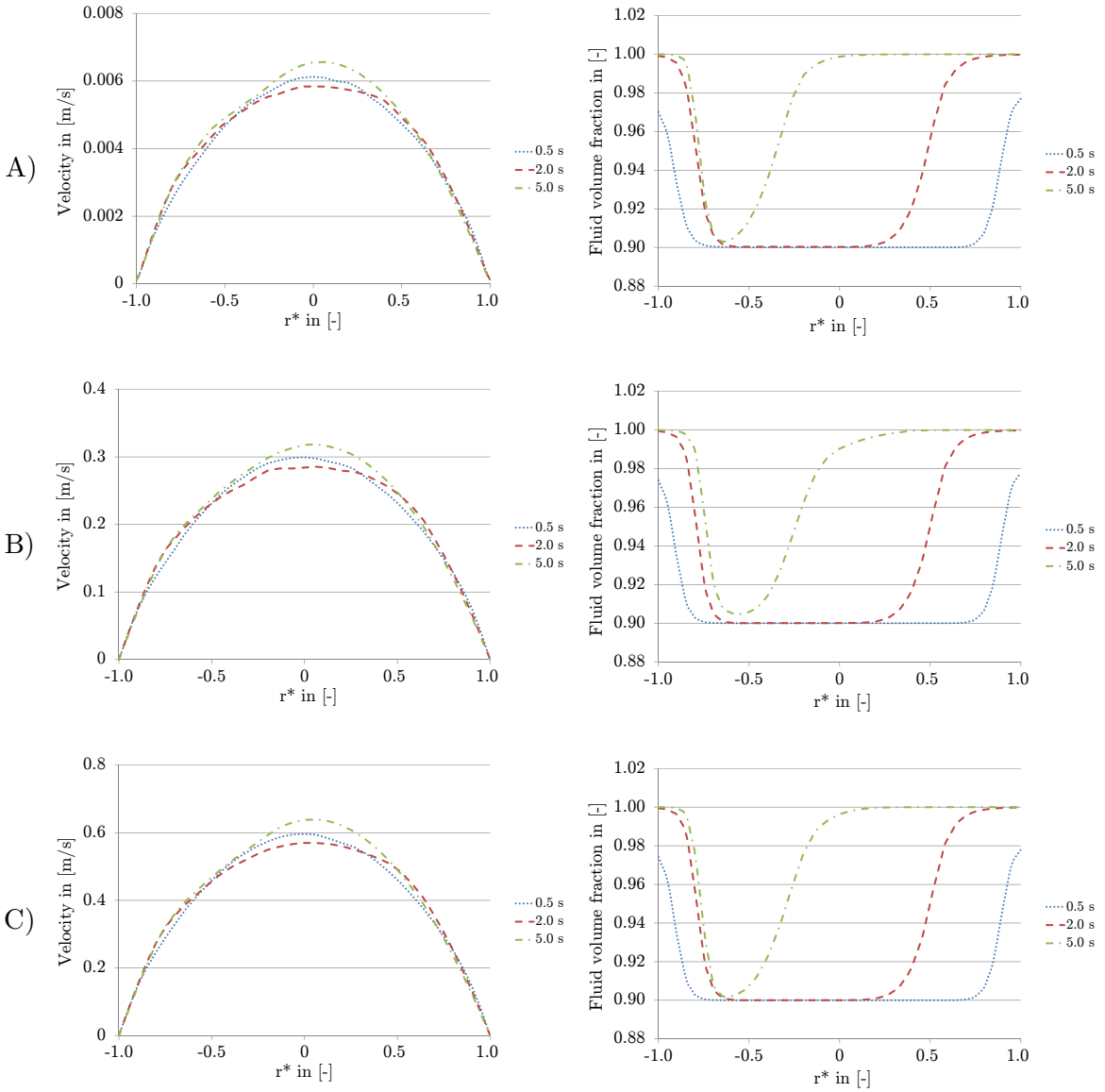

Figure 4.62: At control lines A, B and C a) the velocity distribution b) the fluid volume fraction when considering polydisperse particles at 2 *bar* operating pressure over the backwashing time and without including aggregation and breakage models.

4.9.2 Polydisperse particles with including aggregation and breakage

The agglomeration and breakup of the particles is included. This can be achieved by incorporating the population balance equation in the calculation. The prediction of potential agglomerates inside the capillary during the backwash process is achieved by considering a constant volume fraction of particles, which is maintained over the simulation. During this motion, the particles are observed at control lines A, B and C. The properties of the initial particles are detailed in Table 3.3.

In Fig. 4.63, the particle distribution of phase 1 and its characteristic diameter are illustrated. It can be seen that the particle distribution for phase 1 is similar over the three control lines. It shows the same trend, independent of the flow velocity. At the beginning and after 0.5 s of the simulation, the particles are still homogeneously distributed over the capillary cross-section. During the simulation, the volume fraction of phase 1 decreases in the capillary centre and especially in the lower half of the capillary near the membrane. Furthermore, Fig. 4.63a shows the predicted diameter of the particles over control lines A, B and C. It is noticeable that the particles agglomerate over the capillary length during the simulation time. Their diameter in phase 1 reaches about 11 μm near the membrane in the lower part after 5 s. Thus, the increase in diameter in phase 1 is 4 μm within 5 s from initial value of 7 μm.

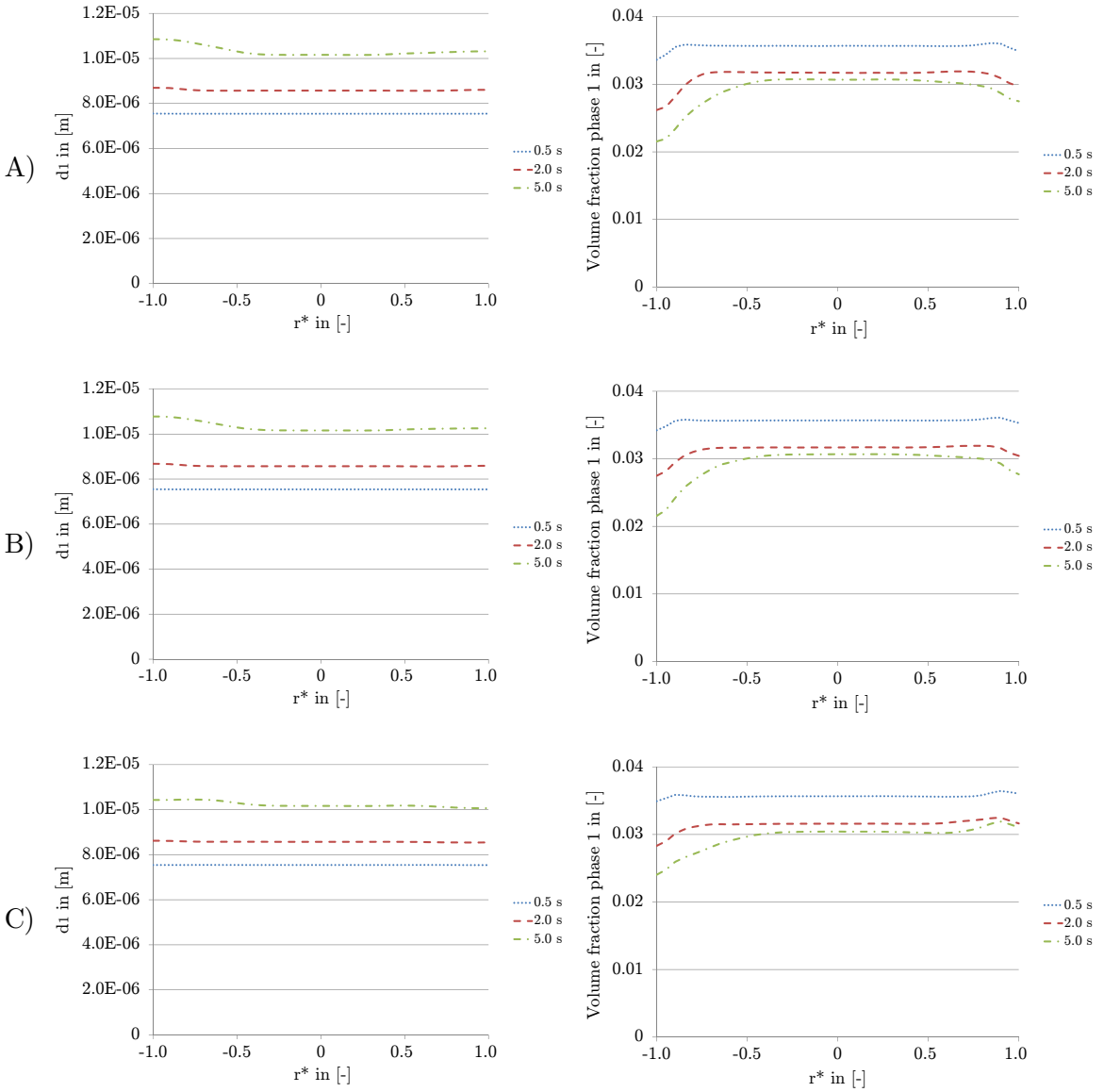

Figure 4.63: At control lines A, B and C a) the characteristic diameter distribution and b) volume fraction of phase 1 when considering polydisperse particles at 2 *bar* operating pressure over the backwashing time and including aggregation and breakage models.

In phase 2 the particles also display a higher volume fraction in the lower half of the capillary near the membrane. Generally, particles of phase 2 are homogeneously distributed in the membrane, as seen in Fig. 4.64b. Similarly, the diameter of phase 2 increases continuously during the simulation time over the capillary length due to agglomeration. This increase is about 7 μm from the initial diameter, as shown in Fig. 4.64a.

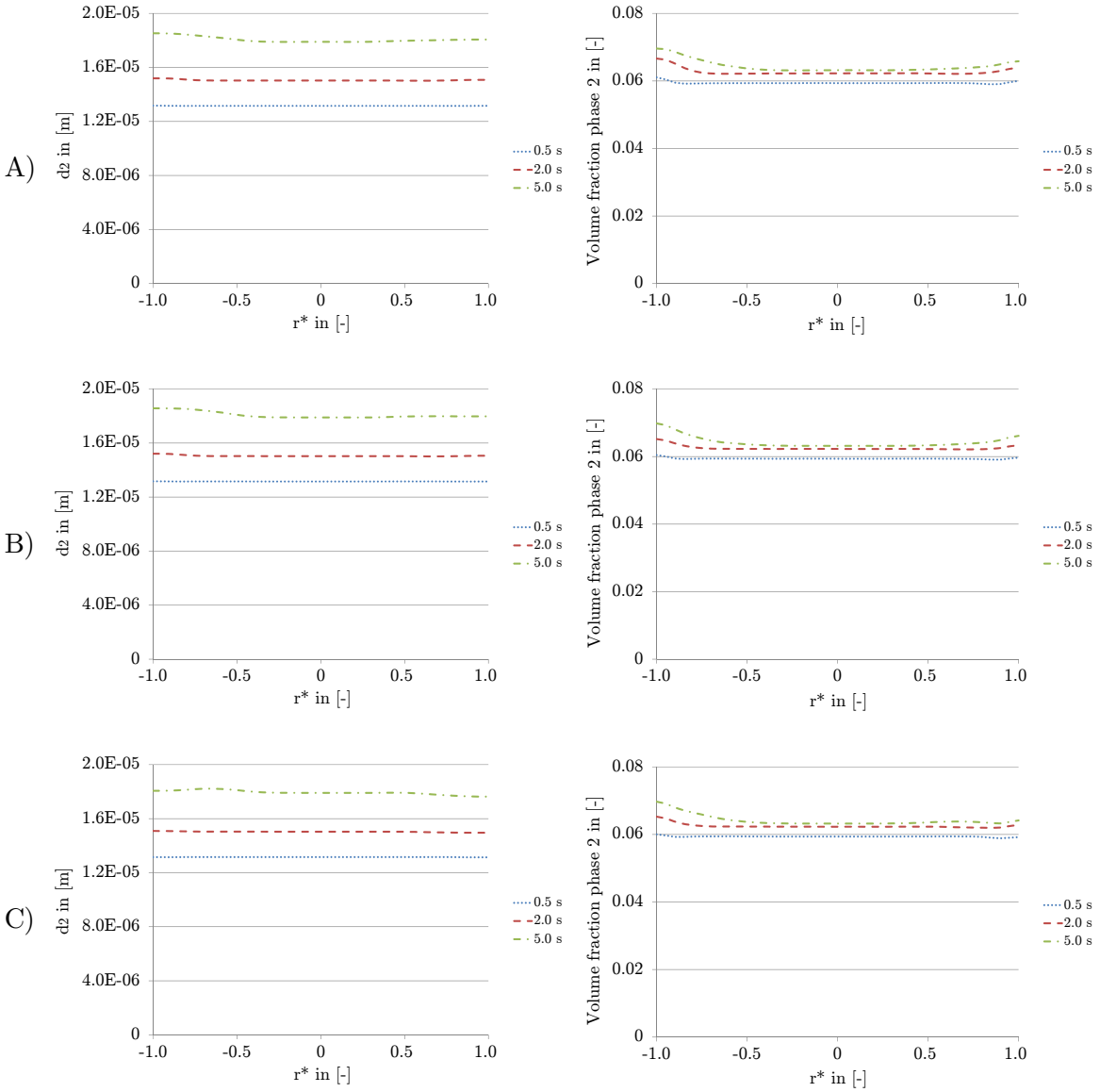

Figure 4.64: At control lines A, B and C a) the characteristic diameter distribution and b) volume fraction of phase 2 when considering polydisperse particles at 2 *bar* operating pressure over the backwashing time and including aggregation and breakage models.

The particles of phase 3 behave in a very similar way to those of phase 2. Their volume fraction increases in the lower part of the capillary. Furthermore, a small increase in volume fraction is observed in the upper part of the capillary. Their behaviour of phase 3 is plotted in Fig. 4.65b. The particle diameter increases after 5 s of the simulation to double the initial value of phase 3. The initial diameter is 17 μm and after 5 s becomes 25 μm over control lines A, B and C, as seen in Fig. 4.65a.

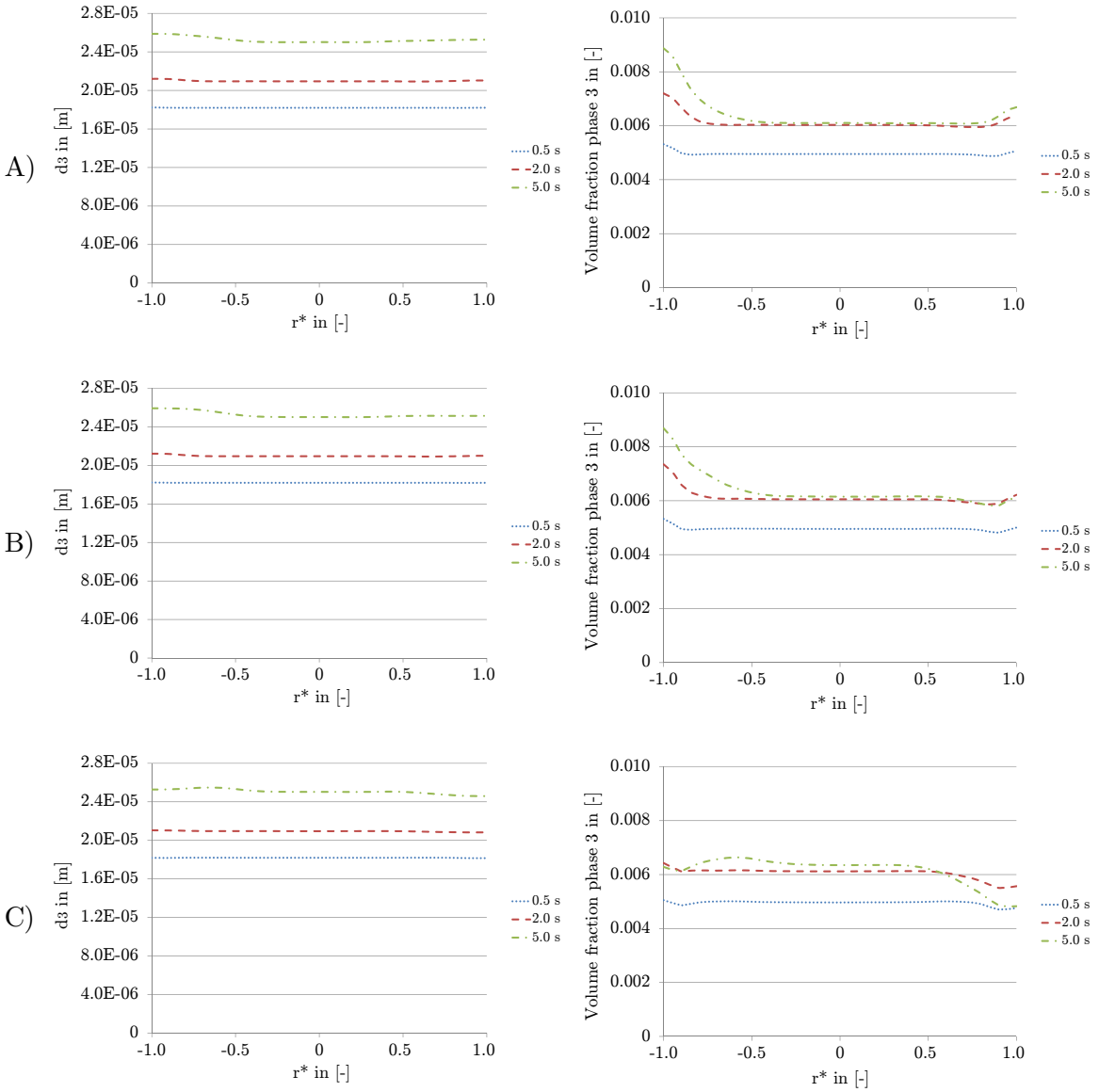

Figure 4.65: At control lines A, B and C a) the characteristic diameter distribution and b) volume fraction of phase 3 when considering polydisperse particles at 2 *bar* operating pressure over the backwashing time and including aggregation and breakage models.

No particle enrichment areas caused by phase 1, 2 or 3 are observed in the capillary for the studied boundary condition. Furthermore, the distribution of the particle diameter depends on the residence time of the disperses phases.

4.10 Conclusion for multiphase flow

The numerical simulations carried out in this chapter consider the multiphase flow inside a single capillary. Three initial particle distributions are taken into account. Two of these are a theoretical distribution which may appear partly in the capillary to be backwashed, and the other is a result of a filtration process performed experimentally. In particular, the theoretical distributions are used to investigate the influence of inhomogeneous distribution of fouling layers in the capillary on the backwash process from a fluid dynamics point of view. Furthermore, under the considered assumptions, particle behaviour as well as the recovery of the particles is investigated during the backwash for the three distributions. In all of these, particle enrichment areas are observed in the lower half of the capillary due to the gravity effect and the resulting downward movement of the particles. Since this study does not consider adhesion forces, it is assumed that these particle enrichment areas in the capillary lead to a high probability of capillary clogging as the particle concentration and packing density in these areas are high. Moreover, a secondary flow arises during backwashing when particle resistance changes over the cross-section, which significantly influences the particle distribution inside the capillary. The number of recirculation zones varies according to the properties of the particles. In other words, apart from properties of the particles, a secondary flow is induced when the particle distribution is not symmetrical around the capillary axis. However, evenly distributed particles are found to be slightly affected by the secondary flow whereas for the other distributions and after the same simulation time, the inhomogeneity in the capillary is enhanced under the accepted considerations in this thesis.

The vertical configuration of the capillary is part of the investigation. However, the assumption made for the simulation - that inward radial velocity is constant over the capillary length - is not fully compatible with this configuration. This is because the hydrostatic pressure has a non-negligible effect on the variation of radial velocity at the inlet on the porous wall, in contrast to horizontal capillary configuration where this variation is neglected. Nevertheless, this calculation

emphasises that gravity has a significant influence on both inhomogeneous particle distribution and induction of secondary flow.

The influence of the bulges on particle distribution is also investigated. These bulges create recirculation zones behind them where the particles are entrapped, and particle enrichment areas develop. These particle enrichment areas increase the probability of agglomerates forming if the adhesion forces (which vary hugely among the particle materials) are strong enough. Furthermore, these bulges enhance the inhomogeneity of the particle distribution inside the membrane over the backwash process. Thus, the developed model predicts the likely particle distribution in the capillary with the existence of non-backwashable particles under the considered assumptions.

During the backwash process the particles in the capillary undergo aggregation and breakage. This involves the evaluation of particle diameter over the backwashing time. As the focus of the investigation is on potential capillary plugging, the aggregation process in the model is adjusted to be dominant. This is why particle diameter rapidly increases once the simulation starts. The assumption of the particles' constant volume fraction over the simulation contrasts with reality. However, it is used to describe the evolution of aggregates when the volume fraction of the particles is at its maximum value. This high volume fraction increases the frequency of particle collision and thus the possible formation of plugs.

Chapter 5

Summery

The application of membrane filtration with Inside-Out Dead-End driven UF-/ MF- capillary membranes in water treatment has exponentially risen and has been receiving increasing attention due to technical, economic and ecological reasons. However, this technology is exposed to fouling which is the main constraint of capillary membrane. It affects the porosity of the membrane and subsequently diminishes the performance of the filtration process and increases the operational costs. Therefore, the membrane has to be backwashed. The required backwash process has high potential to enhance the efficiency of the filtration process and minimise irreversible membrane fouling. It is a determining factor in ensuring an effective filtration process and enhancing the separation of particles in the capillary membrane. This process encounters a number of complicated hydrodynamic phenomena which affects particle removal and accumulation inside the capillary membrane. To increase understanding of the backwash process and optimise the operating parameters, improved fundamental comprehension of the mechanisms which influence the detachment and transport of particles and fouling layers from inside-out dead-end driven capillary membranes is necessary. For this purpose, a numerical model of the process was developed and a set of operating parameters was investigated for both mono- and polydisperse particles. This work covers a wide range of the parameters associated with the backwash process, such as operating pressure, particle size and density, and initial particle distribution. All these variables contribute to the development of an optimised backwash, and can thus lead to

significant reduction in operating costs.

For the horizontal configuration of the capillary, it was found that converting the operating pressure into a constant flux over the capillary length is an acceptable approach for the boundary condition. The water enters the capillary perpendicular to the capillary wall, independent of the conditions it encounters in the backwash, such as membrane permeability and operating pressure. Membrane permeability has an proportional relationship to the flux entering the porous wall, i.e. when the permeability of the membrane increases, the flow rate increases along the capillary and the pressure drop increases too. This permeability represents the packing density of the particles retained on the capillary surface. In addition, increasing the operating pressure leads to higher flux at the same membrane permeability. The pressure drop inside the capillary membrane increases with a rise in operating pressure and reaches its maximum value at the dead-end. Furthermore, the shear rate affecting both the membrane surface and the tightly adhered layers is estimated along the capillary and for different distributions of these layers.

Moreover, the recovery of the particles during the backwash process shows that for a constant backwashing time high operating pressure accelerates the flushing out of particles from the capillary. Furthermore, the results show that particle transport efficiency reduces when particle diameter increases. This means that particles with a small diameter are removed faster than larger particles. Likewise, varying the operating pressure during the backwash process positively effects the removal of the particles, especially when the duration of the high pressure phase is long, i.e. the longer the particles are under high pressure, the less remains of them. The influence of the particle density on the removal and distribution of the particles was investigated. Heavy particles show a significant delay in leaving the capillary compared with lighter particles with the same diameter and undergoing similar operating pressure. For the same operating conditions and after the same backwashing time, the portion of heavier particles remaining in the capillary is much higher than for lighter particles.

A secondary flow is induced inside the capillary during the removal of the particles. The origin of this flow is the heterogeneity of particle distribution over the capillary cross-section. The number of recirculation zones varies according to the density of the considered particles. Secondary flow is responsible for the distribution of the particles and enhances the heterogeneity of particle distribution inside the capillary. It determines the particles enrichment and accumulation areas as it drives the particles to the lower half of the capillary. At this region, the velocity of the fluid is relatively low and the particles tend to gather in critical accumulation areas during backwashing. Thus, the removal of the particles from that region becomes more difficult and can lead to capillary clogging. In terms of particle removal, the results obtained show a good agreement with the experimental data.

Moreover, the vertical placement of the capillary causes symmetrical particle distribution around the axis. This distribution prevents the development of the secondary flow and thus, the particles are transported towards the outlet without causing critical accumulation areas.

The irregular, deposit and non-backwashable particles on the suspended particle distribution shows a significant influence on the formation of accumulation areas during the backwash process. The removable particles are entrapped by the tightly deposited layer and cause critical values of particle volume fraction. If the entrapped particles encounter a high adhesive force, the tightly deposited layer will develop into a dense and impermeable layer which hinders water flowing to the capillary. In general, the remaining parts of the deposited particles enhance the formation of particle enrichment areas and prevent the suspended particles from leaving the capillary. Consequently, the process stops or becomes less efficient.

Considering the aggregation and breakage of the particles in the developed model, homogeneous particles and size distribution inside the capillary is shown. Accumulation areas inside the capillary are not observed. The particles agglomerate continuously during the simulation and along the capillary length.

The increase in particle diameter for large particles is more than for the small particles. The development of possible plugs begins from the suspended particles with a large diameter.

Chapter 6

Outlook

Most of the numerical analysis of multiphase flow in capillary membranes focuses on the filtration process. Nevertheless, the current study developed a numerical model for predicting particle behaviour in a single capillary membrane operated in dead-end mode during backwashing. The model simplified the upgrade towards a much more complicated numerical model in order to approach more realistic conditions for the backwash. Although the agglomeration and breakup of particles are covered in the current study, adhesion force is also of importance as it is a determining factor when it comes to the detachment mechanism.

The current study considered a single capillary from the bundle and disregarded the influence of different capillary arrangements in the module on the flow pattern. It is assumed that due to the small diameter of the capillaries forming the module and the high packing density as well as the inhomogeneities of the irreversible fouling in the plurality of communicating capillaries, the probability of plugging occurring is relatively high. In addition, the influence of other capillaries on the pressure distribution inside the module also plays significant role in the detachment of the particles and consequently on the particle distribution inside the capillary. Generating appropriate shear stress on the membrane surface by determining the velocity profile and the capillaries'

configuration will contribute to better control of fouling and enhance the backwash process.

Till now, most of the published researches concentrate on the design of the module in order to optimise the filtration operating conditions [116, 117, 118], or on membrane cleaning [119, 59, 120, 121, 122]. In spite of the significant influence of optimised backwashing on fouling and removal of particles, consideration of the backwash process has not been part of the manufacturing of the module. An improved module design which takes into account the optimal conditions for filtration as well as backwashing from a numerical point of view does not currently exist. A numerical model for the investigation of the backwash boundary condition in capillary module and the interaction of the phases in the module has not been developed and carried out. Furthermore, most models developed for studying the bundle are based on the assumption that the flow inside each capillary is identical, i.e. the whole bundle is substituted by a single capillary with the surrounding water and permeability equal to that of the bundle.

The main objective of the of further research could be optimising the backwash process in capillary membrane modules. The design of the modules with regard to both filtration and backwash processes will enhance the removal of particles, prevent the clogging of capillaries and extend the membrane lifetime. Optimising the pressure drop inside the module during backwashing will contribute to a fall in the water and energy consumption, and consequently, the operating costs. Furthermore, the investigation of secondary flow induced inside the capillaries in the module has significant influence on particle distribution and particle enrichment areas, which are potential positions of capillary clogging. The capillaries' arrangement in a module and the irregular entry of water into each membrane determines the behaviour of the particles inside the capillaries if this is accompanied by the development of secondary flow.

Based on the comprehensive knowledge gained from the present thesis and the available resources for high performance computing, a CFD model can be

developed for the purpose of optimising the backwash process in capillary modules. Simulations are necessary to understand the role of the module design, operating parameters and membrane characteristics on the removal of particles during backwash.

References

[1] R. Gimbel. Wassertechnik - ein Beitrag zur Loesung der Weltwasserkrise. DECHEMA Kolloquium in Frankfurt, 16. Juni 2010.

[2] S. Panglisch. *Zur Bildung und Vermeidung schwer entfernbarer Partikelablagerungen in Kapillarmembranen bei der Dead-End Filtration.* IWW, 2001.

[3] C. Charcosset. *Membrane Processes in Biotechnology and Pharmaceutics*, chapter Principles on membrane and membrane processes, pages 1–41. Elsevier, 1st edition, 2012.

[4] R.W. Baker. *Membrane Technology and Applications, 3rd Edition*, chapter Membranes and Modules, pages 89–160. John Wiley and Sons, Ltd, 2004.

[5] S.G.J. Heijman, M.D. Kennedy, and G.J. van Hek. Heterogeneous fouling in dead-end ultrafiltration. *Desalination*, 178(1-3):295–301, 2005.

[6] A.G. Fane, C.Y. Tang, and R. Wang. Membrane technology for water: Microfiltration, ultrafiltration, nanofiltration, and reverse osmosis. In P. Wilderer, editor, *Treatise on Water Science*, pages 301–335. Elsevier, 2nd edition, 2011.

[7] A.G. Fane, W. Xi, and W. Rong. Membrane filtration processes and fouling. In G. Newcombe and D. Dixon, editors, *Interface Science in Drinking Water Treatment Theory and Applications*, volume 10, pages 109–132. Elsevier, 1st edition, 2006.

[8] C. Charcosset. Membrane systems and technology. In M. Moo-Young, editor, *Comprehensive Biotechnology*, volume 2, pages 603–618. Academic Press, 2nd edition, 2011.

[9] W. Eykamp. Microfiltration and ultrafiltration. In R.D. Noble and S.A. Stern, editors, *Membrane Separations Technology Principles and Applications*, volume 2, pages 1–43. Elsevier, 1995.

[10] T. Melin and R. Rautenbach. *Membranverfahren: Grundlagen der Modul- und Anlagenauslegung*. VDI-Buch. Springer Berlin Heidelberg, 2007.

[11] L.J. Zeman. *Microfiltration and Ultrafiltration: Principles and Applications*. Taylor & Francis, 1996.

[12] S.G.J. Heijman, M. Vantieghem, S. Raktoe, J.Q.J.C. Verberk, and J.C. van Dijk. Blocking of capillaries as fouling mechanism for dead-end ultrafiltration. *Journal of Membrane Science*, 287(1):119–125, 2007.

[13] S. Panglisch. Formation and prevention of hardly removable particle layers in inside-out capillary membranes operating in dead-end mode. *Water Science and Technology: Water Supply*, pages 117–124, 2003.

[14] R. Gimbel and W. Kowalczyk. DFG Abschlussbericht, Analysis of fluid-dynamical and physico-chemical aspects of capillary membrane backwashing. 12.2010-09.2015, Projektnummer 179936688.

[15] A.G. Fane and C.J.D. Fell. A review of fouling and fouling control in ultrafiltration. *Desalination*, 62:117–136, 1987.

[16] R. Field. *Membrane Technology: Membranes for Water Treatment*, volume 4, chapter Fundamentals of Fouling, pages 1–23. Wiley-VCH Verlag GmbH and Co. KGaA, 2010.

[17] W. Guo, H.H. Ngo, and J. Li. A mini-review on membrane fouling. *Bioresource Technology*, 122:27–34, 2012.

[18] W. Gao, H. Liang, J. Ma, M. Han, Z.l. Chen, Z.S. Han, and G.B. Li. Membrane fouling control in ultrafiltration technology for drinking water production: A review. *Desalination*, 272(13):1–8, 2011.

[19] J. Mendret, C. Guigui, P. Schmitz, and C. Cabassud. In situ dynamic characterisation of fouling under different pressure conditions during dead-end filtration: Compressibility properties of particle cakes. *Journal of Membrane Science*, 333(12):20–29, 2009.

[20] H. Li, A.G. Fane, H.G.L. Coster, and S. Vigneswaran. Direct observation of particle deposition on the membrane surface during crossflow microfiltration. *Journal of Membrane Science*, 149(1):83–97, 1998.

[21] A.D. Marshall, P.A. Munro, and G. Traegaerdh. The effect of protein fouling in microfiltration and ultrafiltration on permeate flux, protein retention and selectivity: A literature review. *Desalination*, 91(1):65–108, 1993.

[22] G.F. Crozes, J.G. Jacangelo, C. Anselme, and J.M. Laine. Impact of ultrafiltration operating conditions on membrane irreversible fouling. *Journal of Membrane Science*, 124(1):63–76, 1997.

[23] M.C. Vincent-Vela, B. Cuartas-Uribe, S. Alvarez-Blanco, and J. Lora-Garcia. Analysis of an ultrafiltration model: Influence of operational conditions. *Desalination*, 284:14–21, 2012.

[24] L. Wang, X. Wang, and K.I. Fukushi. Effects of operational conditions on ultrafiltration membrane fouling. *Desalination*, 229(13):181–191, 2008.

[25] M. Zhang and L. Song. Mechanisms and parameters affecting flux decline in cross-flow microfiltration and ultrafiltration of colloids. *Environmental Science & Technology*, 34(17):3767–3773, 2000.

[26] S. Shirazi, C.J. Lin, and D. Chen. Inorganic fouling of pressure-driven membrane processes - a critical review. *Desalination*, 250(1):236–248, 2010.

[27] H. Nakajima. *Mass Transfer-Advances in Sustainable Energy and Environment Oriented Numerical Modeling*. InTech, 2013. ISBN: 9789535111702.

[28] J. Kim and F.A. DiGiano. Fouling models for low-pressure membrane systems. *Separation and Purification Technology*, 68(3):293–304, 2009.

[29] T. Ando, K. Akamatsu, S.I. Nakao, and M. Fujita. Simulation of fouling and backwash dynamics in dead-end microfiltration: Effect of pore size. *Journal of Membrane Science*, 392-393:48–57, 2012.

[30] S. Panglisch and R. Gimbel. Formation of layers of non-brownian particles in capillary membranes operated in dead-end mode. *Journal of the Chinese Institute of Chemical Engineers*, 35:77–85, 2004.

[31] K. Hwang and Y. Wang. Numerical simulation of particles deposition in cross-flow microfiltration of binary particles. *Tamkang Journal of Science and Engineering*, 2(4):119–125, 2001.

[32] L.F. Fu and B.A. Dempsey. Modeling the effect of particle size and charge on the structure of the filter cake in ultrafiltration. *Journal of Membrane Science*, 149(2):221–240, 1998.

[33] S.H. Yoon, C.H. Lee, K.J. Kim, and A.G. Fane. Three-dimensional simulation of the deposition of multi-dispersed charged particles and prediction of resulting flux during cross-flow microfiltration. *Journal of Membrane Science*, 161(1-2):7–20, 1999.

[34] J. Altmann and S. Ripperger. Particle deposition and layer formation at the crossflow microfiltration. *Journal of Membrane Science*, 124(1):119–128, 1997.

[35] A. Broeckmann, J. Busch, T. Wintgens, and W. Marquardt. Modeling of pore blocking and cake layer formation in membrane filtration for wastewater treatment. *Desalination*, 189(1-3):97–109, 2006.

[36] M.C. Porter. Concentration polarization with membrane ultrafiltration. *Industrial & Engineering Chemistry Product Research and Development*, 11(3):234–248, 1972.

[37] C.C. Ho and A.L. Zydney. A combined pore blockage and cake filtration model for protein fouling during microfiltration. *Journal of Colloid and Interface Science*, 232(2):389–399, 2000.

[38] C. Duclos-Orsello, W. Li, and C.C. Ho. A three mechanism model to describe fouling of microfiltration membranes. *Journal of Membrane Science*, 280(1-2):856–866, 2006.

[39] W. Yuan, A. Kocic, and A.L. Zydney. Analysis of humic acid fouling during microfiltration using a pore blockagecake filtration model. *Journal of Membrane Science*, 198(1):51–62, 2002.

[40] K. Katsoufidou, S.G. Yiantsios, and A.J. Karabelas. A study of ultrafiltration membrane fouling by humic acids and flux recovery by backwashing: Experiments and modeling. *Journal of Membrane Science*, 266(1-2):40–50, 2005.

[41] A.A. Makardij, M.M. Farid, and X.D. Chen. A simple and effective model for cross-flow microfiltration and ultrafiltration. *The Canadian Journal of Chemical Engineering*, 80(1):28–36, 2002.

[42] R. Ghidossi, D. Veyret, and P. Moulin. Computational fluid dynamics applied to membranes: State of the art and opportunities. *Chemical Engineering and Processing: Process Intensification*, 45(6):437–454, 2006.

[43] G. Keir and V. Jegatheesan. A review of computational fluid dynamics applications in pressure-driven membrane filtration. *Reviews in Environmental Science and Bio/Technology*, 13(2):183–201, 2014.

[44] Y. Bessiere, D.F. Fletcher, and P. Bacchin. Numerical simulation of colloid dead-end filtration: Effect of membrane characteristics and operating conditions on matter accumulation. *Journal of Membrane Science*, 313(1-2):52–59, 2008.

[45] P. Bacchin, B. Espinasse, Y. Bessiere, D.F. Fletcher, and P. Aimar. Numerical simulation of colloidal dispersion filtration: description of critical flux

and comparison with experimental results. *Desalination*, 192(1-3):74–81, 2006.

[46] K.J. Lee and R.M. Wu. Simulation of resistance of cross-flow microfiltration and force analysis on membrane surface. *Desalination*, 233(1-3):239–246, 2008.

[47] M. Rahimi, S.S. Madaeni, and K. Abbasi. CFD modeling of permeate flux in cross-flow microfiltration membrane. *Journal of Membrane Science*, 255(12):23–31, 2005.

[48] A. Lerch. Fouling layer formation by flocs in inside-out driven, horizontal aligned capillary ultrafiltration membranes. *Desalination*, 283:131–139, 2011.

[49] J. Bridgeman, B. Jefferson, and S.A. Parsons. The development and application of CFD models for water treatment flocculators. *Advances in Engineering Software*, 41(1):99–109, 2010.

[50] Z. Do-Quang, A. Cockx, A. Liné, and M. Roustan. Computational fluid dynamics applied to water and wastewater treatment facility modeling. *Environmental Engineering and Policy*, 1(3):137–147, 1998.

[51] X. Shi, G. Tal, N.P. Hankins, and V. Gitis. Fouling and cleaning of ultrafiltration membranes: A review. *Journal of Water Process Engineering*, 1:121–138, 2014.

[52] K.N. Bourgeous, J.L. Darby, and G. Tchobanoglous. Ultrafiltration of wastewater: effects of particles, mode of operation, and backwash effectiveness. *Water Research*, 35(1):77–90, 2001.

[53] P.J. Remize, C. Guigui, and C. Cabassud. Evaluation of backwash efficiency, definition of remaining fouling and characterisation of its contribution in irreversible fouling: Case of drinking water production by air-assisted ultrafiltration. *Journal of Membrane Science*, 355(1-2):104–111, 2010.

[54] W.J.C. van de Ven, I.G.M. Puent, A. Zwijnenburg, A.J.B. Kemperman, W.G.J. van der Meer, and M. Wessling. Hollow fiber ultrafiltration: The concept of partial backwashing. *Journal of Membrane Science*, 320(1-2):319–324, 2008.

[55] K. Katsoufidou, S.G. Yiantsios, and A.J. Karabelas. An experimental study of uf membrane fouling by humic acid and sodium alginate solutions: the effect of backwashing on flux recovery. *Desalination*, 220(1-3):214–227, 2008.

[56] P. Hillis, M.B. Padley, N.I. Powell, and P.M. Gallagher. Effects of backwash conditions on out-to-in membrane microfiltration. *Desalination*, 118(1-3):197–204, 1998.

[57] J.P. Chen, S.L. Kim, and Y.P. Ting. Optimization of membrane physical and chemical cleaning by a statistically designed approach. *Journal of Membrane Science*, 219(1-2):27–45, 2003.

[58] N.G. Cogan and S. Chellam. A method for determining the optimal backwashing frequency and duration for dead-end microfiltration. *Journal of Membrane Science*, 469:410–417, 2014.

[59] H. Chang, H. Liang, F. Qu, S. Shao, H. Yu, B. Liu, W. Gao, and G. Li. Role of backwash water composition in alleviating ultrafiltration membrane fouling by sodium alginate and the effectiveness of salt backwashing. *Journal of Membrane Science*, 499:429–441, 2016.

[60] H. Chang, F. Qu, B. Liu, H. Yu, K. Li, S. Shao, G. Li, and H. Liang. Hydraulic irreversibility of ultrafiltration membrane fouling by humic acid: Effects of membrane properties and backwash water composition. *Journal of Membrane Science*, 493:723–733, 2015.

[61] S. Li, S.G.J. Heijman, J.Q.J.C. Verberk, A.R.D. Verliefde, A.J.B. Kemperman, J.C. van Dijk, and G. Amy. Impact of backwash water composition on ultrafiltration fouling control. *Journal of Membrane Science*, 344(1-2):17–25, 2009.

[62] S. Li, S.G.J. Heijman, J.Q.J.C. Verberk, A.R.D. Verliefde, G.L. Amy, and J.C. van Dijk. Removal of different fractions of nom foulants during demineralized water backwashing. *Separation and Purification Technology*, 98:186–192, 2012.

[63] S. Li, S.G.J. Heijman, J.Q.J.C. Verberk, and J.C. van Dijk. Influence of ca and na ions in backwash water on ultrafiltration fouling control. *Desalination*, 250(2):861–864, 2010.

[64] C. Serra, L. Durand-Bourlier, M.J. Clifton, P. Moulin, J.C. Rouch, and P. Aptel. Use of air sparging to improve backwash efficiency in hollow-fiber modules. *Journal of Membrane Science*, 161(1-2):95–113, 1999.

[65] Y. Bessiere, C. Guigui, P.J. Remize, and C. Cabassud. Coupling air-assisted backwash and rinsing steps: a new way to improve ultrafiltration process operation for inside-out hollow fibre modules. *Desalination*, 240(1-3):71–77, 2009.

[66] T.M. Qaisrani and W.M. Samhaber. Impact of gas bubbling and backflushing on fouling control and membrane cleaning. *Desalination*, 266(1-3):154–161, 2011.

[67] C. Guigui, M. Mougenot, and C. Cabassud. Air sparging backwash in ultrafiltration hollow fibres for drinking water production. *IWA Publishing*, 3(5-6):415–422, 2003.

[68] E. Zondervan, B.H.L. Betlem, B. Blankert, and B. Roffel. Modeling and optimization of a sequence of chemical cleaning cycles in dead-end ultrafiltration. *Journal of Membrane Science*, 308(1-2):207–217, 2008.

[69] S. Strugholtz, K. Sundaramoorthy, S. Panglisch, A. Lerch, A. Bruegger, and R. Gimbel. Evaluation of the performance of different chemicals for cleaning capillary membranes. *Desalination*, 179(1-3):191–202, 2005.

[70] E. Zondervan, B.H.L. Betlem, and B. Roffel. Development of a dynamic model for cleaning ultra filtration membranes fouled by surface water. *Journal of Membrane Science*, 289(1-2):26–31, 2007.

[71] H. Jasak, H.G. Weller, and N. Nordin. In-cylinder CFD simulation using a C++ object-oriented toolkit. *SAE Technical Paper*, 2004.

[72] H.G. Weller, G. Tabor, H. Jasak, and C. Fureby. A tensorial approach to computational continuum mechanics using object-oriented techniques. *Computers in physics*, 12(6):620–631, 1998.

[73] A.S. Berman. Laminar flow in channels with porous walls. *Journal of Applied Physics*, 24(9):1232–1235, 1953.

[74] S.W. Yuan and A. Finkelstein. *Laminar Pipe Flow with Injection and Suction Through a Porous Wall*. Defense Technical Information Center, 1955.

[75] B. Bernales and P. Haldenwang. Laminar flow analysis in a pipe with locally pressure-dependent leakage through the wall. *European Journal of Mechanics - B/Fluids*, 43:100–109, 2014.

[76] J.P. Quaile and E.K. Levy. Laminar flow in a porous tube with suction. *Journal of Heat Transfer*, 97(1):66–71, 1975.

[77] R.M. Terrill and P.W. Thomas. On laminar flow through a uniformly porous pipe. *Applied Scientific Research*, 21(1):37–67, 1969.

[78] R.M. Terrill. Laminar flow in a porous tube. *Journal of Fluids Engineering, Transactions of the ASME*, 105(3):303–307, 1983.

[79] R.M. Terrill and G.M. Shrestha. Laminar flow through a channel with uniformly porous walls of different permeability. *Applied Scientific Research, Section A*, 15(1):440–468, 1966.

[80] L.S. Galowin, L.S. Fletcher, and M.J. Desantis. Investigation of laminar flow in a porous pipe with variable wall suction. *AIAA Journal*, 12(11):1585–1589, 1974.

[81] S.K. Karode. Laminar flow in channels with porous walls, revisited. *Journal of Membrane Science*, 191(1-2):237–241, 2001.

[82] A.S. Kim and Y.T. Lee. Laminar flow with injection through a long dead-end cylindrical porous tube: Application to a hollow fiber membrane. *AIChE Journal*, 57(8):1997–2006, 2011.

[83] L. Oxarango, P. Schmitz, and M. Quintard. Laminar flow in channels with wall suction or injection: a new model to study multi-channel filtration systems. *Chemical Engineering Science*, 59(5):1039–1051, 2004.

[84] N.S. Hanspal, A.N. Waghode, V. Nassehi, and R.J. Wakeman. Development of a predictive mathematical model for coupled stokes/darcy flows in cross-flow membrane filtration. *Chemical Engineering Journal*, 149(1-3):132–142, 2009.

[85] V. Nassehi. Modelling of combined navierstokes and darcy flows in crossflow membrane filtration. *Chemical Engineering Science*, 53(6):1253–1265, 1998.

[86] N. Tilton, D. Martinand, E. Serre, and R.M. Lueptow. Incorporating darcy's law for pure solvent flow through porous tubes: Asymptotic solution and numerical simulations. *AIChE Journal*, 58(7):2030–2044, 2012.

[87] H. Teng and T.S. Zhao. An extension of darcy's law to non-stokes flow in porous media. *Chemical Engineering Science*, 55(14):2727–2735, 2000.

[88] A. Pak, T. Mohammadi, S.M. Hosseinalipour, and V. Allahdini. CFD modeling of porous membranes. *Desalination*, 222(1-3):482–488, 2008.

[89] R. Ghidossi, J.V. Daurelle, D. Veyret, and P. Moulin. Simplified CFD approach of a hollow fiber ultrafiltration system. *Chemical Engineering Journal*, 123(3):117–125, 2006.

[90] P. Forchheimer. Wasserbewegung durch Boden. *Zeitschrift des Vereines Deutscher Ingenieuer*, 45:1782–1788, 1901.

[91] A. Dybbs and R.V. Edwards. A new look at porous media fluid mechanics-darcy to turbulent. In *Fundamentals of transport phenomena in porous media*, volume 82, pages 199–256. Springer, 1984.

[92] J.H. Ferziger and M. Peric. *Computational Methods for Fluid Dynamics*. Springer London, Limited, 2002. ISBN: 9783642560262.

[93] H. Enwald, E. Peirano, and A.E. Almstedt. Eulerian two-phase flow theory applied to fluidization. *International Journal of Multiphase Flow*, 22:21–66, 1996.

[94] C.T. Crowe, J.D. Schwarzkopf, M. Sommerfeld, and Y. Tsuji. *Multiphase Flows with Droplets and Particles*. Taylor & Francis, 1997. ISBN: 9780849394690.

[95] H. G. Weller. Derivation, modelling and solution of the conditionally averaged two-phase flow equations. *Technical Report TR/HGW/02, Nabla Ltd*, 2005.

[96] P.J. Oliveira. *Computer modelling of multidimensional multiphase flow and application to T-junctions*. PhD thesis, Imerial College, University of London, 1992.

[97] M. Ishii. *Thermo-fluid dynamic theory of two-phase flow*. Eyrolles, Paris, 1975. LCCN: 75314315.

[98] P.J. Oliveira and R.I. Issa. Numerical aspects of an algorithm for the eulerian simulation of two-phase flows. *International Journal for Numerical Methods in Fluids*, 43(10-11):1177–1198, 2003.

[99] J. Boussinesq. *Essai sur la théorie des eaux courantes*. Mémoires présentées par divers savants à l'Académie des Sciences. Imprimerie Nationale, 1877.

[100] L. Schiller and A.Z. Naumann. Ueber die grundlegenden Berechnungen bei der Schwerkraftaufbereitung. *Ver.Deut.Ing.*, 77:318–320, 1933.

[101] T.R. Auton. The lift force on a spherical body in a rotational flow. *Journal of Fluid Mechanics*, 183:199–218, 1987.

[102] L.F.L.R. Silva and P.L.C. Lage. Development and implementation of a polydispersed multiphase flow model in openfoam. *Computers and Chemical Engineering*, 35(12):2653–2666, 2011.

[103] OpenFOAM. The open source computational fluid dynamics CFD toolbox. *http://www.openfoam.com*.

[104] R.I. Issa. Solution of the implicitly discretised fluid flow equations by operator-splitting. *Journal of Computational Physics*, 62(1):40–65, 1986.

[105] D. Ramkrishna. *Population Balances: Theory and Applications to Particulate Systems in Engineering*. Elsevier Science, 2000. ISBN: 9780080539249.

[106] D. Ramkrishna and J.D. Borwanker. A puristic analysis of population balance-I. *Chemical Engineering Science*, 28(7):1423–1435, 1973.

[107] D. Ramkrishna and J.D. Borwanker. A puristic analysis of population balance-II. *Chemical Engineering Science*, 29(8):1711–1721, 1974.

[108] S. Kumar and D. Ramkrishna. On the solution of population balance equations by discretization-i. a fixed pivot technique. *Chemical Engineering Science*, 51(8):1311–1332, 1996.

[109] S. Kumar and D. Ramkrishna. On the solution of population balance equations by discretization-II. A moving pivot technique. *Chemical Engineering Science*, 51(8):1333–1342, 1996.

[110] R. McGraw. Description of aerosol dynamics by the quadrature method of moments. *Aerosol Science and Technology*, 27(2):255–265, 1997.

[111] D.L. Marchisio, R.D. Vigil, and R.O. Fox. Quadrature method of moments for aggregationbreakage processes. *Journal of Colloid and Interface Science*, 258(2):322–334, 2003.

[112] D.L. Marchisio and R.O. Fox. Solution of population balance equations using the direct quadrature method of moments. *Journal of Aerosol Science*, 36(1):43–73, 2005.

[113] L.F.L.R. Silva, R.B. Damian, and P.L.C. Lage. Implementation and analysis of numerical solution of the population balance equation in CFD packages. *Computers and Chemical Engineering*, 32(12):2933–2945, 2008.

[114] H. Rusche. *Computational Fluid Dynamics of Dispersed Two-phase Flows at High Phase Fractions*. PhD thesis, Imerial College, University of London, 2003.

[115] A. Keller, R. Gimbel, H. Mansour, and W. Kowalczyk. Studies on the removal of fouling layers in UF capillary membranes during backwash. *10th Aachen Conference Water and Membranes, Aachen, Germany*, 29-30.10.2013.

[116] G. Cano, P. Steinle, J.V. Daurelle, Y. Wyart, K. Glucina, D. Bourdiol, and P. Moulin. Determination of pressure and velocity fields in ultrafiltration membrane modules used in drinking water production. *Journal of Membrane Science*, 431:221–232, 2013.

[117] A. Dasilva, M. Heran, C. Sinfort, and A. Grasmick. Optimization of flow shear stress through a network of capillary fibers with the use of CFD. *International Journal of Chemical Reactor Engineering*, 2:1–11, 2004.

[118] G. Cano, P. Steinle, J.V. Daurelle, Y. Wyart, K. Glucina, D. Bourdiol, and P. Moulin. Pressure fields in an industrial uf module: effect of backwash. *Desalination and Water Treatment*, 51(25-27):4907–4913, 2013.

[119] Z. Wang, J. Ma, C.Y. Tang, K. Kimura, Q. Wang, and X. Han. Membrane cleaning in membrane bioreactors: A review. *Journal of Membrane Science*, 468:276–307, 2014.

[120] X. Meng, W. Tang, L. Wang, X. Wang, D. Huang, H. Chen, and N. Zhang. Mechanism analysis of membrane fouling behavior by humic acid using atomic force microscopy: Effect of solution ph and hydrophilicity of PVDF ultrafiltration membrane interface. *Journal of Membrane Science*, 487:180–188, 2015.

[121] B. Xu and R.M. Narbaitz. Improved membrane pretreatment of high hydrophobic natural organic matter (nom) waters by floatation. *Journal of Membrane Science*, 518:120–130, 2016.

[122] C. Regula, E. Carretier, Y. Wyart, G. Gesan-Guiziou, A. Vincent, D. Boudot, and P. Moulin. Chemical cleaning/disinfection and ageing of organic uf membranes: A review. *Water Research*, 56:325–365, 2014.